UNIVERSITY OF CALIFORNIA SAN DIEGO

Turbulent aftermaths: the long-lived ocean effects of atmospheric extremes

A dissertation submitted in partial satisfaction of the
requirements for the degree Doctor of Philosophy

in

Oceanography

by

Noel Gutiérrez Brizuela

Committee in charge:

Matthew H. Alford, Chair
Shang-Ping Xie, Co-Chair
Jennifer Burney
James N. Moum
Janet Sprintall
William R. Young

2023

The Dissertation of Noel Gutiérrez Brizuela is approved, and it is acceptable in quality and form for publication on microfilm and electronically.

University of California San Diego

2023

EPIGRAPH

And so it became clear, as they meditated, that man would appear with the sunrise. And so they called for the creation and growth of the trees and the vines, and the birth of life and the creation of man. It was decided this way in the darkness and in the night by the Heart of the Sky, whose name is Hurricane.

Popol Vuh

TABLE OF CONTENTS

LIST OF FIGURES

LIST OF TABLES

ACKNOWLEDGEMENTS

I am deeply thankful for the guidance of my advisors Matthew H. Alford and Shang-Ping Xie, and to everyone who helps make Scripps the wonderful place it is.

Chapter 1, in full, is a reprint of the material as it appears in G. Brizuela, Noel; Johnston, T. M. Shaun; Alford, Matthew H.; Asselin, Olivier; Rudnick, Daniel L.; Moum, James N.; Thompson, Elizabeth J.; Wang, Shuguang & Lee, Chia-Ying (2023). A vorticity-divergence view of internal wave generation by a fast-moving tropical cyclone: insights from Super Typhoon Mangkhut. *Journal of Geophysical Research: Oceans*. The dissertation author was the primary investigator and author of this paper.

Chapter 2, in full, is a reprint of the material as it appears in Gutiérrez Brizuela, N., Alford, M. H., Xie, S. P., Sprintall, J., Voet, G., Warner, S. J., Hughes, K., & Moum, J. N. (2023). Prolonged thermocline warming by near-inertial internal waves in the wakes of tropical cyclones. *Proceedings of the National Academy of Sciences*, 120(26), e2301664120. The dissertation author was the primary investigator and author of this paper.

Chapter 3, is currently being prepared for submission for publication of the material. G. Brizuela, Noel; Xie, Shang-Ping; Alford, Matthew H.; Xia, Yi; Voet, Gunnar; Moum, James N. have contributed to the investigation. The dissertation author was the primary investigator and author of this material.

VITA

2017	Bachelor of Science, Physics, Universidad de Guadalajara
2018	Master of Science, Oceanography, University of California San Diego
2023	Doctor of Philosophy, Oceanography, University of California San Diego

PUBLICATIONS

G. Brizuela, N., Johnston, T. M. S., Alford, N. H., Asselin, O., Rudnick, D. L., Moum, J. N., Thompson, E. J., Wang, S., & Lee, C. Y. (2023). A vorticity-divergence view of internal wave generation by a fast-moving tropical cyclone: insights from Super Typhoon Mangkhut. *Journal of Geophysical Research: Oceans*, e2022JC019400.

Gutiérrez Brizuela, N., Alford, M. H., Xie, S. P., Sprintall, J., Voet, G., Warner, S. J., Hughes, K. & Moum, J. N. (2023). Prolonged thermocline warming by near-inertial internal waves in the wakes of tropical cyclones. *Proceedings of the National Academy of Sciences*, 120(26), e2301664120.

Luongo, M. T., Brizuela, N., Eisenman, I., & Xie, S. P. (2023). Retaining short-term variability reduces biases in wind stress overriding simulations. *Under review*.

Nazarian, R., Brizuela, N., Matijevic, B. J., Vizzard, J. V., Agostino, C. P., & Lutsko, N. J. (2023). Projected changes in mean and extreme precipitation over northern Mexico. *Under review*.

Tariq, A., Banda, J. M., Skums, P., Dahal, S., Castillo-Garsow, C., Espinoza, B., G. Brizuela, N., Saenz, R. A., Kirpich, A., Luo, Ruiyan, Srivastava, A., Gutierrez, H., Garcia-Chan, N., Bento, A. I., Jimenez-Corona M., & Chowell, G. (2021). Transmission dynamics and forecasts of the COVID-19 pandemic in Mexico, March-December 2020. *PloS one*, 16(7), e0254826.

Brizuela, N. G., García-Chan, N., Gutierrez Pulido, H., & Chowell, G. (2021). Understanding the role of urban design in disease spreading. *Proceedings of the Royal Society A*, 477(2245), 20200524.

Johnston, T. S., Rudnick, D. L., Brizuela, N., & Moum, J. N. (2020). Advection by the North Equatorial Current of a cold wake due to multiple typhoons in the western Pacific: Measurements from a profiling float array. *Journal of Geophysical Research: Oceans*, 125(4), e2019JC015534.

Brizuela, N., Filonov, A., & Alford, M. H. (2019). Internal tsunami waves transport sediment released by underwater landslides. *Scientific Reports*, 9(1), 1-8.

ABSTRACT OF THE DISSERTATION

Turbulent aftermaths: the long-lived ocean effects of atmospheric extremes

by

Noel Gutiérrez Brizuela

Doctor of Philosophy in Oceanography

University of California San Diego, 2023

Matthew H. Alford, Chair
Shang-Ping Xie, Co-Chair

Cycles of heat transfer between the tropical ocean and atmosphere help drive some of the Planet's most important modes of climate variability. Subsurface turbulent heat fluxes (J_q) that redistribute ocean heat are known to mediate ocean-atmosphere dynamics at multiple timescales. However, a relative scarcity of observations has slowed down the inclusion of J_q in dynamical frameworks and theories of coupled tropical climate. This dissertation includes three chapters that use in-situ ocean measurements to explore the relations between atmospheric forcing, J_q, and other oceanic variables. Two case studies give special attention to the immediate and long-term ocean response to tropical cyclones (TCs), while a third chapter uses year-long

records of J_q to explain their relation to the Asian Monsoon, and interpret their impacts on the seasonality of ocean temperatures in the Western Pacific Warm Pool (WPWP). Overall, the results highlight the importance of atmospheric extremes in regulating J_q and ocean heat uptake by the WPWP and by cold water masses that lay beneath it. Most attention is given to TCs, the near-inertial internal waves (NIWs) they generate, and how NIWs allow TCs to transform ocean currents and thermodynamics for weeks after the storms have dissipated. Besides TCs, it is also emphasized that large scale dynamics can also give rise to atmospheric extremes in which background conditions cause dramatic seasonal shifts in J_q and ocean heat uptake.

Introduction

The tropical ocean exists between extremes. At one end of the scale, the ocean surface is flat and lethargic, winds are calm, and the skies are clear. At the other end is tempest, when raging winds drive relentless currents atop which waves shoot sea spray into the air, thereby seeding clouds that help perpetuate storms.

At any given time, a multitude of processes push the tropical ocean-atmosphere system closer to one or other extreme of this spectrum. El Nino, the Asian Monsoon, the Madden-Julian and Boreal Summer Intra-Seasonal Oscillations, and different forms of synoptic weather act simultaneously to create active-break cycles in rainfall and wind that span all timescales. By modulating winds and cloud formation, the push-and-pull that results from all these processes can also produce drastic swings in the direction and intensity of heat transfer in and out of the ocean. This way, the ocean takes up heat during sunny, calm days, and loses it during tempests.

This back and forth of heat transfer between the ocean and atmosphere, it turns out, is one of the primary forces that shape tropical weather and climate. Frankignoul and Hasselmann (1977) used a stochastic model to show that long-term variations in ocean temperature could result from the cumulative effects of random, high-frequency variations in atmospheric forcing. This result implies that, at any time, the ocean state reflects the history of past weather, and therefore leads to feedbacks from present to future atmospheric variability. The model used by Frankignoul and Hasselmann (1977) incorporates the effects of random weather in a sensible way, but it is phenomenological rather than mechanistic. In fact, understanding of some physical processes shaping the ocean response to atmospheric forcing, and representing them in physical models of climate remains a paramount challenge in physical oceanography.

Atmospheric forcing of the upper ocean can be described by the net heat flux across the air-sea interface (Q_{net}) and the tangential wind stress (τ) on the ocean surface. Standard meteorological measurements can often be used to parameterize Q_{net} and τ with sufficient accuracy to reproduce observed variations in sea surface temperature (SST) and horizontal ocean currents ($\mathbf{u}$) (Large and Pond, 1981; Fairall et al., 1996). However, small inaccuracies in τ and Q_{net} can become significant when their effects are integrated over long timescales. Likewise, standard parameterizations become unreliable under extreme weather conditions that call for more sophisticated measurements (Powell et al., 2003) that are costly and technically challenging. Limitations in the parameterization and measurement of Q_{net} and τ therefore complicate our mechanistic understanding of the connections between weather and climate: Because the principles exposed in Frankignoul and Hasselmann (1977) rely on the cumulative effects of weather extremes, errors in standard parameterizations can easily propagate and lead physical models to misrepresent feedbacks in the ocean-atmosphere system.

Early implementation of numerical models that simulated the upper ocean response to changes in atmospheric forcing (Kraus and Turner, 1967; Price et al., 1986; Price, 1981) quickly led oceanographers to recognize that turbulence was important to redistribute heat down from the ocean surface and reproduce realistic temperature profiles. Eventually, observations of the subsurface turbulent heat flux (J_{q}) became possible due to advances in sensor technology and turbulence parameterizations relating energy dissipation to the vertical redistribution of buoyancy (Osborn, 1980; Gargett and Moum, 1995). Measuring J_{q} remains a costly, challenging, and somewhat imprecise task to this day. If anything, methods used to estimate J_{q} may in fact carry greater uncertainties than parameterizations of Q_{net} and τ generally do. Still, when added to a suite of complementary air-sea observations, estimates of J_{q} have helped refine understanding of the mechanisms by which atmospheric forcing impacts the upper ocean at timescales from hours to years (D'Asaro, 2003; Hughes et al., 2020b; Moum et al., 2013; Warner and Moum, 2019), and subsequent feedbacks to the atmosphere (Moum et al., 2016).

The magnitudes of all τ, Q_{net}, and J_{q} simultaneously peak directly beneath tropical

cyclones (TCs). TC winds as fast as $80\,\mathrm{m\ s^{-1}}$ induce $\|\tau\| \approx 10\,\mathrm{Pa}$, which is roughly 50-100 times greater than climatological values of $\|\tau\|$ in most areas of the ocean. Such extreme forcing leads to contributions $\sim -1000\ \mathrm{W\ m^{-2}}$ to Q_{net} from latent heat fluxes (Liu et al., 2011). Heat transfer from the near-surface to the thermocline, however, can reach $J_{\mathrm{q}} \sim 5000\,\mathrm{W\ m^{-2}}$ (D'Asaro, 2003; Brizuela et al., 2023a) and ultimately dominate changes in SST beneath high-intensity TCs (Vincent et al., 2012a).

TC-driven turbulence cools SST by driving vertical shear in near-surface currents and thereby promoting the upward entrainment of cold thermocline water (Price, 1981). This process of SST cooling is best known for its short-term effects on TC intensification, as cold SST inhibits deep convection and can sometimes shut it down completely (Emanuel, 1999). Less recognized, but of noteworthy significance to climate, is that turbulent heat transfer under TCs leaves behind anomalously warm thermocline that lie below cold SST wakes:

Emanuel (2001) proposed that excess heat put into the thermocline by TC-driven mixing could be an important source of variability in large scale ocean heat transports. Subsequent satellite estimates (Sriver and Huber, 2007; Mei et al., 2013) confirmed that thermocline warming by TC-driven mixing had the potential to modulate regional ocean heat budgets. Numerical experiments suggested that thermocline warming by TCs helps sustain SST in the subtropical and eastern Equatorial Pacific (Korty et al., 2008; Fedorov et al., 2010). Despite the potential implications of this 'ocean heat pump hypothesis' (as the proposal in Emanuel (2001) became known), in-situ observational attempts to detail the long-term fate of heat anomalies induced by TCs have been scarce and unable to disentangle the simultaneous effects of J_{q} and three-dimensional advection (Park et al., 2011; Mrvaljevic et al., 2013; Johnston et al., 2020).

Being perhaps the greatest form of extreme forcing shaping the tropical oceans, TCs and the ocean heat pump hypothesis offer a valuable opportunity to inspect the mechanisms that link short-term atmospheric variability and long-term ocean change (Frankignoul and Hasselmann, 1977). SST cooling induced by TCs induces variations in air-sea coupling over synoptic-to-intra-seasonal timescales (Emanuel, 1999; Fu and Wang, 2004; Moum et al., 2016) and thereby shapes

the high-frequency forcing that Frankignoul and Hasselmann (1977) described as random noise. However, the focus of this thesis is on the gradual drift of ocean temperatures that results from the cumulative effects of this frequency forcing and the mechanisms that govern it. Because deeper ocean layers affect the atmosphere at greater timescales than those near the surface, we are thus interested in resolving how heat makes its way from the ocean surface down into the thermocline, and J_q is our main variable of interest.

To advance understanding of the long-term ocean effects of high frequency atmospheric forcing, the three chapters of this thesis present in-situ estimates of J_q and assesses their significance to the upper ocean temperature balance. The research presented here sums insight to a growing body of literature detailing how J_q modulates the vertical distribution of ocean heat under different atmospheric conditions (Moum et al., 2013; Warner et al., 2016; Moum et al., 2016; Pujiana et al., 2018; Hummels et al., 2020). In particular, all three chapters are focused on the Western Pacific Warm Pool, where all major modes of tropical climate variability converge. To manage the complexity of air-sea interactions in this region, we take a process-based approach and dedicate each chapter to mechanisms acting at different timescales as follows:

The immediate ocean response to a fast-moving TC

Chapter 1 gives a detailed overview of the immediate ocean response to a fast-moving TC (Super Typhoon Mangkhut, September of 2018). Using data from six autonomous profiling floats, three interrelated aspects of the ocean response are highlighted: (1) the generation of near-inertial internal waves (NIWs), (2) the downward transfer of near-surface heat by J_q during TC passage, and (3) the turbulent diffusion of rain layers induced by the TC itself. (1) is a well-studied problem and the underlying mechanisms have been understood for decades (Geisler, 1970; Price, 1983; Gill, 1984). However, the chapter brings novelty to it by introducing a theoretical framework that allows us to express inertial pumping -the mechanism by which TCs generate NIWs- through ordinary differential equations rather than partial ones. The validity of this theoretical framework is validated using both float measurements and a 3D coupled model

of the TC.

Even though numerical models can represent (2) with relative accuracy, in-situ estimates of the turbulent diffusivity (κ) and J_q directly beneath TCs are very scarce (D'Asaro, 2003). Using vertical profiles of temperature and salinity from floats beneath the TC, the analysis identifies density overturns and infers κ and J_q with values as high as $\sim 0.1\,\mathrm{m\ s^{-1}}$ and $\sim 4000\,\mathrm{W\ m^{-2}}$ respectively. These values are consistent with observed rates of SST cooling, thus suggesting that methods used in this analysis can be implemented to further constrain the role of turbulence in air-sea interactions under TCs.

Lastly, (3) constitutes one of the greatest challenges curbing the performance of numerical models in representing air-sea interactions under TCs. Near-surface layers of freshwater are known to suppress SST cooling or even lead to SST warming when fresh layers lay over subsurface temperature maxima (Balaguru et al., 2012; Rudzin et al., 2019). Analyses presented in Chapter 1 contribute to this problem by detailing the gradual erosion of rain layers detected in float data, and by estimating the energetic cost of mixing rainfall with the underlying seawater.

Long-term effects of TC forcing on the tropical thermocline

Chapter 2 begins with an overview of the ocean heat pump hypothesis and of the main argument against it. Years after Emanuel (2001) proposed the hypothesis, a multiple studies used satellite data and models to constrain the global contribution of TCs to the ocean heat budget (Sriver and Huber, 2007) and likely impacts to climate (Korty et al., 2008; Sriver et al., 2010; Scoccimarro et al., 2011). However, Jansen et al. (2010) pointed out that excess heat in the ocean thermocline would only stay locked in beneath the surface if it stayed below the wintertime mixed layer (ML) base. Accounting for this in a way that was consistent with the assumptions made in previous studies that addressed the hypothesis, Jansen et al. (2010) estimated that the entire TC contribution to ocean heat could be lost during the winter, and thus not contribute to shape the background ocean stratification or climate. While this weakened the acceptance of the hypothesis among climate scientists, subsequent studies (Mei et al., 2013) continued to find

indirect evidence that TCs do make long-lasting, net contributions to the ocean heat budget. Yet, the mechanisms that could explain prolonged retention of TC-induced warming in the tropical thermocline remained unclear.

Analyses laid out in Chapter 2 use microstructure estimates of J_q before and after the passage of three major TCs in the Philippine Sea to resolve how the downward transfer of thermocline heat changes after TC passage. It is demonstrated that NIWs generated by TCs greatly deepen the reach of TC-induced ocean warming to depths greater than that of the winter ML, thus ensuring that excess heat remains locked in for years and that their impacts of weather be remote. NIWs are able to do this because their downward propagation brings momentum into the ocean current and drive sheared currents that enhance turbulence and ultimately mix thermal gradients. The discussion highlights how NIWs and thermocline mixing had not been considered, at all, in previous studies addressing this problem. Thus, the paradigm had been to assume that TCs only induced mixing during their passage, and only at the base of the ML. By showing that NIWs can drive up the permanent thermocline J_q to values of heat transfer equivalent to direct atmospheric exposure, the results in this section make the case for the inclusion of NIWs in future studies of TC-climate interaction.

Stepping back and putting it all in perspective

Even though the heat stored in the WPWP drives some of the foremost modes of climate variability, exactly how the WPWP takes up and stores that heat, and how it transfers it to other components of the climate system, is only known loosely. Time- and area-averaged values of Q_{net} over the WPWP range by as much as 40 W m^{-2} in different atmospheric reanalyses (Song and Yu, 2013). While the Tropical Pacific is increasingly recognized as the primary source of ocean heat (Forget and Ferreira, 2019), such large uncertainties in Q_{net} have serious implications for the accuracy of coupled climate models. In particular, because without knowing how much heat enters the WPWP, it is impossible to obtain consistent estimates of heat transfer out of the WPWP and into colder, deeper layers of the ocean (Song and Yu, 2013). This is particularly pressing, as

climate simulations have shown that variations in the WPWP κ can lead to anomalous SST in the Eastern Pacific and therefore disturb (or help sustain) the East-West Equatorial Pacific SST contrast (Fedorov et al., 2010; Sriver et al., 2010).

Chapter 3 of this dissertation combines insight from the previous two chapters to synthesize results from two year-long records of J_q in the northern WPWP. The focus of the analysis is on the seasonality of J_q and other turbulent variables, and to explain how that seasonality arises from atmospheric forcing imposed by the Asian Monsoon System. Our results show that heat accumulates near the ocean surface during the Inter-Monsoon Period (March to June), when SST increases and the WPWP expands northward. Near-surface heat is later transferred to the ocean thermocline during the Summer and Winter Monsoons, when upper ocean J_q increases. One key difference between these two Monsoon periods is that increased summertime mixing results from the influence of weather, while wintertime mixing is primarily forced by background winds.

Chapter 1

A vorticity-divergence view of near-inertial internal waves by a fast-moving tropical cyclone: insights from Super Typhoon Mangkhut

Tropical cyclones (TCs) power upper ocean currents that help redistribute heat and momentum throughout the water column (Geisler, 1970; Shay et al., 1989) and lead to turbulence that mixes thermal gradients, thereby exposing subsurface waters to atmospheric influence (Price, 1981; Balaguru et al., 2012). These processes are known to impact short-term weather forecasts (Schade and Emanuel, 1999) but may also cause variations in long-term climate (Emanuel, 2001; Fedorov et al., 2010). Furthermore, phytoplankton blooms behind TCs are thought to contribute as much as 20% of primary productivity in some marginal seas (Menkes et al., 2016). Therefore, untangling the multiple processes that unfold beneath and behind TCs is important to refine their representation in numerical weather prediction models, but also to understand the complex role of TCs in the Earth system.

Near-surface currents that rotate near the inertial frequency (f) dominate upper ocean dynamics behind fast-moving TCs (Geisler, 1970; Price, 1983; Shay et al., 1998). Transient winds amplify inertial currents on the right (left) side of Northern (Southern) hemisphere TCs but suppress them on the opposite side, thus causing an asymmetric distributing energy across TC tracks (Chang and Anthes, 1978; Price, 1981). Horizontal convergence and divergence

associated with these currents lead to inertial pumping of the mixed layer (ML) base, which allows near-inertial internal waves (NIWs) to propagate down across the ML base and transfer momentum into the thermocline (Price, 1983; Gill, 1984). Although inertial pumping and its interactions with background ocean motions are beginning to be better understood (Kunze and Sanford, 1984; Balmforth et al., 1998; Whitt and Thomas, 2015; Thomas et al., 2020; Sanford et al., 2021), general approaches that help understand links between storm morphology and resulting patterns of NIW generation are still lacking.

Turbulence and advection associated with wind-driven currents help redistribute heat across subsurface reservoirs. Notably, shear-driven turbulence at the ML base cools the sea surface temperature (SST) during and shortly after TC passage, reducing subsequent heat fluxes to the atmosphere and helping modulate the intensity of TCs (Emanuel, 1999; Glenn et al., 2016). Without in-situ measurements of the turbulent diffusivity (κ), only numerical models can isolate changes in stratification caused by mixing from the effects of upwelling and air-sea fluxes (Vincent et al., 2012a; Zhang et al., 2018), but such models rely on imperfect parameterizations to represent mixing. Furthermore, better constraints on the magnitude and spatiotemporal extent of enhanced κ induced by TCs are crucial to understand and quantify the TC contribution to global ocean heat uptake and transport (Brizuela et al., 2023a).

In this article, we use data from six profiling floats (Johnston and Rudnick, 2021; Johnston et al., 2020) to reconstruct the 3D fields of temperature (T), salinity (S), and currents (u, v, w) beneath Super Typhoon Mangkhut (Fig. 1.1). Data are compared with output from a coupled 3D ocean-atmosphere model of Mangkhut (Wang, 2020; Johnston et al., 2021). Under the assumption that the upper ocean response to TC forcing approaches a steady state when viewed in storm-following coordinates (Geisler, 1970), we diagnose the roles of upwelling, advection, and mixing in the redistribution of subsurface heat and rainfall inputs. Float velocity data are used to validate linear theory results showing that upwelling and NIW generation under TCs result from the coupling of ML vorticity ($\zeta \equiv \frac{\partial v}{\partial x} - \frac{\partial u}{\partial y}$) and divergence ($\Gamma \equiv \frac{\partial u}{\partial x} + \frac{\partial v}{\partial y}$) by Earth's

rotation. As explained below, this coupling is equivalent to the horizontal rotation of near-inertial currents under TCs as examined by Geisler (1970); Price (1983), and others. As argued below, changing variables to vorticity and divergence provides additional insight on the mechanisms of upwelling and NIW generation under TCs.

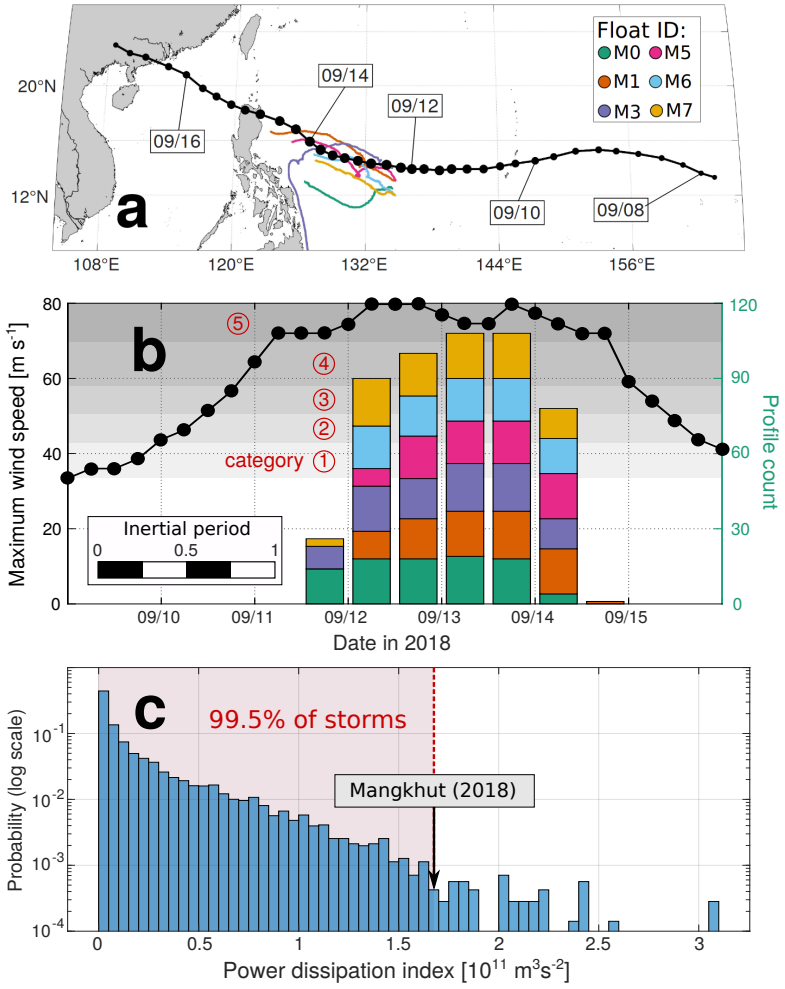

Figure 1.1. TC overview. (**a**) Best track data (Joint Typhoon Warning Center, 2022) shown in black and float trajectories are in colors. (**b**) Maximum 1-minute sustained wind speed $|U_{10}|$ (dotted line, left axis) and histogram showing the time distribution of float measurements. Gray shading in (**b**) shows the wind speed thresholds for Saffir-Simpson TC categories 1 ($\|U_{10}\| \leq 30\,\mathrm{m\,s^{-1}}$) to 5 ($|U_{10}| > 70\,\mathrm{m\,s^{-1}}$). (**c**) Probability distribution of power dissipation index estimated for >7000 storms puts Mangkhut among the 0.5% most powerful tropical storms in record.

Section 2 describes our data and processing methods including details about the 3D

model used for validation. Section 3 lays out the linear theory of upwelling and NIW generation under TCs and reformulates standard ML dynamics in terms of ζ and Γ to demonstrate their inertial coupling. Section 4 presents observational and modelled maps of (u, v) to verify relations between wind forcing, vorticity, divergence and NIW generation. Indirect evidence of turbulent mixing under Mangkhut is presented using float measurements of T and S in Section 5. A discussion of our methods and results is presented in Section 6, while conclusions are given in Section 7.

1.1 Data and Methods

1.1.1 Data collection

Super Typhoon Mangkhut originated on September 7, 2018 as a tropical depression in the central Pacific Ocean and later intensified as it moved westwards into the Philippine Sea. Between September 11 and 15, when our measurements were made, Mangkhut always sustained maximum 1-minute wind speeds between 70 and 80 m s^{-1} (Fig. 1.1b), equivalent to a category 5 hurricane. Between September 11 and 14, Mangkhut's mean translation speed was approximately $U_{storm} \approx 6.2$ m s^{-1} or twice the local group speed ($\mathbf{c}_g$) of the first baroclinic mode, making it a fast-moving TC whose ocean response was dominated by NIWs (Geisler, 1970; Nilsson, 1995). Throughout the TC's period of maximum intensity, SOLO-II floats (Davis et al., 2001) sampled the ocean response under the TC (Fig. 1.1b). The combination of Mangkhut's long lifespan and elevated intensity put it among the 0.5% most powerful tropical storms on record (Fig. 1.1c, Emanuel 2005). As it travelled through the Philippine and South China Seas, Mangkhut caused significant damage and loss of life in the Philippines, Guam, Taiwan, Hong Kong, and China (Wamsley, 2018).

Upon deployment, the floats modified their buoyancy to dive up to 200 m depth and back to the surface at intervals < 50 minutes. While doing so, they obtained upward profiles of T and S, and drifted westward with the North-Equatorial Current at ~ 0.18 m s^{-1} (Fig. 1.2a,

Johnston et al. 2020). Because floats record their coordinates at the beginning and end of every dive cycle, their Global Positioning System data yields two estimates of horizontal velocity (Fig. 1.2b). $\mathbf{u}_{mean}$ is the depth-mean current over the profiling range and is calculated using the difference between the start and end locations of individual dives. Surface estimates $\mathbf{u}_{surf}$, which are subject to wave motion and windage, are calculated using the drift between consecutive dives, when floats remain at the surface for $\sim$ 5 minutes while they transfer data via Iridium satellite.

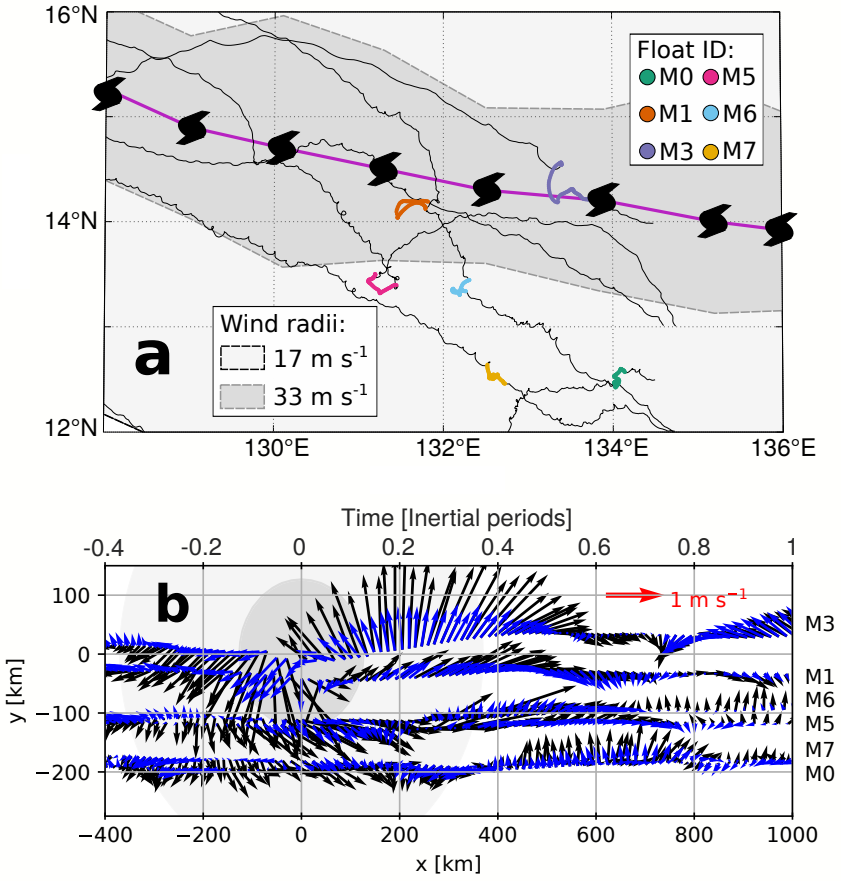

Figure 1.2. (**a**) 6-hourly best track data for Mangkhut (black vortices). Black lines mark float trajectories, while the locations of vertical profiles used in this study are highlighted in colors. (**b**) Plane view of $\mathbf{u}_{surf}$ (black) and $\mathbf{u}_{mean}$ (blue), with x and y components scaled equally to show the true direction of currents in storm-following coordinates (x, y).

Output from a coupled ocean-atmosphere model of Mangkhut is compared to dynamical insights derived from float velocity data. The coupled system uses the Weather Research and

Forecast (WRF) model V3.8.1 (Skamarock et al., 2008) as its atmospheric component, while the ocean is represented by the Hybrid Coordinate Ocean Model V2.2 (HYCOM; Wallcraft et al. 2009). Horizontal grid spacing in HYCOM was $1/12^{\circ}$ for 41 vertical layers (10 in the upper 50 m) and output was saved at 3 hour intervals. Chen and Curcic (2016) give an assessment of this coupled model's performance under North Atlantic TCs. Further details about the model configuration used for Mangkhut were given by Johnston et al. (2021).

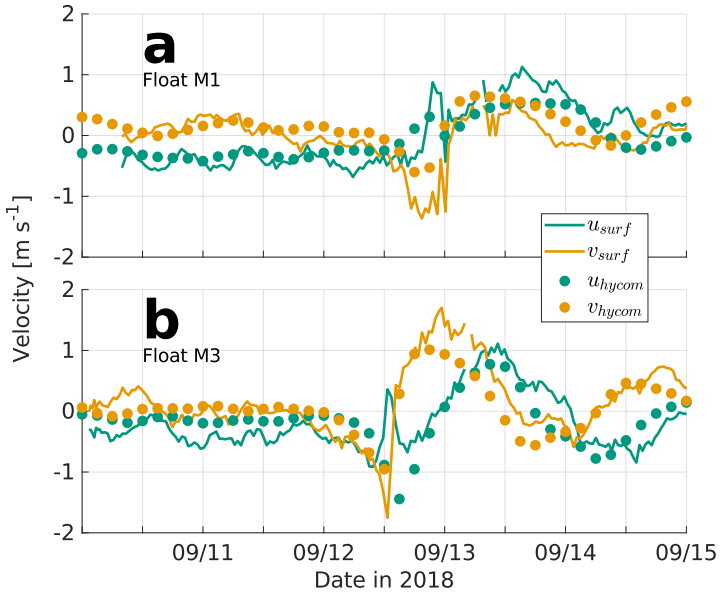

Figure 1.3. Model-observation comparison of upper ocean velocities. ML velocities $\mathbf{u}_{hycom}$ (circles) at fixed locations in the coupled 3D model are compared against measurements $\mathbf{u}_{surf}$ (solid lines) from floats (**a**) M1 and (**b**) M3.

Comparisons of model output against measured $\mathbf{u}_{surf}$ (Fig. 1.3) are indicative of both the accuracy of the simulation and that of float velocity estimates. Although qualitative agreement between both datasets is good, neither float nor model data in Fig. 1.3 should be regarded as ground truth for ocean conditions at a time and place. While $\mathbf{u}_{surf}$ may be biased by windage or wave motion, the model's atmospheric component lets Mangkhut evolve dynamically, such that the modelled track and intensity differ slightly from observations (Johnston et al., 2021). To account for this, model velocities $\mathbf{u}_{hycom}$ in Fig. 1.3 were taken from the average location of each float within 24 h of TC passage. As described next, objective mapping of float data onto

storm-following coordinates provides a more meaningful representation of ML dynamics under Mangkhut than pointwise comparisons in Fig. 1.3.

1.1.2 3D reconstruction of the ocean response

Best track data for Mangkhut (Joint Typhoon Warning Center, 2022) was linearly interpolated to the times of float data, which were then reorganized in storm-following coordinates (x,y) (Fig. 1.2b). Positive values of x denote regions behind the storm eye, while $y > 0$ indicates locations right of the TC track. Likewise, $\mathbf{u}_{surf}$ and $\mathbf{u}_{mean}$ were rotated such that u and v represent along-track and cross-track velocities respectively. Plots in (x,y) use the equivalent time $t = x/U_{storm}$ to preserve information about temporal variability that has been mapped onto x. We use $U_{storm} = 6.2$ m s^{-1} to characterize Mangkhut between September 11 and 14, when its translation speed remained nearly constant (RMSE 0.5 m s^{-1}) and $\sim$85% of our measurements were made (Fig. 1.1b). Time scaling $t\frac{f}{2\pi}$ used in visualizations uses the inertial period $\frac{2\pi}{f}$ at 15.54°N ($\sim$ 45 hr) such that one inertial period in t corresponds to $U_{storm}\frac{2\pi}{f}$ =1000 km in x (Fig. 1.2b).

Despite the fact that each float effectively sampled different parts of the storm at different times (Fig. 1.2a), both $\mathbf{u}_{surf}$ and $\mathbf{u}_{mean}$ line up with $v < 0$ ($v > 0$) for $x < 0$ ($x > 0$) and later rotate in the clockwise sense in the TC wake. Such similarities in measurements made by different floats at different times in Fig. 1.2b suggest that the ocean response was steady within the TC-following (x,y) coordinates (Geisler, 1970). To best exploit the spatiotemporal information embedded in float data, we used objective mapping (Davis, 1985; Le Traon et al., 1998) with a Gaussian decorrelation scale of 150 km to horizontally interpolate measurements $\mathbf{u}_{surf}$, $\mathbf{u}_{mean}$, T, and S. The signal-to-noise ratio for objective mapping was set to 10, and areas where the estimated mean square error of interpolated fields is greater than 7.5% of signal variance have been masked out in plots.

To reconstruct 3D patterns in T and S, we stacked 2D maps at 5 m intervals, thus

producing $T^*(x,y,z)$ and $S^*(x,y,z)$. Here, the star * denotes objectively mapped variables. Although vertical variations in u,v were not measured directly, we use differences between $\mathbf{u}^*_{surf}$ and $\mathbf{u}^*_{mean}$ to separate the ML flow from the less energetic ocean below (Johnston et al., 2021). More precisely, we assume that depth-dependence at each location (x,y) is given by

$$\mathbf{u}^*(x,y,z) = \begin{cases} \mathbf{u}^*_{surf} & z \geq -h \\ \mathbf{u}^*_{surf} + \left\langle \frac{\partial \mathbf{u}}{\partial z} \right\rangle (z-h) & -h > z > -h-l \\ \mathbf{u}^*_{surf} + \left\langle \frac{\partial \mathbf{u}}{\partial z} \right\rangle l & -h-l \geq z \geq -H. \end{cases} \tag{1.1}$$

The piecewise function (1.1) includes two layers of depth-constant velocity and a sheared transition layer between them. Flow in the uppermost layer, which spans the depth of the ML $-h < z \leq 0$, is given by $\mathbf{u}^*_{surf}$. Here, h is defined as the depth at which T^* is 0.2 °C colder than it is at 20 m depth; this helps avoid transient effects of diurnal warm layers and rain layers, whose timescale of dynamical significance under intense wind forcing is much shorter than that of near-inertial motions (Thompson et al., 2019; Hughes et al., 2020a). Below $z = -h$, we assume a transition layer of thickness l and constant shear

$$\left\langle \frac{\partial \mathbf{u}}{\partial z} \right\rangle = 2H \frac{\mathbf{u}^*_{surf} - \mathbf{u}^*_{mean}}{[l^2 + 2l(H-l-h)]}. \tag{1.2}$$

This transition layer is set by the vertical penetration of wind-driven turbulent momentum, which determines the depth at which $\mathbf{u}$ no longer behaves like a slab (Turner and Kraus, 1967; Pollard et al., 1973). In reality, the transition layer thickness can vary considerably and is seen as a stratification and shear maximum below the ML base (Johnston and Rudnick, 2009). However, vigorous mixing and internal wave strain behind Mangkhut makes it such that a transition layer cannot be reliably identified in profiles of T and S at many locations. Therefore, we set a constant thickness $l = 30$ m, which is based on the mean value found by Johnston and Rudnick (2009) when defining the transition layer based on the magnitude of the vertical shear squared. Lastly, the third and deepest layer extends down to $H = 180$ m and has velocities $\mathbf{u}^*_{surf} + \left\langle \frac{\partial \mathbf{u}}{\partial z} \right\rangle l$. Here,

H is set by the depth of individual float dives, which ranged between 180 and 200 m. This way, equations (1.1) and (1.2) force the depth-mean of $\mathbf{u}^*$ between $z = 0$ and $z = -H$ to be equal to $\mathbf{u}^*_{mean}$.

Concentrating $\left\langle \frac{\partial \mathbf{u}}{\partial z} \right\rangle$ within a transition layer captures some of the main features of wind-forced currents. Thus, equations (1.1) and (1.2) yield an idealized 3D velocity field constrained by float velocity estimates and previous knowledge of the baroclinic response to TC forcing. However, it should be noted that high baroclinic modes that cannot be represented by equation (1.1).

To finalize the reconstruction of 3D flows beneath Mangkhut from float measurements, we impose a condition of adiabatic continuity to obtain $\frac{\partial w^*}{\partial z} = -\frac{\partial u^*}{\partial x} - \frac{\partial v^*}{\partial y}$. Furthermore, we assume a rigid lid so that $w^*(z = 0)$ vanishes and the vertical velocity is

$$w^*(x,y,z) = \int_0^z \left(\frac{\partial u^*}{\partial x} + \frac{\partial v^*}{\partial y} \right) dz'. \tag{1.3}$$

Before showing the interpolated fields T^*, S^*, u^*, v^*, w^*, we must emphasize that (1) they only resolve gradients at scales $\sim$ 150 km and greater, given the decorrelation lengthscale $L =$ 150 km and the maximum float separation of roughly 100 km. Moreover, (2) Caution is warranted when interpreting results near the edge of the objective maps, and (3) while equation (1.1) loosely approximates the vertical structure of a mode 1 baroclinic mode, the full ocean response to TC winds includes higher vertical modes that drive shear throughout the thermocline (Shay et al., 1989, 1998). Therefore, w^* can reproduce vertical displacements at the ML base but may fail to capture realistic variations deeper in the water column.

1.1.3 Thorpe scale estimates of turbulence

Vertical profiles of T and S taken at 1 Hz (vertical resolution $\sim$ 0.2 m) were used to compute in situ density (ρ). These allowed us to derive Thorpe scale estimates (Thorpe, 1977) of the turbulent dissipation rate (ε) and diffusivity (κ) within unstable overturns where $\frac{\partial \rho}{\partial z} > 0$.

This method relies on reordering vertical profiles of ρ to obtain ρ_{ordered} such that $\frac{\partial \rho_{\text{ordered}}}{\partial z} \leq 0$; then, an overturn is said to span every contiguous vertical range for which $\rho \neq \rho_{\text{ordered}}$. For each overturn, we compute the set of vertical displacements d' necessary to turn ρ into ρ_{ordered} and viceversa, thus defining the Thorpe scale as $L_{Ti} = \sqrt{\langle d'^2 \rangle_i}$, where the brackets indicate averaging within an overturn i. Given this, ε was calculated as

$$\varepsilon_i = 0.64 L_{Ti}^2 \langle N \rangle_i^3. \tag{1.4}$$

Here, $\langle N \rangle_i$ is the mean buoyancy frequency calculated from the sorted profile of ρ. To filter out spurious overturns caused by random noise and spikes in our data, estimates of ε were discarded for overturns in which any of the following were true:

1. The height of overturning cells (D_z) was less than 5 m (this choice was made for consistency, as 5 m is the vertical resolution of T^* and S^*).
2. $D_z < 2\Delta\rho_{\text{noise}} \left\langle -\frac{\partial \rho}{\partial z} \right\rangle_i^{-1}$, where $\Delta\rho_{\text{noise}} = 5 \times 10^{-4}$ kg m^{-3} is the standard error in ρ data (Galbraith and Kelley, 1996).
3. The change in density across an overturn is less than $2\Delta\rho_{\text{noise}}$
4. Positive displacements ($d' > 0$) make up less than 20% or more than 80% of all d' values within the overturning cell (Gargett and Garner, 2008).

Next, valid estimates of ε were used with the relation in Osborn (1980) to compute $\kappa_i = 0.2 \frac{\varepsilon_i}{\tilde{N}^2}$. Here, $\tilde{N}$ is the background buoyancy frequency from sorted profiles of ρ. This allows us to estimate the downward turbulent heat flux

$$J_{qi} = \rho_0 C_p \kappa_i \langle \frac{\partial T}{\partial z} \rangle_i. \tag{1.5}$$

Here, the constants are $\rho_0 = 1024$ kg m^{-3} and $C_p = 4000$ J kg^{-1} $^\circ$C^{-1}. Comparisons between Thorpe-inferred quantities and microstructure measurements suggest that equation

(1.4) can yield valid estimates in the thermocline beneath a TC, where temperature gradients are sharp and convective instability is not the main driver of turbulence (Dillon, 1982; Ferron et al., 1998; Dunckley et al., 2012; Mater et al., 2015; Hamann et al., 2021). More details on the implementation, assumptions, and limitations of the Thorpe scale method can be found in Johnson and Garrett (2004); Thompson et al. (2007); Scotti (2015) and references therein.

1.2 Mixed layer theory

In this section, we review the mechanisms of NIW generation by TCs and formulate the relevant linear ML dynamics. Instead of understanding ML motions using depth-averaged ML currents $\bar{\mathbf{u}} = (\bar{u}, \bar{v})$, we use their vorticity ($\zeta = \mathbf{k} \cdot \nabla \times \bar{\mathbf{u}}$) and divergence ($\Gamma = \nabla \cdot \bar{\mathbf{u}}$). This change of variables leads to a coupling between ζ and Γ that gives rise to inertial pumping and helps conceptualize NIW generation by TCs as a 1D rather than 3D process. By stating inertial pumping as a set of ordinary differential equations rather than partial differential equations, as done by Gill (1984), the spatiotemporal patterns of NIW generation are more easily related to the morphology of atmospheric forcing $\tau = (\tau_x, \tau_y)$. In order to simplify the notation, the projection onto the vertical unit vector $\mathbf{k}$ is henceforth implied when computing the curl of 2D vector fields.

The response of $\bar{\mathbf{u}}$ to τ in a ML of thickness h can be described using the linear slab model

$$\frac{\partial \bar{u}}{\partial t} = f\bar{v} + \frac{\tau_x}{\rho_0 h} - r\bar{u} \tag{1.6}$$

$$\frac{\partial \bar{v}}{\partial t} = -f\bar{u} + \frac{\tau_y}{\rho_0 h} - r\bar{v} \tag{1.7}$$

$$\frac{\partial h}{\partial t} + h\nabla \cdot \bar{\mathbf{u}} = W_e. \tag{1.8}$$

Pollard and Millard (1970) first used these equations to explain in situ measurements of

$\bar{\mathbf{u}}$, while recent studies have shown their skill in reproducing the ocean response to TCs (Guan et al., 2014). Solutions to Eqs. (1.6) and (1.7) may be written as the sum of two terms (D'Asaro, 1985), one that varies slowly and approximates an Ekman balance, and another representing near-inertial oscillations whose amplitude decays exponentially due to the damping coefficient r. In order to resolve vertical velocities at the ML base ($\frac{\partial h}{\partial t}$), we couple (1.6) and (1.7) to the continuity equation (1.8). Here, $W_e \geq 0$ is an entrainment rate used to represent ML deepening caused by turbulent mixing (Price, 1981).

Because our focus here is on NIW generation, equations (1.6)-(1.8) exclude pressure gradient and advection terms that make negligible or secondary contributions to $\frac{\partial h}{\partial t}$ under TCs. Even though horizontal surface pressure gradients drive flows in TC wakes (Shay and Chang, 1997), they scale to make a negligible contribution to $\frac{\partial h}{\partial t}$ (Geisler, 1970; Gill, 1984; D'Asaro, 1989). Similarly, nonlinear solutions of $\frac{\partial h}{\partial t}$ by Price (1981) are in agreement with linear analytical results obtained for fast-moving storms Geisler (1970), suggesting that the advective terms can be dropped from the equations of motion (Fig. 10 in Price 1981). While 3D effects associated with the pressure and advection terms may play a significant role under slow-moving TCs (Yablonsky and Ginis, 2009), simplified dynamics in Equations (1.6)-(1.8) can reproduce the ocean response to fast-moving TCs, defined as those whose translation speed $\mathbf{U}_{storm}$ is greater than the local group speed ($\mathbf{c_g}$) of the first baroclinic mode ($\mathbf{U}_{storm}/\mathbf{c_g} > 1$) (Geisler, 1970; Nilsson, 1995).

When the ML base oscillates at frequencies slightly greater than f, periodic pumping of the ML base and pressure gradients that result under it allow downward momentum transfer in the form of NIWs (Price, 1983; Gill, 1984). Therefore, the full baroclinic ocean response to TCs must be represented by coupling contiguous layers of increasing density through interfacial displacements (Geisler, 1970; Price, 1983). Given that their focus is on the ML, equations (1.6) and (1.7) do not represent these thermocline processes explicitly. Rather, they use the empirical damping rate r to parameterize the gradual decay of ML momentum that results from internal wave propagation, nonlinearities, and turbulent dissipation (Pollard and Millard, 1970; D'Asaro, 1989; D'Asaro et al., 1995).

The value of r is typically determined empirically to fit observations of $\bar{\mathbf{u}}$, which can yield timescales r^{-1} that range from 8 hours to 8 or more days (Pollard and Millard, 1970; Alford and Gregg, 2001; Guan et al., 2014). This broad range may be due to the fact that r is meant to represent the effects of all dynamics ignored in equations (1.6) and (1.7). Previous studies have sought to derive scalings of the type $r^{-1} \sim E_{NIW}/F_{NIW}$, where E_{NIW} is the near-inertial energy and F_{NIW} is the corresponding energy flux (Gill, 1984). However, such derivations are necessarily incomplete and depend on assumptions about the physical process by which NIWs develop horizontal gradients and their corresponding group velocity ($\mathbf{c_g}$). In the mid latitudes, this reduction of horizontal scales is thought to depend on gradients in the mesoscale and planetary vorticity (Kunze, 1985; D'Asaro, 1989; Johnston et al., 2016; Asselin and Young, 2020; Thomas et al., 2020), while the spatial structure of TC winds imprints sharp gradients on upper ocean currents and thus allows for more rapid generation of NIWs (D'Asaro, 1989). To emphasize this feature of NIW generation by TCs, we now consider the ML response to τ not in terms of $\bar{u}$ and $\bar{v}$, but their spatial gradients. The final aim here is to elucidate the drivers of inertial pumping in $\frac{\partial h}{\partial t}$, by which NIW energy propagates into the thermocline.

1.2.1 Dynamics of wind-forced gradients in the upper ocean

Below, we manipulate equations (1.6)-(1.8) to isolate the components that contribute to $\frac{\partial h}{\partial t}$ and thus generate NIWs. To do this, we calculate $\frac{\partial \zeta}{\partial t} = \nabla \times \frac{\partial \bar{\mathbf{u}}}{\partial t}$ and study its relation to $\frac{\partial \Gamma}{\partial t} = \nabla \cdot \frac{\partial \bar{\mathbf{u}}}{\partial t}$. Taking the curl and divergence of equations (1.6) and (1.7) thus yields an alternative representation of ML dynamics

$$\frac{\partial \zeta}{\partial t} = -f\Gamma + \frac{1}{\rho_0 h}\left(\nabla \times \tau - \frac{\tau}{h} \times \nabla h\right) - r\zeta \tag{1.9}$$

$$\frac{\partial \Gamma}{\partial t} = f\zeta + \frac{1}{\rho_0 h}\left(\nabla \cdot \tau - \frac{\tau}{h} \cdot \nabla h\right) - r\Gamma \tag{1.10}$$

$$\frac{\partial h}{\partial t} + h\Gamma = W_e. \tag{1.11}$$

This formalism does not explicitly include information about the magnitude and direction of currents. Instead, it uses the physical principles in equations (1.6)-(1.8) to resolve spatiotemporal patterns in $\frac{\partial h}{\partial t}$ that generate internal waves. While past studies have used ζ and Γ as the basis of fluid dynamical models (Névir and Sommer, 2009; Salmon, 2007), these variables are particularly relevant to NIW generation and their interaction with background flows (Gill, 1984; Nagai et al., 2015; Whitt and Thomas, 2015). Furthermore, note that under axial-symmetric storms, $\nabla \cdot \tau$ and $\nabla \times \tau$ are fully determined by radial and tangential winds respectively. Thus, equations (1.9) and (1.10) show how these separate components of τ directly drive orthogonal but coupled modes of motion Γ and ζ in the ML.

In TC wakes, once winds cease to play a dominant role and the ML evolves freely, our diagnostic model (1.9)-(1.11) yields the three term balance

$$\frac{\partial \zeta}{\partial t} = -f\Gamma - r\zeta \tag{1.12}$$

$$\frac{\partial \Gamma}{\partial t} = f\zeta - r\Gamma. \tag{1.13}$$

This linear system of equations, a damped harmonic oscillator, produces inertial cycles in ζ and Γ with an exponential decay rate r. Inertial pumping arises directly from these cycles, which are simply a consequence of clockwise rotation in $\bar{\mathbf{u}}$ over time at a given point in the TC wake. To visualize how equations (1.12) and (1.13) are an explicit statement of inertial pumping, we follow Gill (1984) and set $\tau = W_e = r = 0$ to consider an initial condition $(\zeta_i, \Gamma_i) = (c_i, 0)$ at time $t = t_i$, where $c_i > 0$. As illustrated in Fig. 1.4, equations (1.12) and (1.13) imply that inertial rotation of current vectors transforms ζ into Γ and Γ into $-\zeta$ at time intervals $\sim \frac{\pi}{2f}$. Quadrature between ζ and Γ in this oscillatory mode means that NIW crests and troughs (maximum upward

and downward displacements of the ML base) must be surrounded by anticyclonic and cyclonic inertial currents respectively (Fig. 1.4).

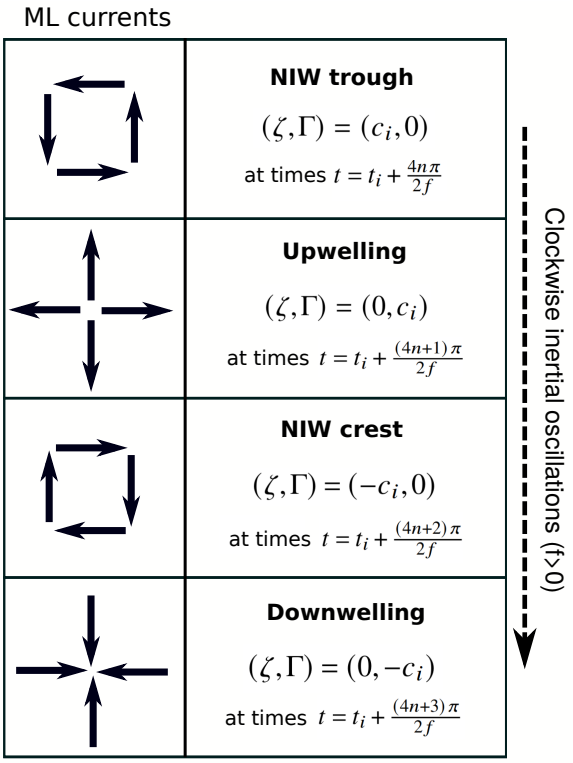

Figure 1.4. Successive rows illustrate the time evolution of current vectors under clockwise inertial oscillations. The left column shows schematic vews of $\mathbf{u}$ at temporal intervals $\frac{n\pi}{2f}$ ($n = 0, 1, 2, \ldots$). Over this period, clockwise rotation of $\mathbf{u}$ by 90° fully transforms ζ into Γ, and Γ into $-\zeta$.

1.2.2 Relating upwelling and NIW generation to TC winds

When winds act on the ocean surface, $\overline{\mathbf{u}}$ initially accelerates in the direction of τ while turbulence helps distribute momentum vertically and deepen the ML. Later on, $\overline{\mathbf{u}}$ undergoes inertial rotation and becomes misaligned with τ. Variations in the alignment between τ and $\overline{\mathbf{u}}$ play a crucial role in setting the ocean response to TCs, as misalignment gives rise to an asymmetric distribution of ML energy around the TC track (Chang and Anthes, 1978) and can stop ML deepening by turbulence when $\overline{\mathbf{u}}$ approaches Ekman's balance and the rate of wind work $\tau \cdot \overline{\mathbf{u}}$ vanishes (Ekman, 1905; Pollard et al., 1973).

Setting $\nabla h = 0$ in equations (1.9)-(1.11), we may write the Ekman balance as $(\zeta, \Gamma) \sim \frac{1}{f\rho_0 h}(-\nabla\cdot\tau, \nabla\times\tau)$, so that Γ (and the resulting upwelling) is sustained by $\nabla\times\tau$. However, notice that $\nabla\times\tau$ does not directly drive the evolution of Γ in equation (1.10). Instead, $\frac{\partial\zeta}{\partial t}$ and $\frac{\partial\Gamma}{\partial t}$ will mirror patterns in $\nabla\times\tau$ and $\nabla\cdot\tau$ respectively at the initial stages of TC forcing. It is only later that the inertial rotation of currents gradually links $\nabla\times\tau$ to Γ and produces upwelling (Fig. 1.4).

The relative magnitude of steady (Ekman) and oscillating (NIWs) components of the ocean response to TC forcing is determined by U_{storm}, $\mathbf{c_g}$, and the horizontal scale of τ. Using a two-layer model, Geisler (1970) showed that energy transfer into NIWs decreases with the ratio $U_{storm}/\mathbf{c_g}$. At the limit where $U_{storm}/\mathbf{c_g} < 1$ (slow-moving TCs), Geisler's solutions predict that the momentum in $\nabla\times\tau$ is entirely used by Ekman-style upwelling with no oscillatory behavior. Nilsson (1995) later generalized this result by deriving analytical expressions for the power put into geostrophic and NIW modes in a continuously stratified fluid given $\mathbf{c_g}$, U_{storm}, and the wavenumber spectrum of τ.

The formalism in equations (1.9)-(1.11) does not explicitly represent $\mathbf{c_g}$, but instead uses r to parameterize Eulerian momentum decay. Hence, we investigate how the value of r influences the relative roles of NIW generation and net upwelling as described by the (ζ, Γ) slab model. To do this, we used Euler's method to compute point solutions (solving with no space dependence, such that $\nabla h = 0$) of the slab model under the forcing of a Gaussian vortex $\nabla\times\tau$ (Fig. 1.5a). This represents the changing direction of tangential τ inside an axisymmetric TC eye but does not include radial stresses $\nabla\cdot\tau$, which are known to make only minor contributions to NIW generation under TCs (Price, 1983; Shay et al., 1989; Nilsson, 1995). The evolution of $(\zeta/f, \Gamma/f, h)$ from an initial condition $(0, 0, 80\text{ m})$ using f at 15.5°N and $r \in [0.3f, 0.7f]$ is shown in Figs. 1.5b,c.

Numerical solutions show that increasing the value of r weakens near-inertial oscillations in ζ/f, Γ/f, and $h(t)$, and enhances the net ML displacement $h(t_0) - h(t)$ at long times (Fig. 1.5). Namely, greater values of r produce an ocean response that is akin to that of storms with

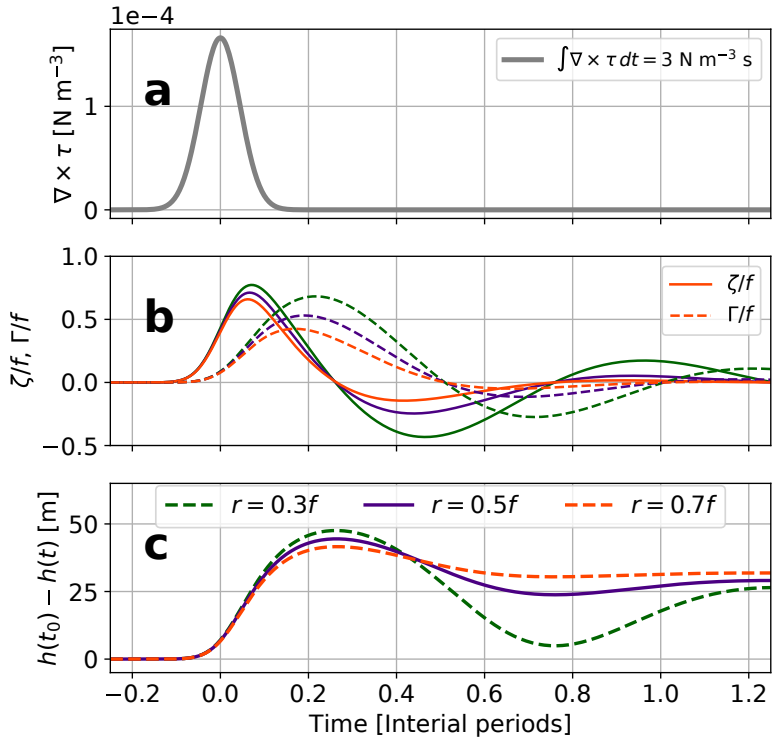

Figure 1.5. ML response (1.9)-(1.11) to (**a**) wind vortex representing the radial wind stress of an axisymmetric TC. (b) shows the evolution of ζ/f (solid lines) and Γ/f (dashed lines) for damping parameters $r = 0.3f$, 0.5f, and 0.7f in green, purple, and orange, respectively. (**c**) shows corresponding solutions of the mixed layer displacement $h(t_0) - h(t)$ when $W_e = 0$.

lower $U_{storm}/\mathbf{c_g}$, as $h(t_0) - h(t)$ continues to oscillate after its maximum displacement if $r = 0.3f$, but converges shortly after its peak when $r = 0.7f$. This suggests that the sensitivity of the (ζ, Γ) slab model in equations (1.9)-(1.11) to the damping parameter r is consistent with the notion developed around the (u, v) model that r is directly proportional to $\mathbf{c_g}$ and helps parameterize its effects. Namely, underlying ocean conditions impacting the partition of energy between geostrophic and NIW modes in TC wakes can be partly represented by tuning r.

The linear (ζ, Γ) view of ML dynamics in equations (1.9)-(1.11) does not include any new physics absent from standard ocean models based on (u, v). Rather, it uses a simple change of variables to explain inertial pumping (Fig. 1.4) using ordinary differential equations instead of partial ones, as done by Gill (1984). This helps conceptualize inertial pumping and upwelling as 1D (rather than 3D) processes. Furthermore, coupling between ζ and Γ concretely explains why

NIW wakes are generally centered along the TC track where $\nabla \times \tau$ peaks and not on its right side, where the greatest concentration of near-inertial energy is (Price, 1981, 1983). Namely, NIWs only form where horizontal gradients (ζ and Γ) exist, and the forcing $\nabla \times \tau$ that directly drives cycles in ζ and Γ is greatest along the track.

Overall, numerical solutions in Fig. 1.5 show that equations (1.9)-(1.11) can reproduce inertial pumping and upwelling under TCs but rely on tuning of the parameter r. Furthermore, note that the 1D approach used here does not include the effects of pressure gradients and horizontal advection, which may have greater relevance under slow-moving TCs ($U_{storm}/\mathbf{c_g} \leq 1$). In the next section, we use float measurements and output from WRF-HYCOM coupled simulations of Mangkhut ($U_{storm}/\mathbf{c_g} \sim 2$) to demonstrate the relevance of equations (1.9)-(1.11) and (ζ, Γ) coupling (Fig. 1.4) in describing NIW generation under fast-moving TCs.

1.3 Upper ocean dynamics beneath Mangkhut

We now turn our attention towards model output and observations of upper ocean dynamics beneath Super Typhoon Mangkhut. First, we present evidence supporting the validity of sampling and interpolation schemes described in Section 2. Second, the evolution of ζ and Γ, and their effect on T and S in our observations is explained using numerical solutions of equations (1.9)-(1.11). Altogether, these analyses exemplify and expand on the dynamics described in Section 3 and help visualize the mechanisms of NIW generation under fast-moving storms. The role of turbulent mixing in changing h is discussed briefly.

Mechanisms of NIW generation in model output and observations are compared (Fig. 1.6c) using a time series of the modelled $(\zeta, \Gamma)/f$ averaged between 14 and 14.5°N (solid lines) and float estimates ζ^*_{surf}/f along $y = 0$ (dashed lines). Much like the idealized solutions in Figs. 1.4 and 1.5b, the ML response to Mangkhut can be described as a combination of initial forcing by $\nabla \times \tau$ and later coupling between ζ/f and Γ/f by inertial rotation of $\overline{\mathbf{u}}$. Atmospheric forcing is evidenced by a peak in ζ/f under the TC eye, while inertial rotation later transformed this

response into a peak in Γ/f (Fig. 1.6c). As $\overline{\mathbf{u}}$ continued to rotate, ML flows reorganized to form minima in ζ/f and Γ/f along the TC track (Figs. 1.6a,b). At the end of the first inertial cycle, the ML came to have $\zeta/f \approx 0.25$ and $\Gamma/f \approx 0$ in both the 3D model and observations (Figs. 1.6c).

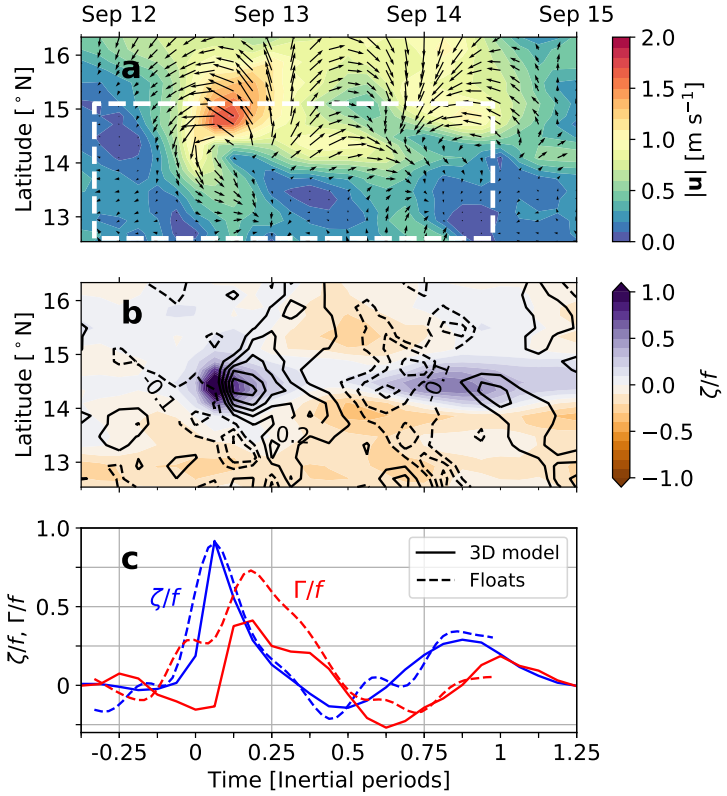

Figure 1.6. Hovmöller diagrams of the ML flow along 133 °E in terms of (**a**) $\overline{\mathbf{u}}$ and (**b**) $(\zeta,\Gamma)/f$ from the 3D coupled model, where Γ/f is contoured at 0.1 intervals (dashed/solid for negative/positive values). (**c**) Modelled $(\zeta,\Gamma)/f$ averaged between 14 and 14.5°N (solid lines) is compared to observed values along $y = 0$ (dashed lines). The dashed rectangle in panel **a** is representative of the area and stages of ocean response sampled by floats (Fig. 1.2b).

Broadly speaking, spatial patterns in $\|\overline{\mathbf{u}}\|$ and $(\zeta,\Gamma)/f$ in observations (Fig. 1.7) are consistent with those in the 3D model (Fig. 1.6a,b). Yet, some notable differences between the modelled and observed ML response exist. For example, $\Gamma^*_{surf}/f \sim 0.25$ near the leading edge of the TC eye (Fig. 1.7c), but the 3D model yields $\Gamma_{hycom}/f \sim -0.1$ there (Fig. 1.6b). Available

data is insufficient to reliably attribute such differences to potential biases induced by windage and wave motion, our sampling and interpolation scheme, or to processes misrepresented in the 3D model. Nevertheless, patterns in $\mathbf{u}^*_{surf}$ and $\mathbf{u}^*_{mean}$ (Fig. 1.7a,b) are qualitatively similar to each other, suggesting that windage and wave motion only had a limited impact on $\mathbf{u}^*_{surf}$.

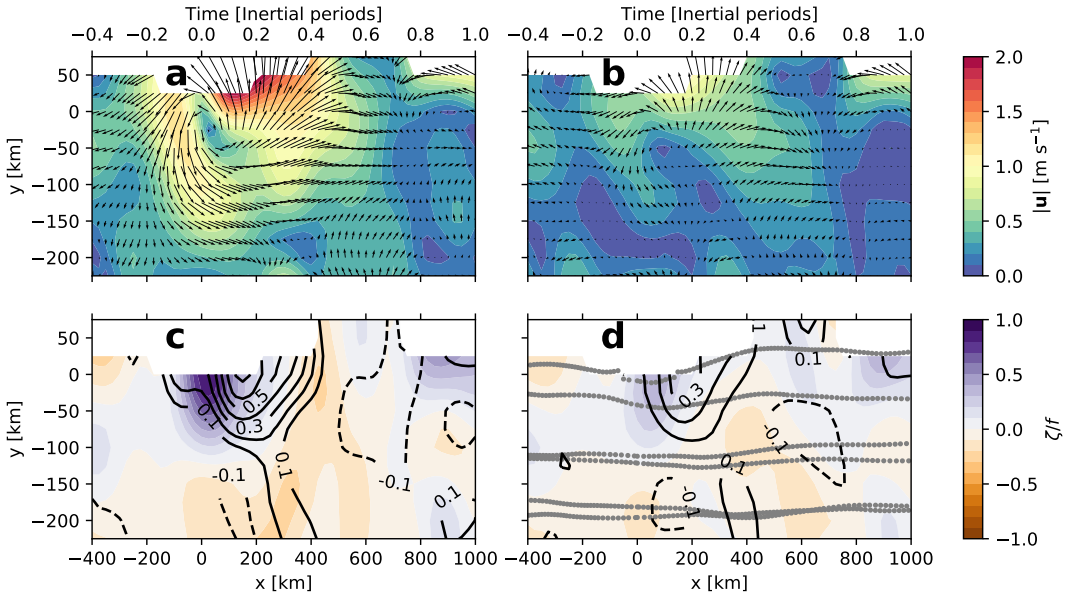

Figure 1.7. Observed ML dynamics under Mangkhut. (**a**) $\mathbf{u}^*_{surf}$ and (**b**) $\mathbf{u}^*_{mean}$ show current speeds in color shading. (**c**) ζ^*_{surf}/f and Γ^*_{surf}/f, and (**d**) ζ^*_{mean}/f and Γ^*_{mean}/f show the gradient-based description of ML motions. Black solid contours in Figs. 1.7c,d are for upwelling-favorable values $\Gamma/f > 0$, while dashed contours show $\Gamma/f < 0$, and gray dots in Fig. 1.7d show the locations of float profiles.

With the validity of our observational technique supported by model results, we now put our focus on the coupling between ζ/f and Γ/f and how it leads to NIW generation. To test whether observations are consistent with linear theory, Fig. 1.8 compares mapped float data along $y = 0$ to numerical solutions of equations (1.9)-(1.11) under idealized forcing and with $r = 0.5f$.

Atmospheric forcing by $\nabla \times \tau$ in Fig. 1.8 corresponds to the reversal of tangential wind between opposite sides of the TC eyewall. The magnitude of $\nabla \times \tau$ used here agrees with the mean wind stress curl across the TC eye ($\frac{|\tau_{\mathbf{max}}|}{\mathrm{MWR}} = 2.24 \times 10^{-4}$ N m^{-3}, dashed line), where

$MWR = 40$ km is the radius of maximum wind and $|\tau_{max}| = C_D \rho_{air} |U_{10}|^2$ was calculated using $U_{10} = 70$ m s^{-1} (Fig. 1.1), $\rho_{air} = 1.22$ kg m^{-3}, and $C_D = 1.5 \times 10^{-3}$ (Zweers et al., 2010).

The magnitude of convergent stresses $\nabla \cdot \tau < 0$ is set to be artificially low in these simulations (Fig. 1.8a). Although $\|\nabla \cdot \tau\| \sim \|\nabla \times \tau\|$ in the 3D atmospheric model, the response in Γ that is generated by $\|\nabla \cdot \tau\|$ is rapidly suppressed by 3D and nonlinear effects and thus does not contribute significantly to NIW generation in the TC wake (Price, 1983; Shay et al., 1989). Lastly, it should be noted that forcing in Fig. 1.8a ignores the gradual weakening of τ far from the eyewall, where $\nabla \times \tau < 0$ and $\nabla \cdot \tau > 0$.

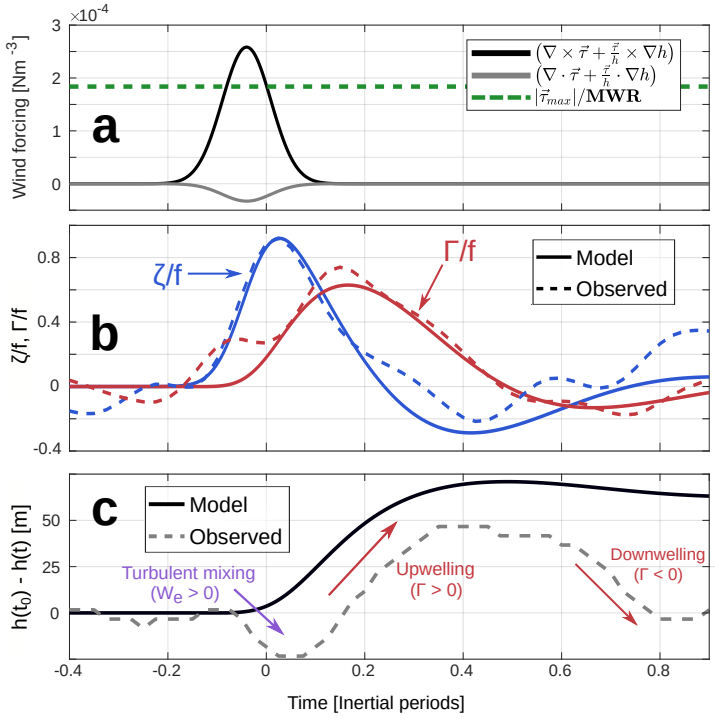

Figure 1.8. ML response to idealized TC-like atmospheric forcing. (**a**) Idealized wind forcing (solid lines) used to drive the ML linear model in equations (1.9)- (1.11) setting $W_e = \nabla h = 0$ and $r = 0.5f$. The dashed green line indicates the mean wind stress curl $\|\tau_{max}\|/MWR$ of the TC eye. (**b**) Numerical solutions of ζ/f (blue) and Γ/f (red) are compared to observations ζ_{surf}/f and Γ_{surf}/f along $y = 0$ km (Fig. 1.7c). (**c**) Linear solutions of $h(t)$ (solid line) are compared to observed displacements of the 27°C isotherm (dashed line).

Agreement between linear solutions and observations in Fig. 1.8 confirms that clockwise rotation of $\bar{\mathbf{u}}$ (Fig. 1.2b) transformed the wind-forced ζ into Γ near the end of the forced stage.

Momentum in Γ was later transferred to an inertial anticyclone $\zeta < 0$ and the cycle continued as shown schematically in Fig. 1.4. Note that the quality of the fit in Fig. 1.8b is sensitive to various model parameters (r, $\nabla \times \tau$, $\nabla \cdot \tau$), and initial conditions for (ζ, Γ, h). Nonetheless, this analysis confirms that ζ and Γ oscillate in quadrature in observations, the 3D model, and linear theory (Figs. 1.6c, 1.8b). This robust result comes from the linear terms by which f couples u and v in equations (1.6) and (1.7), and ζ and Γ in equations (1.9) and (1.10).

When Earth's rotation transferred ζ into Γ, the ML base moved upwards and a NIW was generated (Figs. 1.8c, 1.9a). Observations show that the 27°C isotherm deepened by $\sim$25 m under the TC eye before it shoaled by 75 m as predicted by linear theory (Fig. 1.8c). Initial deepening may be partially explained by turbulent mixing, evidenced by Thorpe scale estimates $\kappa \sim 10^{-1}$ m^{2}s^{-1} near $x = 0$ km (Fig. 1.9b). Agreement between the modelled $\frac{\partial h}{\partial t}$ and observed displacements of the 27°C isotherm behind the TC are consistent with Γ^*_{surf} there (Fig. 1.8c). This result implies that upwelling in the wake of Mangkhut resulted from the near-inertial coupling of ζ and Γ, marking the generation of a large amplitude NIW. Moreover, the modelled Γ agrees well with Γ^*_{surf} for all $t > 0$ (Fig. 1.8b). However, Γ^*_{surf} failed to capture downwelling necessary to displace h after $t \approx 0.6$ inertial periods (Fig. 1.8c).

Profiles of w^* and u^* in Fig. 1.9a reveal the structure of upwelling in the wake of Mangkhut. There, w^* reaches 8 m h^{-1} and explains isothermal displacements as large as 75 m around $x = 350$ km. T^* shows that isotherms had been lifted by $\sim$ 20 m after $\sim$0.85 inertial periods ($x = 850$ km, Fig. 1.9a), indicating that the oscillatory NIW displacement is $\sim$55 m from crest to trough. Net upwelling of isotherms in TC wakes is evidence of geostrophic adjustment (Geisler, 1970; Nilsson, 1995), which is regulated in (1.10)-(1.11) by the magnitude of r for a given atmospheric forcing (Fig. 1.5c).

To test the impacts of advection in setting the ocean stratification behind Mangkhut, as well as the accuracy of inferred 3D flows (Eqs. 1.1-1.3), the Eulerian heating rate $\frac{\partial H_c}{\partial t} = \rho_0 C_p \frac{\partial T^*}{\partial t}$ is calculated along $y = 0$ through two different methods (Fig. 1.9b). First, we used a frozen field

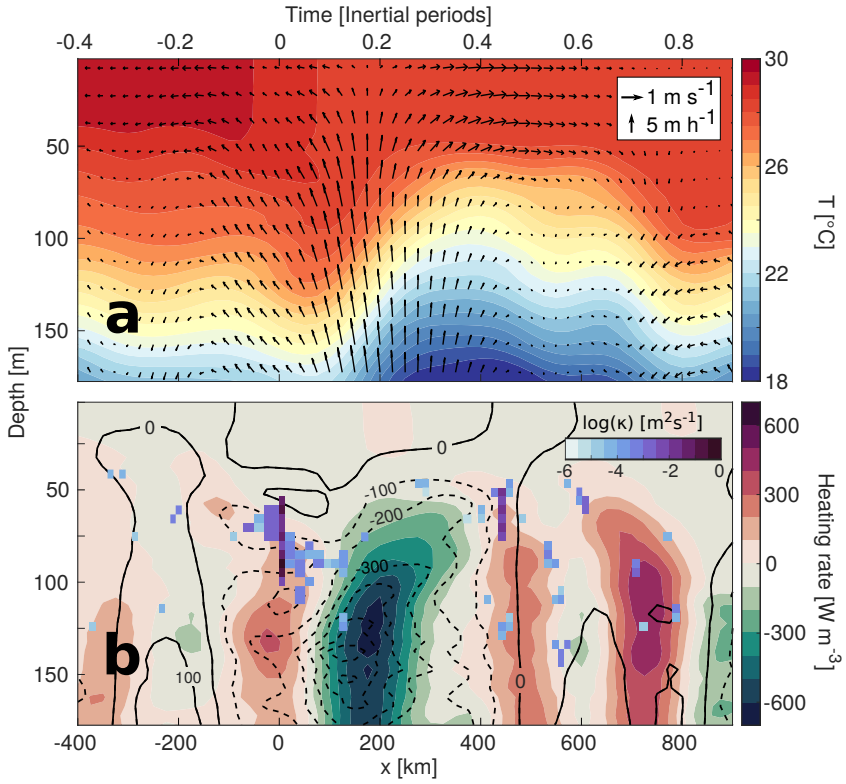

Figure 1.9. (**a**) Vertical sections of T^* and (u^*, w^*) along y=0 show the generation of a NIW behind Mangkhut. The vertical component w^* is magnified for clarity. (**b**) The Eulerian heating rate $\frac{\partial H_c}{\partial t}$ estimated using $\frac{\partial T^*_{\text{frozen}}}{\partial t}$ (color shading) and $\frac{\partial T^*_{\text{adv}}}{\partial t}$ (black contours), while estimates of κ indicate the intensity of vertical mixing inferred from Thorpe scales in M3 data (note the log scale).

assumption so that $\frac{\partial T^*_{\text{frozen}}}{\partial t} = U_{storm}\frac{\partial T^*}{\partial x}$ (color shading). Second, we used $\mathbf{u}^*$ and w^* to calculate the advective contribution $\frac{\partial T^*_{\text{adv}}}{\partial t} = -u^*\frac{\partial T^*}{\partial x} - v^*\frac{\partial T^*}{\partial y} - w^*\frac{\partial T^*}{\partial z}$ (black contours). Note that the latter expression ignores heating by turbulent mixing, while the frozen field estimate accounts for all observed heat transfer.

Areas of agreement between both estimates of $\frac{\partial H_c}{\partial t}$ (color shading and black contours in Fig. 1.9b) suggest that heat transfer was locally dominated by the vertical advection term $w^*\frac{\partial T^*}{\partial z}$ and that the approximation w^* is adequate. Similarities are particularly good near $x = 180$ km, where upwelling caused $\frac{\partial H_c}{\partial t} \sim$ -500 W m^{-3}.

Advective estimates of $\frac{\partial H_c}{\partial t}$ mistakenly predict cooling below 75 m depth around $x = 0$, where T^* shows heating rates as high as 300 W m^{-3} (color shading). Disagreement between

observed heating and advective estimates below the TC eye may be explained by a possible bias in Γ^*_{surf} (Fig. 1.6c) but also by vigorous mixing. Thorpe scale estimates $\kappa \sim 10^{-1}$ m^2 s^{-1} near $x = 0$ (Fig. 1.9b) reveal areas where the corresponding turbulent heat flux $J_q \sim 4000$ W m^{-2} (Eq. 1.5) could invalidate the assumption that $\frac{\partial H_c}{\partial t}$ was dominated by advection.

While variations in the ML flow are dominated by near-inertial oscillations (Fig. 1.8), $\frac{\partial H_c}{\partial t}$ also shows the signature of higher-frequency motions (Fig. 1.9b). Horizontal sections of $\zeta^*/f, \Gamma^*/f$, and N^* at 160 m depth (Fig. 1.10) feature nearly parallel, periodic stripes that move away from the storm track towards $y < 0$. Dashed black lines in Fig. 1.10 help identify this apparent propagation corresponding to a cross-track phase speed ~ 3.1 m s^{-1}. While ζ^*/f and Γ^*/f are linked by the rotation of current vectors (Fig. 1.4), Γ^* and N^* are linked by isopycnal displacement and straining. Therefore, these three variables offer complementary views of internal wave phase propagation.

The difference between surface and vertically-averaged velocities $\|\mathbf{u}^*_{surf} - \mathbf{u}^*_{mean}\|$ is a proxy for vertical shear below the ML (Fig. 1.10c), which drives turbulent mixing in TC wakes (Price, 1981). Thorpe scale estimates of ε in individual overturns are shown with colored circles (Fig. 1.10c), with their greatest values and concentration appearing within 100 km of the TC eye. Ahead of the TC, overturns with $\varepsilon < 10^{-7}$ W kg^{-1} were sampled at nearly equidistant locations by floats M3, M6, and M0. Conversely, overturns in the TC wake appeared more sporadically and clustered around a few locations, but with most values of ε ranging between 3×10^{-7} and 10^{-6} W kg^{-1}.

1.4 Upper ocean thermodynamics beneath Mangkhut

1.4.1 Mixed layer deepening and turbulent entrainment

Space-time variations in subsurface T and S result from 3D advection, mixing, and interactions with the atmosphere. In the case of intense, fast-moving TCs like Mangkhut ($U_{storm}/\mathbf{c_g} \sim 2$), shear-driven mixing at the ML base is expected to dominate upper ocean cooling

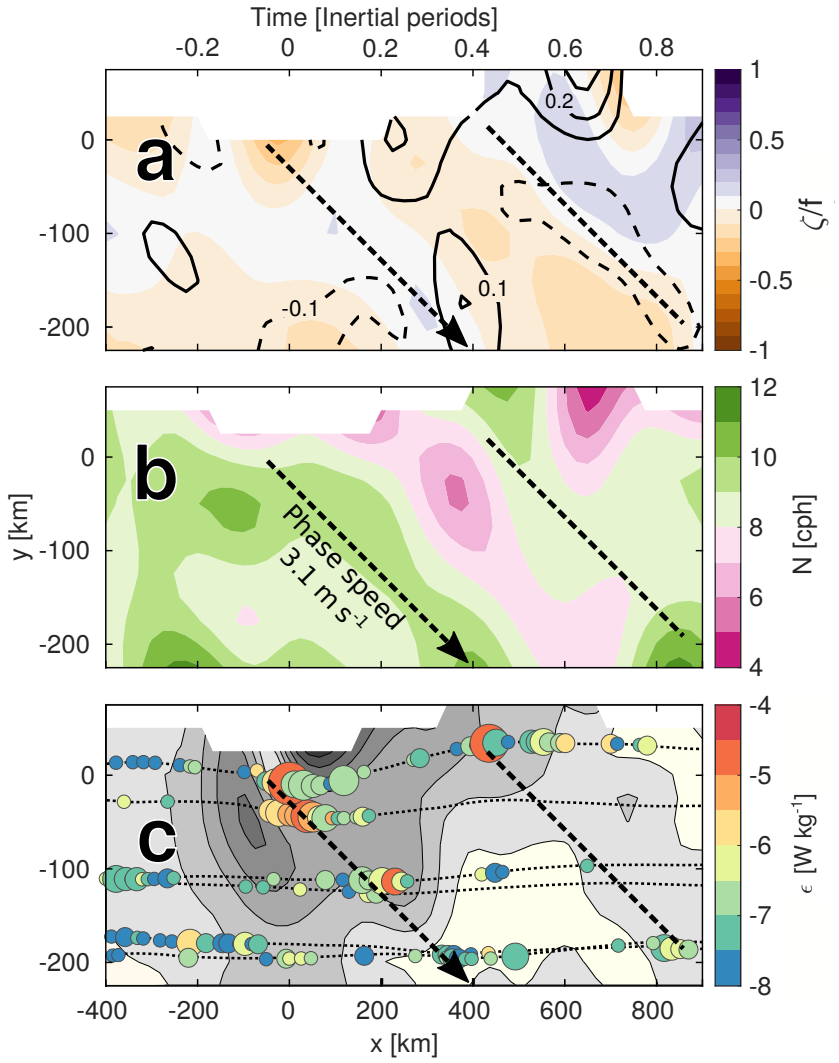

Figure 1.10. Horizontal sections of dynamical variables at 160 m depth. (**a**) ζ^* (color) and Γ^* (black contours, negative dashed), (**b**) N^*, and (**c**) $\|\mathbf{u}^*_{surf} - \mathbf{u}^*_{mean}\|$ (gray shading at 0.2 m s^{-1} intervals), which is a proxy for vertical shear at the ML base. The colors of circles in Fig. 1.10.**c** indicate ε estimated for individual overturns. The size of circles indicates overturn size (given by the maximum d'), which ranges between 5 and 25 m. Thin, dotted lines denote individual float tracks. Note that scales differ in x and y.

(D'Asaro, 2003; Vincent et al., 2012a). This process is evidenced by float measurements of T averaged between 0.5 and 1.5 m depth (Fig. 1.11a), which show a general cooling trend during TC passage.

In particular, 1-m binned profiles of T, S and potential density (σ_θ) from float M3 show a clear, gradual deepening of the ML base between $x = -250$ and $x = 0$ km (Figs. 1.11b-d).

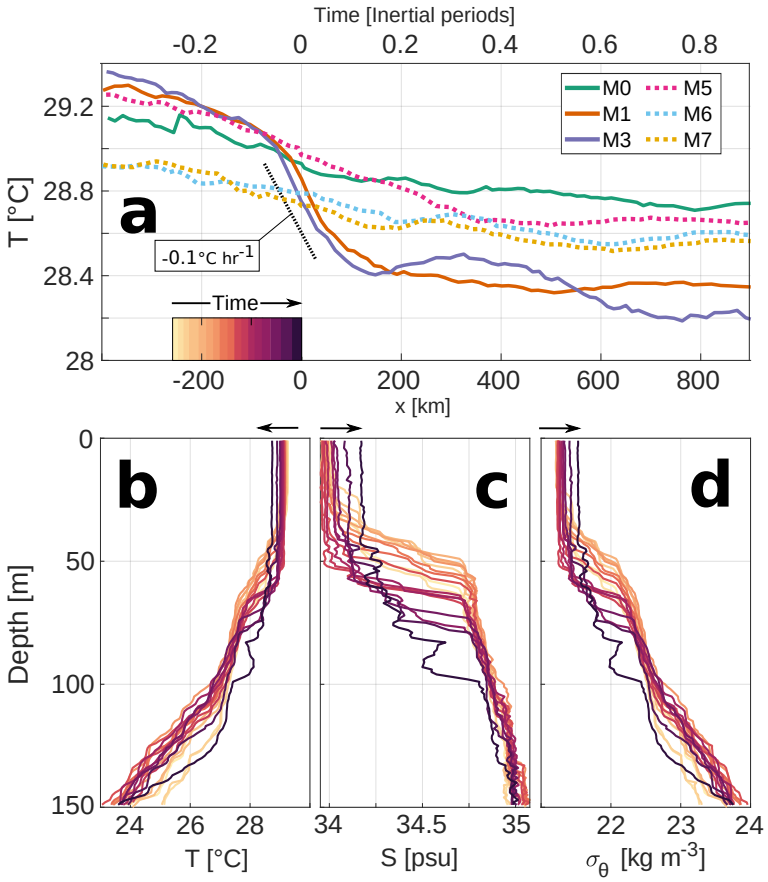

Figure 1.11. SST cooling by turbulent entrainment. (**a**) SST measured by all floats as a function of along-track distance x. 1-m binned profiles of (**b**) T, (**c**) S, and (**d**) potential density σ_θ measured by float M3 between $x = -250$ and $x = 0$. Individual profiles shown in the lower panels are color coded by their position in x (color bar in panel a).

Successive float profiles in Figs. 1.11b-d show cooling trends in SST but increasing sea surface salinity (SSS) and σ_θ as the ML deepened. This corresponds to entrainment of cold, salty water from below and implies that a fraction of turbulent kinetic energy in wind-driven currents was used to raise the potential energy (PE) of the water column. In fact, density data (ρ) from floats M1 and M3 indicate that $PE^0_{-60} = \int_{-60}^{0} \rho g z dz$ in the upper 60 m increased by ~ 9 and 10×10^3 J m^{-2} between $x = -200$ and 200 km respectively.

As further evidence of the vigorous turbulence that transformed ocean thermodynamics beneath Mangkhut, vertical profiles of σ_θ feature $\sim$10 m-tall regions with unstable stratification (i.e. $\frac{\partial \sigma_\theta}{\partial z} > 0$, Fig. 1.11d). Thorpe scale estimates (see Section 2.2) in Figs. 1.9b and 1.10c

indicate the contribution of these density overturns to ocean turbulence. Overall, the distribution and magnitude of turbulent patches agree with the timing of ML deepening and SST cooling (Figs. 1.8c, 1.11a). We estimate the turbulent heat flux $J_q \sim 4000$ W m^{-2} out of the ML for float M3 near $x = 0$ km (given $\kappa \sim 0.1$ m^2 s^{-1} and $\frac{\partial T}{\partial z} \sim 0.01$ °C m^{-1} in equation 1.5). For a ML with $h = 40$ m, this value of J_q corresponds to an SST cooling rate ~ -0.1 °C hr^{-1}, consistent with observations in Fig. 1.11a. The corresponding salinity flux $\kappa \frac{\partial S}{\partial z}$ is $\sim 1 \times 10^{-3}$ psu m s^{-1} out of the ML, equivalent to a rate of increase ~ 0.1 psu hr^{-1}, also consistent with observations by M3 (Fig. 1.12a).

After storm passage, SSS (SST) had increased (decreased) for all floats (Figs. 1.11a, 1.12a), indicating widespread mixing of the upper ocean beneath Mangkhut. In fact, plan views of near-surface $T^*(x,y)$ and $S^*(x,y)$ in Fig. 1.13 reveal a narrow and asymmetric wake of cold, salty water. This indicates that SST cooling was dominated by turbulent mixing and is consistent with greater windwork and current speeds for $y > 0$ (Figs. 1.6a, 1.7a,b, Chang and Anthes 1978; Price 1981). Furthermore, gradients $\frac{\partial T^*}{\partial x}$ and $\frac{\partial S^*}{\partial t}$ (not shown) indicate that maximum mixing rates occurred within 100 km of the TC eye, in agreement with Thorpe scale estimates in Figs. 1.9b and 1.10c.

The impact of precipitation on S in the upper 5 m is opposite to that of mixing and thus can be assessed from Fig. 1.12a, as floats M5, M6 and M7 sampled sharp decreases in near-surface S between $x = -250$ and $x = -150$ km. To examine the impacts of rainfall in near-surface T and S, we interpolated data from the Integrated Multi-Satellite Retrievals for Global Precipitation Measurement (IMERG, Huffman et al. (2015)) onto the times and locations of float measurements. Estimated hourly rates of precipitation and cumulative rainfall integrated since floats were at $x = -400$ km show that all floats experienced considerable precipitation (Fig. 1.12b).

Despite receiving more freshwater (~ 300 mm) than any other floats, time series of near-surface S from M1 and M3 do not feature noticeable decreases attributable to precipitation (Fig. 1.12). For precipitation to noticeably impact measurements of S, surface rain layers must

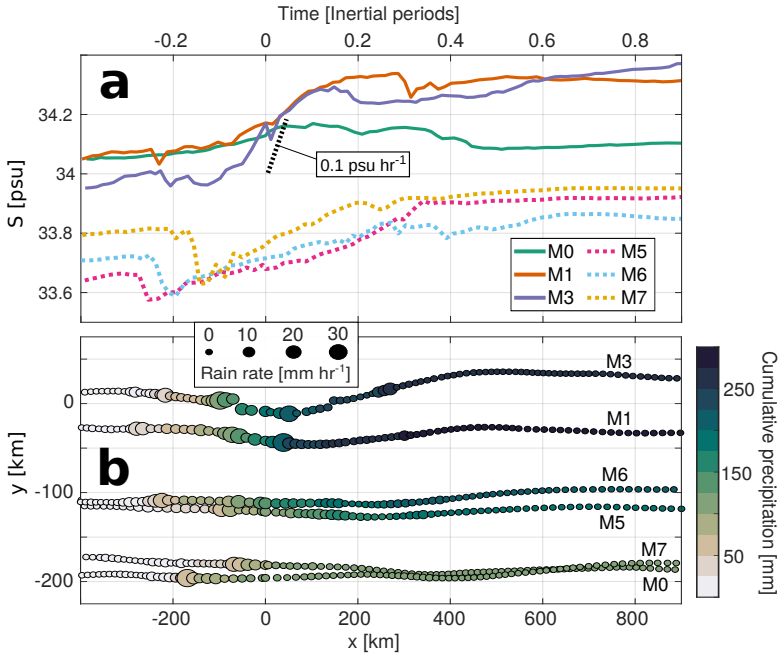

Figure 1.12. (**a**) S averaged in the upper 5 m along float tracks increases as a response to mixing of subsurface waters and decreases due to rainfall. (**b**) IMERG data show rain rates and cumulative precipitation along float trajectories.

form and remain stable for a period of time long enough ($>$ 30 minutes) to be sampled by floats. However, this is only possible when buoyancy production by rainfall is greater than buoyancy mixing rates that diffuse salinity gradients (Thompson et al., 2019). Given that floats M1 and M3 were near the TC track and experienced the greatest turbulence rates (Fig. 1.10c), it is likely that sudden SSS freshening by rainfall was quickly mixed before it could be sampled.

Successive profiles of T and S by float M7 (Fig. 1.14) detail the process of rain layer formation and their subsequent destruction by turbulent mixing. Each row of plots in this sequence shows 5 consecutive profiles spanning $\sim$ 3 h ($\sim$ 75 km). At the beginning, float profiles ranging from $x = -246$ to $x = -168$ km show a well-mixed upper ocean with no vertical gradients in T or S (Figs. 1.14a,b). Later on, a layer of water with low T and S formed in the upper 5 m around $x = -140$ km (black line) but was gradually mixed and deepened over the following casts (Figs. 1.14c,d). This rain layer accounts for the sharp decrease in SSS measured by M7 (Fig. 1.12a), while the subsequent increase in SSS was consistent with mixing of cold,

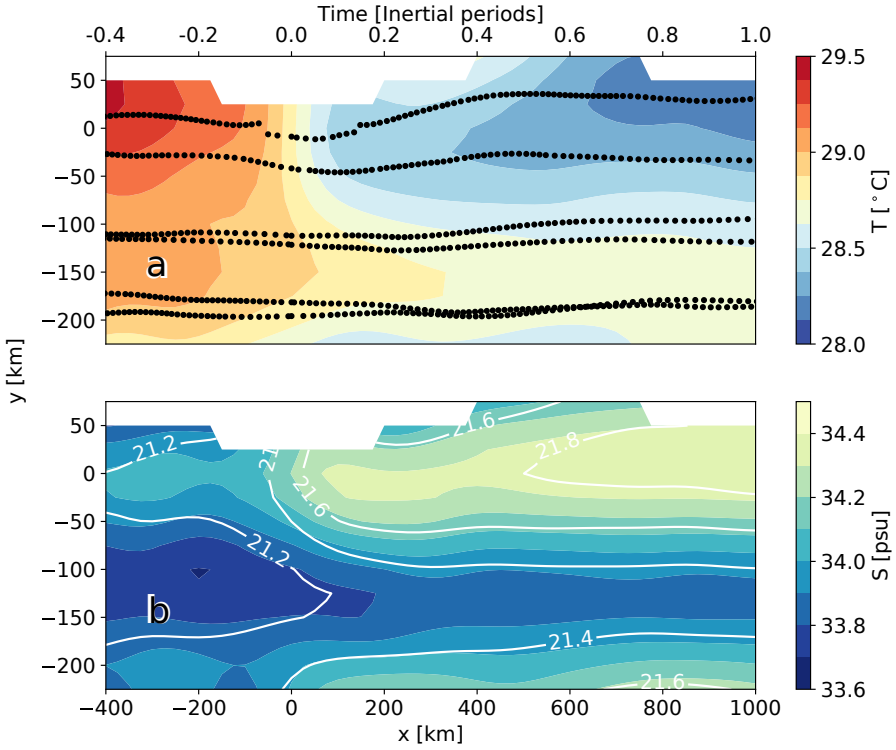

Figure 1.13. Plan view of (**a**) T^* and (**b**) S^* averaged over the upper 5 m. Black dots show the locations of each profile, while white contours in Fig. 1.13b show values of σ_θ in units of kg m^{-3}.

salty water from below. Roughly four hours (near $x = -50$ km) after its formation, there was little to no indication left that a rain layer had formed around float M7 (Figs. 1.14e,f).

Under fast-moving and high-intensity TCs like Mangkhut, precipitation can counteract some impacts of mixing, increasing S and decreasing σ_θ in the ML (Huang et al., 2009; Reul et al., 2021). Mixing a rain layer with $S = 0$ and thickness $\Delta h_{rain} = 0.3$ m (Fig. 1.12b) into a ML with $S = 34$ psu and $h = 40$ m would decrease SSS by 0.2 psu and surface σ_θ by 0.15 kg m^{-3}. This is equivalent to $\sim 60\%$ of the observed increase in SSS near the TC track (Fig. 1.12a) and $\sim 25\%$ of the observed change in surface σ_θ (Fig. 1.13b). In the case of Mangkhut, the SSS and surface σ_θ anomalies induced by rainfall were $\sim -30\%$ and $\sim -15\%$ as large as those caused by mixing.

As an indirect effect of precipitation on air-sea interaction under TCs, we now consider the energetics associated with rain layer destruction by mixing. To estimate this, we compare *PE*

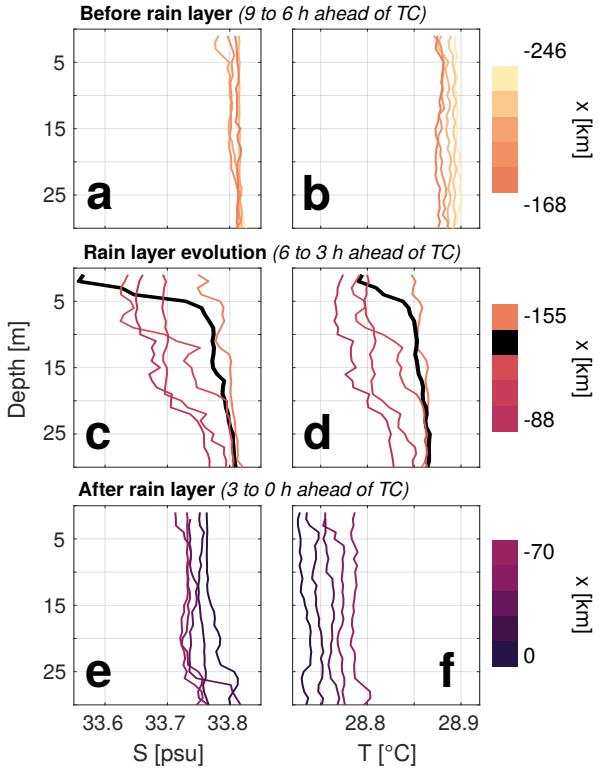

Figure 1.14. Three stages of rain layer evolution. Each row shows 5 consecutive profiles of T and S (color-coded by along-track position x) measured by float M7 over a ~ 3 h period. (**a**) S and (**b**) T before rainfall effects were noticeable. (**c**) and (**d**) show the formation of a rain layer (black line) and its gradual diffusion to greater depths. On Figs. 1.14e,f, turbulent mixing has mostly de-stratified the upper ocean.

of a water column before and after buoyancy anomalies in a rain layer of thickness Δh_{rain} have been mixed down to the ML base. For $\Delta h_{rain} = 0.3$ m, PE in the upper 60 m changes by $\sim 10^3$ J m^{-2}, roughly 10% of the change estimated between $x = -200$ and $x = 200$ km for floats M1 and M3. This suggests that rain layer destruction can take up $\sim 10\%$ of turbulent kinetic energy under TCs, therefore inhibiting further SST cooling from mixing across the ML base (Smyth et al., 1997; Jourdain et al., 2013).

1.4.2 Turbulent mixing effects on stratification

While the impacts of TC-driven turbulence are most noticeable in the formation of cold and salty wakes (Fig. 1.13), thermocline mixing by TCs helps regulate ocean heat uptake and

transport (Sriver and Huber, 2007; Jansen et al., 2010; Mei et al., 2013). To assess these effects, modellers often make assumptions about the spatial and temporal extent of anomalous κ driven by TCs. Below, we analyze observed changes in the T-S relations to infer κ in the TC wake. In this way, we retrieve information about TC-driven mixing that may not be inferred from surface or ML thermodynamics alone.

Changes in T-S relations for floats M1 and M3 (Fig. 1.15a) resulted from a combination of turbulence, 3D advection, and atmospheric fluxes. However, the effects of turbulence are distinguishable from others because mixing between two water masses produces a weighted average of the original T-S properties across contiguous layers (Hautala et al., 1996; Alford et al., 1999; Moum et al., 2003). For example, we consider the changes in average T-S properties measured by float M3 within the ranges $200 \leq x \leq 400$ km and $400 \leq x \leq 600$ km (dashed and solid lines respectively in Fig. 1.15b). To assess the role of turbulence in setting the evolution between the two T-S profiles in Fig. 1.15b, we compare observations to the evolution predicted by

$$\frac{\partial T}{\partial t} \sim \kappa \frac{\partial^2 T}{\partial z^2} \tag{1.14}$$

$$\frac{\partial S}{\partial t} \sim \kappa \frac{\partial^2 S}{\partial z^2}. \tag{1.15}$$

Equations (1.14) and (1.15) ignore the effects of 3D advection and air-sea interaction, and thus describe only the effects of mixing on T-S relations. Taking the profile observed by M3 for $x \in (200, 400)$ km as our initial condition and setting $\kappa = 3 \times 10^{-3}$ and 1×10^{-2} m^2 s^{-1} over 8 h (0.2 inertial periods) yields the T-S profiles shown in black dashed lines (Fig. 1.15b). Numerical solutions to equations (1.14) and (1.15) used boundary conditions $\frac{\partial}{\partial z} = 0$ at $z = 0$ and $z = 180$ m, implying no flux through the boundaries. Results agree well with the observed T-S changes for $\sigma_\theta < 23.2$ kg m^{-3} but fail to explain observations at greater densities (Fig. 1.15b). More precisely, note that for $\sigma_\theta > 23.5$ kg m^{-3}, the observed S was beyond the range of S in

the initial condition. Such a transformation requires input of high-S water from elsewhere and hence cannot result from vertical mixing. Altogether, these analyses suggest mixing dominated watermass transformations down to $\sim$ 110 m depth between $x = 200$ and $x = 600$ km, while 3D advection had greater impacts below.

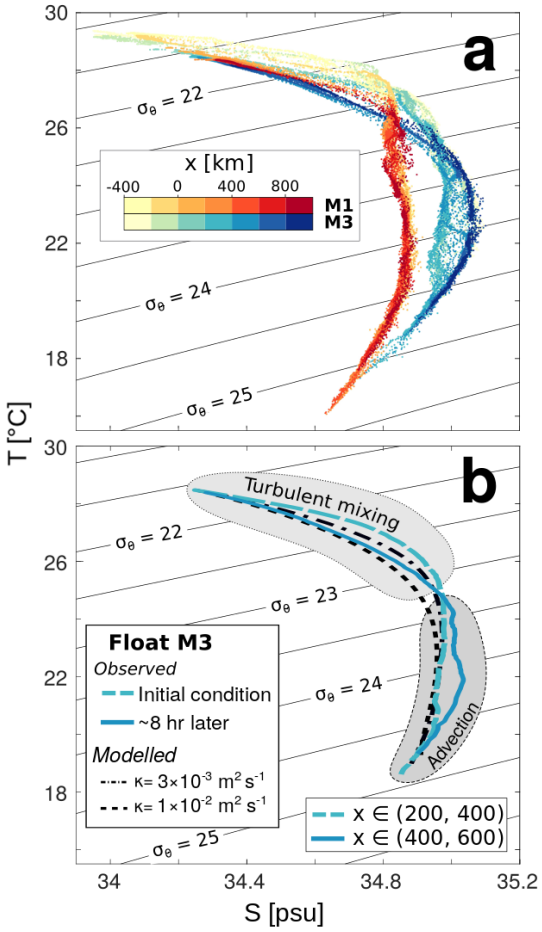

Figure 1.15. (**a**) *T-S* profiles measured by floats M1 and M3 are color-coded by x. (**b**) Mean T-S profiles for $x \in (200, 400$ km) (dashed line) and $x \in (400, 600$ km) (solid line) by float M3 show transformations caused throughout an 8 h period. Black dashed lines show T-S properties modelled using (1.14) and (1.15) under the initial condition $x \in (200, 400$ km) and different values of κ.

Values $\kappa > 10^{-3}$ m^2 s^{-1} inferred from this analysis are 3-10 times greater than the majority of Thorpe scale estimates between $x = 200$ and 600 km, whose mean value is 7.1×10^{-4} m^2 s^{-1} (Fig. 1.9b). This is not a large discrepancy given the uncertainty of Thorpe scale estimates

and the small number (< 30) of overturns detected in this range of x. Vertical profiles of $T(z)$ (not shown) that make up modelled T-S relationships in Fig. 1.15b feature negligible cooling at the surface level, but cooling of $\sim 0.2\,^{\circ}$C that peaks near 40 m depth. Areas of mixing-induced warming as large as $\sim 0.1\,^{\circ}$C appear between 60 and 100 m depth, but the majority of heat transferred downwards in solutions of equation (1.14) accumulated below 150 m, where our observations cannot help derive estimates of κ (Fig. 1.15b). Further observations are needed to better characterize the vertical extent of mixing-induced warming during this stage shortly after TC passage.

To assess the long-term impacts of 'residual' mixing in the TC wake (Fig. 1.15b), we use $\kappa = 3 - 10 \times 10^{-3}$ m^2 s^{-1} to compute J_q across the 26°C isotherm (approximately 60 m depth), yielding mean values $\langle J_q \rangle \approx 1900 \pm 1000$ W m^{-2} within $200 < x < 600$ km and $-50 < y < 50$ km. This value of is roughly three times as large as the downwelling shortwave radiative flux under clear skies in this area, which peaked near 700 W m^{-2} in shipboard observations made when the floats were deployed. Given that SST cooling typically stops only a few hours after TC passage (Figs. 1.11a), it is often assumed that TC-driven mixing stops then too. Nevertheless, these measurements (Fig. 1.15b) indicate that the vertical redistribution of heat by TC-driven turbulence lasts beyond what SST data alone would suggest. The persistence and vertical distribution of heat content anomalies days to weeks after Mangkhut was studied by Johnston et al. (2020), who highlighted advection of subsurface anomalies by the North Equatorial Current and potential interactions with subsequent TCs.

1.5 Discussion

The 3D ocean response to Super Typhoon Mangkhut was reconstructed and diagnosed using data from profiling floats. We find general agreement between interpolated fields and a 3D model (Figs. 1.6, 1.7). A linear model using ζ and Γ instead of $\overline{\mathbf{u}}$ to describe ML dynamics helped interpret measurements and identify the mechanisms driving NIW generation (Figs. 1.8,

1.9). Lastly, estimates of κ and ε based on T and S data provides insight about the spatiotemporal persistence of TC-driven mixing and impacts to upper ocean thermodynamics (Figs. 1.9b, 1.10c, 1.14, 1.15b).

1.5.1 Linear ML dynamics and inertial pumping

Our analyses describe the mechanism responsible for NIW generation by TCs. For the first time, the dynamics of inertial pumping were reduced to a set of ordinary differential equations (1.9)-(1.11) for ζ and Γ, while observations of ζ and Γ were found to be in agreement with both linear theory and a 3D model (Figs. 1.6, 1.8). The theoretical and observational results of this study are in close alignment with early analyses by Geisler (1970) and Price (1981, 1983), meaning that we have not unveiled any new physics. Rather, the significance of this study is in pointing out the inertial coupling between ζ and Γ as the essence of inertial pumping and in using observations to show those physics at work under a TC of extreme intensity (Fig. 1.2c).

Past studies have inferred the 3D structure of upper ocean features powered by TCs (Price et al., 1994; Jacob et al., 2000; Sanabia and Jayne, 2020). Here, the (ζ,Γ) framework presented in Section 3 helped us to unambiguously relate observed isothermal displacements to TC forcing (Figs. 1.8, 1.9). Equations (1.9)-(1.11) can relate storm morphology (represented by $\nabla\times\tau$ and $\nabla\cdot\tau$) to patterns in NIW generation in a 1D framework. While our results validate equations (1.9)-(1.11) in reproducing upwelling and NIW generation by fast-moving TCs, future studies may test it for slow-moving TCs and storms with different morphologies. General nonlinear dynamical models based on ζ and Γ (see for example Névir and Sommer 2009) may facilitate such studies by clarifying the roles of pressure gradients and nonlinear terms.

1.5.2 Float-based estimates of ζ and Γ

Float estimates of ζ and Γ for $x > 500$ km in TC-following coordinates do not capture $\Gamma < 0$ necessary for downwelling evidenced by T^* (Figs. 1.8c, 1.9). This is likely due to the loss of coherence by NIWs in the TC wake, since derivatives $\frac{\partial u^*}{\partial y}$ and $\frac{\partial v^*}{\partial y}$ are set by differences

in measurements made more than 200 km and 12 hours apart (Figs. 1.1, 1.2). Such biases in $(\zeta^*_{surf}, \Gamma^*_{surf})/f$ affect the value $r = 0.5f$ used for numerical solutions in Fig. 1.8, which is considerably higher than values $\sim 0.2f$ commonly used to reproduce $\bar{\mathbf{u}}$ under extratropical storms (Pollard and Millard, 1970; D'Asaro, 1985; Alford, 2001). Past studies have argued that r is likely greater in TC wakes due to increased NIW energy flux divergence caused by the point-like nature of TC forcing (Kundu and Thomson, 1985) and interactions with background motions (Guan et al., 2014). However, aforementioned uncertainties in our estimates $(\zeta_{surf}, \Gamma_{surf})$ complicate interpretations of the significance of the value $r = 0.5f$ used here and its relation to NIW dynamics. A detailed analysis of NIW properties using this dataset over longer timescales and without the assumptions implied by our coordinate transformation can be found in Johnston et al. (2021).

1.5.3 Float-based descriptions of mixing

Vertical profiles of T and S (Figs. 1.11, 1.14) detail mixing processes that modulate storm development. Thorpe scale estimates of κ and ε (Figs. 1.9, 1.10) provide the spatial distribution of mixing and potential impacts to air-sea interactions. While turbulent heat fluxes have been calculated directly using Lagrangian instruments (D'Asaro, 2003), the indirect approach followed here allows near real-time monitoring with potential applications in forecasting. Moreover, the watermass transformation analysis in Fig. 1.15 and inferred turbulent mean heat fluxes $J_q \approx 1900 \pm 1000$ W m^{-2} across the 26 °C isotherm in the TC wake show that subsurface redistribution of heat by mixing may persist after SST stabilizes. This emphasizes the importance of in-situ turbulence estimates in studies aiming to improve parameterizations used in studies of TC-climate interaction (Sriver and Huber, 2007; Korty et al., 2008; Brizuela et al., 2023a).

Insufficient spatial resolution in numerical models can cause them to underestimate the intensity of TC winds (Walsh et al., 2007), subsequent upwelling, and NIW generation (Vincent et al., 2012a). Likewise, it is unclear whether mixing parameterizations used by models can reproduce the full set of impacts reported here and others that may remain undetected. For

example, accurate representation of mixing in rain layers (Fig. 1.14) and barrier layers (Balaguru et al., 2012; Rudzin et al., 2019) is challenging but necessary to avoid biases in forecasts of storm intensity (Hlywiak and Nolan, 2019). These and other intricacies associated with TC-driven mixing and NIW generation, including their long-term impacts on ocean thermodynamics, have yet to be comprehensively described in observations. Analyses presented in Sections 4 and 5 show how data from autonomous platforms can provide insight about the multiscale ocean response to TCs. Such profiling float measurements are crucial to accurately constrain the role of TCs in global budgets of mixing and internal wave energy.

1.6 Conclusions

Formulating the linear ML dynamics using ζ and Γ in equations (1.9)-(1.11) yields a direct statement of inertial pumping and explains NIW generation behind TCs. This gradient-based view shows that the clockwise rotation of currents rearranges (u, v) so that ζ evolves into Γ, and Γ into $-\zeta$ (Fig. 1.4). In these cycles, ζ and Γ remain in quadrature as are u and v for NIWs. ML currents in observations and a 3D model of Mangkhut followed this pattern, which also controlled w in the TC wake (Figs. 1.6, 1.8).

Our analyses include indirect estimates of ocean mixing and its effects. Progressive changes in profiles of T and S indicate that SST cooling beneath Mangkhut was dominated by turbulent entrainment into the ML (Fig. 1.11, 1.13). Thorpe scale estimates in regions of unstable stratification show active mixing ahead, under, and behind Mangkhut but was most vigorous near the TC eye (Fig. 1.10c), where we estimate $\kappa \sim 10^{-1}$ m^2 s^{-1}. Such values of κ would produce to heat fluxes of $\sim 4 \times 10^3$ W m^{-2} across the ML base (Figs. 1.9) and can explain the observed SST cooling rate ~ 0.1 °C hr^{-1} (Fig. 1.11a). Likewise, the corresponding salinity flux $\kappa \frac{\partial S}{\partial z} \sim 2 \times 10^{-3}$ psu m s^{-1} explains an increase of ~ 0.1 psu hr^{-1} in SSS, roughly the same as the greatest rates in our observations (Fig. 1.12a). Furthermore, our measurements highlight the effects of near-surface rain layers (Fig. 1.14), whose diffusion into the ML was estimated

to use $\sim 10\%$ of potential energy change associated with mixing near the TC track. Lastly, we document the continued transformation of watermass characteristics hundreds of kilometers behind the TC with diffusivities $\kappa > 10^{-3}$ m^2 s^{-1} down to ~ 110 m depth (Fig. 1.15).

This work is supported by grant NA17OAR4310259 from the Climate Variability and Predictability program at NOAA, and grants N00014163085 and N000141613073 from the Office of Naval Research's PISTON initiative, which are components of the international Years of the Maritime Continent program. We are grateful to the master, crew, and science party on *R/V Thomas Thompson* for their help in deploying floats. The Instrument Development Group at the Scripps Institution of Oceanography designed, prepared, and monitored the SOLO-II floats. N.G.B. is funded by Consejo Nacional de Ciencia y Tecnología (CONACyT) and UC Mexus. E.J.T. contributes effort with funding from the NOAA Weather Program Office's Precipitation Prediction Grand Challenge. Without implying their endorsement, we thank Kristin Zeiden, Nathalie Zilberman, and William R. Young for their valuable comments.

Chapter 1, in full, is a reprint of the material as it appears in G. Brizuela, Noel; Johnston, T. M. Shaun; Alford, Matthew H.; Asselin, Olivier; Rudnick, Daniel L.; Moum, James N.; Thompson, Elizabeth J.; Wang, Shuguang & Lee, Chia-Ying (2023). A vorticity-divergence view of internal wave generation by a fast-moving tropical cyclone: insights from Super Typhoon Mangkhut. *Journal of Geophysical Research: Oceans*. The dissertation author was the primary investigator and author of this paper.

Chapter 2

Prolonged thermocline warming by near-inertial internal waves in the wakes of tropical cyclones

2.1 Introduction

Ocean turbulence regulates the ocean's internal stratification, circulation patterns, and poleward heat transport (Ganachaud and Wunsch, 2000; MacKinnon et al., 2017; Holmes et al., 2019). Furthermore, modeling studies increasingly connect high-frequency weather disturbances to enhanced turbulent mixing that sustains the background air-sea thermal balance (Qiu et al., 2004; Jochum et al., 2013; Zhang et al., 2015; Luongo et al., 2023). Directly beneath the powerful winds of tropical cyclones (TCs), shear-driven turbulence entrains cold thermocline waters into the near-surface mixed layer (ML), thereby leaving cold ML wakes atop anomalously warm thermoclines (Price, 1981; Mrvaljevic et al., 2013; Zhang et al., 2018; Johnston et al., 2020). In the weeks following TC passage cold sea surface temperatures (SSTs) help enhance local ocean heat uptake (OHU), causing the upper ocean to warm up and restratify back towards its climatological state (Price et al., 2008; Haney et al., 2012; Pasquero et al., 2021). At the end of this process, subsurface warm anomalies that were mixed down during TC passage are effectively insulated from atmospheric influence and thus amount to a net increase in ocean heat content (OHC) (Emanuel, 2001; Sriver and Huber, 2007; Mei et al., 2013; Cheng et al., 2015).

After being advected along isopycnals by large scale currents, anomalies in OHC induced by TCs can reach the surface, release their heat into the atmosphere, and influence climate at remote locations (Korty et al., 2008; Sriver et al., 2010; Fedorov et al., 2010).

Remote sensing estimates of the TC contribution to global OHU (total time rate of change in OHC) range roughly between 0.15 and 0.60 PW (see Bueti et al. (Bueti et al., 2014) for an overview of major studies and methods). Whether that heat stays in the ocean for months or years, however, is a matter of debate. Assuming that warm anomalies induced by TCs stay fixed where they first appeared, Jansen et al. (Jansen et al., 2010) estimated that as much as $\sim$70% of heat mixed down by TCs would be released locally to the atmosphere when the ML deepens during winter. However, rates of steric expansion inferred from sea surface height data in TC wakes suggest that anomalies in OHC induced by TCs mostly persist through the winter (Mei et al., 2013). Up to this point, it remains unclear which mechanisms are helping transfer warm anomalies below the winter ML and thus preserving TC-induced contributions to OHC.

Prolonged influence of TCs on values of thermocline turbulent diffusivity (κ) and resulting downward heat fluxes (J_q) would allow subsurface warm anomalies to deepen weeks after TC passage and thus keep them away from the winter ML. Near-inertial internal waves (NIWs), which are generated by fast-moving TCs (Geisler, 1970; Brizuela et al., 2023b) and enhance thermocline mixing (Gregg et al., 1986; Hebert and Moum, 1994; Alford and Gregg, 2001; Hummels et al., 2020), may well have such an effect. Cuypers et al. (Cuypers et al., 2013) used moored data of velocity and stratification after the passage of a tropical storm in the Indian Ocean to infer J_q and associated warming rates (T_t^{turb}, where the subscript t indicates a time rate of change) that result from vertical gradients in J_q (Eq. 2.4). Their analyses, which only cover the upper 100 m, rely on a fine-scale mixing parameterization (Gregg, 1989; MacKinnon and Gregg, 2005) that yields peaks in J_q along NIW shear layers and implies $T_t^{\mathrm{turb}} \approx 0.015\,^{\circ}\mathrm{C\ day}^{-1}$ directly below NIW envelopes (Cuypers et al., 2013). Similarly, other studies have indirectly inferred the presence and effects of thermocline mixing by TC-generated NIWs (Jaimes and Shay, 2010; Zhang et al., 2014), sustained microstructure turbulence measurements are necessary to constrain

the spatial and temporal extent to which TCs enhance κ and J_q and thereby understand the mechanisms responsible for preserving excess heat below the winter ML.

Knowing how, when, and where TCs drive ocean mixing is necessary to fully understand the TC contribution to OHC and subsequent impacts on climate (Korty et al., 2008; Jansen and Ferrari, 2009; Fedorov et al., 2010; Manucharyan et al., 2011). Here, we compare microstructure estimates of κ and J_q before and after the passage of three major TCs. Our analyses confirm that thermocline values of κ and J_q are enhanced by TC-generated NIWs down to at least 300 m depth and up to three weeks after TC passage (the entire vertical and temporal span of our observations). Such prolonged mixing transfers heat between the seasonal and permanent thermoclines, thus deepening the reach of TC-induced warm anomalies and presumably extending their residence time in the ocean. Near-surface data also include increased J_q after TC passage, implying greater rates of heat uptake at the ocean surface. Lastly, we derive an empirical linear relation between thermocline NIW activity and κ and use it to infer the regional significance of thermocline warming by NIW-driven mixing in TC wakes. Overall, our analyses show that thermocline mixing by TC-generated NIWs must be represented in models to accurately assess the effects of TCs on OHC, the upper ocean circulation, and remote impacts to climate.

2.2 Results and Discussion

Shipboard measurements of subsurface ocean conditions before and after TC forcing in the Western Pacific Warm Pool were made onboard *R/V Thomas G. Thompson* between 20 August and 11 October of 2018. The first half of our experiment was characterized by suppressed atmospheric convection (Sobel et al., 2021), but TCs Mangkhut, Trami, and Kong-Rey moved by our study region during the second half (Figs. 2.1a,b, S1). The cumulative transfer of kinetic energy from winds into the ocean (ΔKE, see Materials and Methods) calculated for two 30-day periods (Figs. 2.1a,b) is reflected by vertical profiles of observed kinetic energy ($KE = \rho_0/2\|\mathbf{u}\|^2$, Fig. 2.1c) before and after TC passage. Ocean areas sampled before TC passage saw no gain in

kinetic energy from winds (areas where $\Delta KE < 0$ in Fig. 2.1a), but regions sampled after TC passage gained $\Delta KE > 2 \times 10^5$ J m^{-2} (Fig. 2.1b). Only a fraction of ΔKE contributes to NIW generation, but rather than resolve the complicated dynamics that determine this energy transfer (Crawford and Large, 1996; Alford, 2020) we point out that the translation speed of the three TCs was greater than the baroclinic mode-1 gravity wave speed over our study region (Fig. S1). This implies that ocean currents in their wakes were dominated by NIWs (Geisler, 1970; Nilsson, 1995) and thus make it easy to identify the TCs' influence on upper ocean dynamics.

By comparing measurements made before and after the passage of TCs, we assess the ocean effects of TC forcing on timescales of days to weeks. To sort out spatial and temporal differences in the ocean response to TCs, our observations were grouped into one period representing conditions before TC passage (cyan lines), and three depicting post-TC dynamics. The first set of post-TC measurements was located 250 km to the left of Mangkhut's track (*Left side*, orange lines in Fig. 2.1), implying that NIWs observed there had most likely propagated south from regions where ΔKE peaked (Chang and Anthes, 1978; Price, 1981). In contrast, the two later periods of post-TC observations represent ocean conditions *Across tracks* (purple lines) and on the *Right side* of TC tracks (pink lines), thus including areas of greater ΔKE, ML deepening, and local NIW generation (Crawford and Large, 1996; Alford, 2020). Ship tracks for each period are color coded in Figs. 2.1a,b, while the corresponding temporal coverages are compared to the timing of TC forcing in Fig. S1. Time-depth sections of measured horizontal velocities ($\mathbf{u} = (u, v)$), their near-inertial component ($\|\mathbf{u}_{\mathrm{NI}}\|$), κ, and the resulting J_{q} (Fig. 2.2) for each period reveal a clear contrast in NIW activity and mixing before and after TC passage.

TCs Mangkhut, Trami, and Kong-Rey moved across 135 °E on 12 September, 23 September, and 1 October respectively (Figs. S1, 2.3c). Post-TC observations span the period between 21 September and 12 October, meaning that NIWs in our observations had time to disperse from each other, propagate away from their generation sites, and undergo refraction (Kunze, 1985; Thomas et al., 2020; Asselin and Young, 2020). Because NIWs can persist at a given site for $\sim$ 25 days (Alford et al., 2017), the effects of the three TCs are likely superimposed

in parts of our record. Therefore, our measurements are representative of the Tropical Western Pacific at the height of the TC season rather than of the ocean's long-term response to a single TC.

2.2.1 Upper ocean conditions before and after TC forcing

Upper ocean conditions after the passage of TCs are characterized by elevated mean values of KE, κ, J_q, and shear variance (Figs. 2.1c-f) compared to ocean conditions before TCs (cyan lines). 95% confidence intervals for the time-depth means of κ and J_q in Table 2.1 are shown separately for the near-surface (0-50 m depth, white rows) and thermocline levels (50-250 m, turquoise rows), revealing that J_q increased after TC passage by factors in the ranges [1.8, 21.4] and [1.7, 4.8] at the near-surface and thermocline levels. Low values of J_q between 50 and 70 m for all periods in Fig. 2.1e indicate that turbulent heat transfer in the near-surface was relatively independent from transfer within the thermocline. In other words, there are two separate mixing processes happening above and below the ML base days to weeks after TC passage, and near-surface restratification is helping insulate thermocline heat, a necessary condition for net OHC to increase after TC passage (Emanuel, 2001).

Vertical profiles of J_q in Fig. 2.1e are consistent with increased OHU in the TC wake, while thermocline data further point to enhanced heat transfer across 150 m depth or between the seasonal and permanent thermoclines. The mean heat flux convergence and resulting warming rates T_t^{turb} are ~ 0.03 °C day^{-1} in the upper 50 m, while thermocline measurements reveal contiguous layers with warming/cooling rates reaching ± 0.015 °C day^{-1} (Fig. 2.1g, see Materials and Methods). These values contrast with observations made before TC passage, when maximum values of T_t^{turb} were roughly 25% of those measured after TC forcing (Fig. 2.1g). Overall, this evidence points to increased local OHU after TC forcing and prolonged deepening of upper thermocline heat, which would presumably reduce the amount of heat that will be locally lost to the atmosphere during winter.

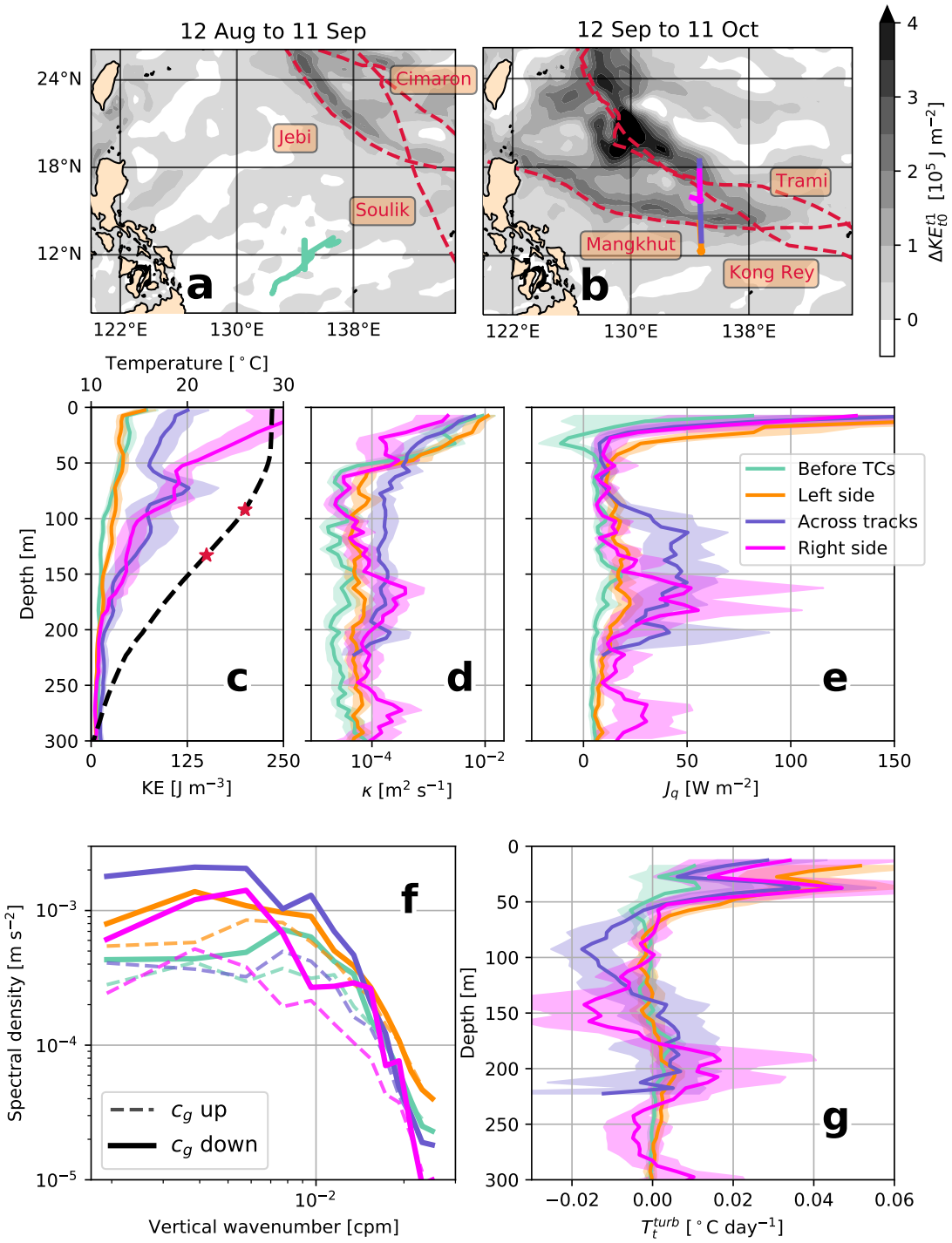

Figure 2.1. Ocean effects of wind forcing by TCs. (a,b) ΔKE integrated over the periods noted in 2018. Mean vertical profiles and 95% confidence intervals of (c) KE, (d) κ, (e) J_q, and (g) T_t^{turb} for each of the four periods defined in Fig. 2.2. (c) shows the mean $T(z)$ across all periods (dashed black line, upper axis), while red stars mark the 22 and 26 °C isotherms. Measurements in (f) vertical wavenumber spectra of shear are shown in dashed and solid lines for rotation associated with upward- and downward-propagating internal wave energy respectively.

Table 2.1. Statistical summary of four periods of observation. Based on a total of N individual casts, 95% confidence intervals for the average κ and J_q were computed for the near-surface (depth < 50 m, white rows) and thermocline (50 - 250 m depth, green rows) layers during each of the periods defined in Fig. 2.2. Vertical variations in κ and J_q are plotted with confidence intervals in Figs. 2.1d,e.

	N	$\langle\kappa\rangle$ [10^{-5} m^2 s^{-1}]	J_q
Before TCs	1273	[125 - 241]	[3 - 13]
		[3 - 3]	[7 - 8]
Left side	1635	[243 - 337]	[40 - 56]
		[6 - 7]	[14 - 15]
Across tracks	841	[133 - 201]	[26 - 44]
		[16 - 20]	[30 - 35]
Right side	306	[45 - 94]	[25 - 56]
		[9 - 12]	[18 - 23]

2.2.2 Observed collocation of NIWs, κ, and J_q

Time-depth sections of $\mathbf{u}$, $\mathbf{u}_{NI}$, κ, and J_q in Fig. 2.2 indicate that the observed increase in thermocline values of κ and J_q was associated with TC-generated NIWs. $\|\mathbf{u}_{NI}\|$ rarely reached 0.15 m s^{-1} before TC passage (Figs. 2.2e,i), but downward-propagating envelopes where $\|\mathbf{u}_{NI}\| > 0.15$ m s^{-1} are evident in all post-TC measurements. More importantly, NIW envelopes are collocated with areas of enhanced κ and J_q (Figs. 2.2f-h,j-l). This collocation continues down to 300 m, as deep as our microstructure measurements go, but is likely to continue at greater depths as NIWs propagate into the deep ocean.

Changes in rotary wavenumber spectra of shear (Fig. 2.1f, see Materials and Methods) before and after TC passage show a significant increase in variance associated with TC-generated internal waves. Shear associated with downward-propagating internal wave modes (c_g down, Fig. 2.1f) increased after TC passage and at virtually all scales, while upward-propagating internal wave modes (c_g up, Fig. 2.1f) did not consistently increase their shear variance. Evidence of increased shear due to downward-propagating NIWs may explain the collocation between mixing and NIWs in Figs. 2.2f-h,j-l, as shear instability is known to be the leading driver of mixing within NIW envelopes (Gregg et al., 1986; Hebert and Moum, 1994; Alford and Gregg, 2001).

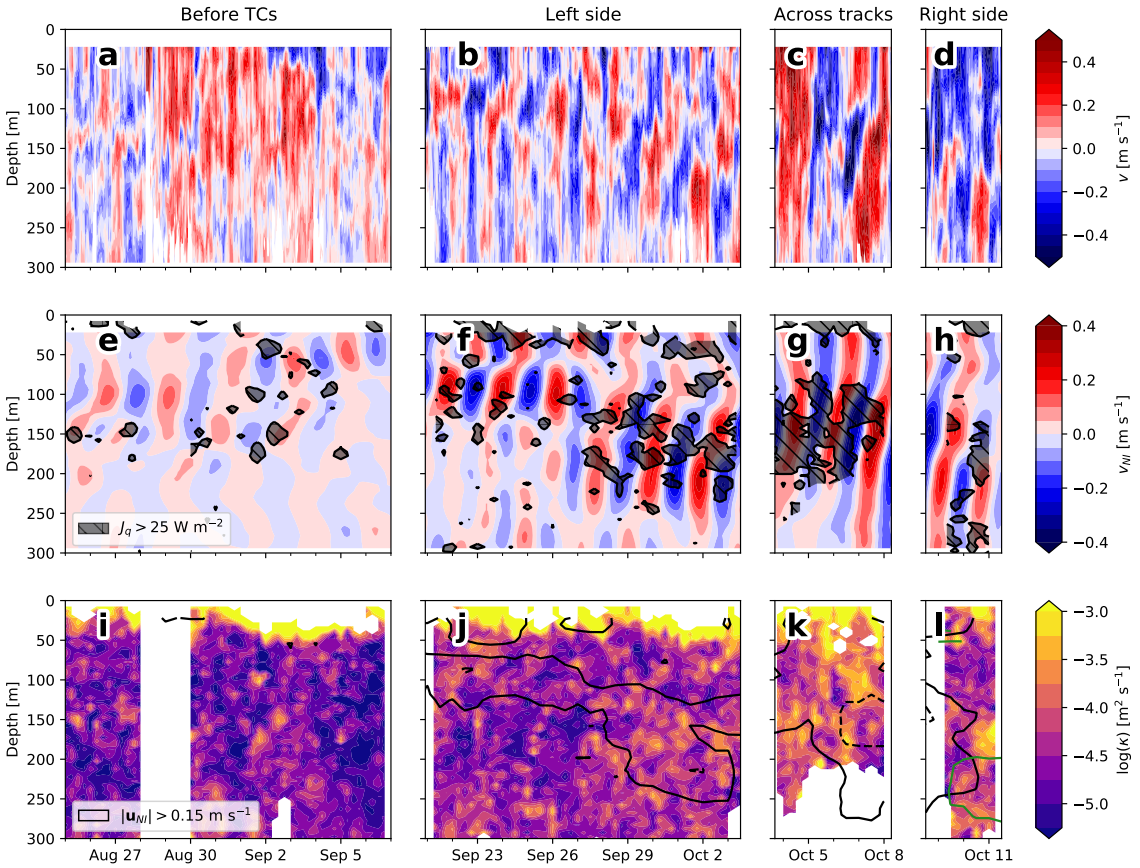

Figure 2.2. Upper ocean conditions before and after the passage of three major TCs. Color shading shows (a-d) observed velocities v, their (e-h) bandpass-filtered component v_{NI}, and associated (i-l) 12-hourly averages of κ. Gray hatching in (e-h) outlines areas where 8-hourly averages of J_{q} are greater than 25 W m^{-2}. Black contours in (i-l) outline areas where $\|\mathbf{u}_{\mathrm{NI}}\|$ is greater than (solid) 0.15 and (dashed) 0.3 m s^{-1}. Each column represents one of the periods whose temporal averages are shown in Fig. 2.1.

A meridional transect across the wakes of TCs Mangkhut, Trami, and Kong-Rey (Fig. 2.3 spans the *Across TC tracks* period) reveals complex variations in NIW properties and mixing that result from patterns in NIW generation and propagation since TC passage. Tilted bands of alternating signs in v and v_{NI} (Figs. 2.3a, 2.2g) are more intense and dominated by greater vertical scales at the northern end of the transect, which features more recent TC forcing than the southern end. Three distinct maxima in near-surface $\|\mathbf{u}\|$ are located near 13.8, 15.8, and 17.8°N (Fig. 2.3b) and likely associated with the passage of TCs Mangkhut, Kong-Rey, and Trami, which crossed 134.7°E near 14.1, 16.5, and 17.1°N roughly 23, 5, and 14 days before we sampled their respective latitudes (Figs. 2.3c). Thermocline $\|\mathbf{u}\|$ was as high as 1.1 m s^{-1} directly below mesoscale layers where shear squared ($S^2 = \|\frac{\partial \mathbf{u}}{\partial z}\|^2$) peaks and thus creates a favorable environment for enhanced turbulence (Figs. 2.3c,d).

Elevated mean values of thermocline J_{q} after TC passage (Fig. 2.1e, Table 2.1) were largely set by relatively few intermittent events with $J_{\mathrm{q}} > 100\,\mathrm{W\ m^{-2}}$ that happened near local peaks in S^2 (Fig. 2.3c). We assess the impact of S^2 on J_{q} by calculating the Richardson number $Ri = N^2/S^2$ and outlining areas where $Ri < 0.5$ (gray contours in Fig. 2.3d). Here, N is the buoyancy frequency and while the canonical threshold for shear instability is $Ri < 0.25$, we use a higher value to compensate for the vertical resolution of $\mathbf{u}$. Notice that the background value of J_{q} is negligibly small, but sporadic patches of increased J_{q} are collocated with gray contours in Fig. 2.3d. This collocation is evidence that enhanced mixing resulted from shear instability in NIWs.

2.2.3 Regional variations in NIW activity and mixing

To generalize our time- and location-specific measurements, we assume that empirical relations between observed $\|\mathbf{u}_{\mathrm{NI}}\|$ and κ (Figs. 2.4a,b) are representative of those in other areas impacted by the same TCs. This way, we use HYCOM's representation of thermocline $\|\mathbf{u}_{\mathrm{NI}}\|$ (see Supplementary Material) to inform the distribution of NIW activity throughout the Western Pacific and infer associated patterns in κ and thermocline mixing (Figs. 2.4c,d). Even though

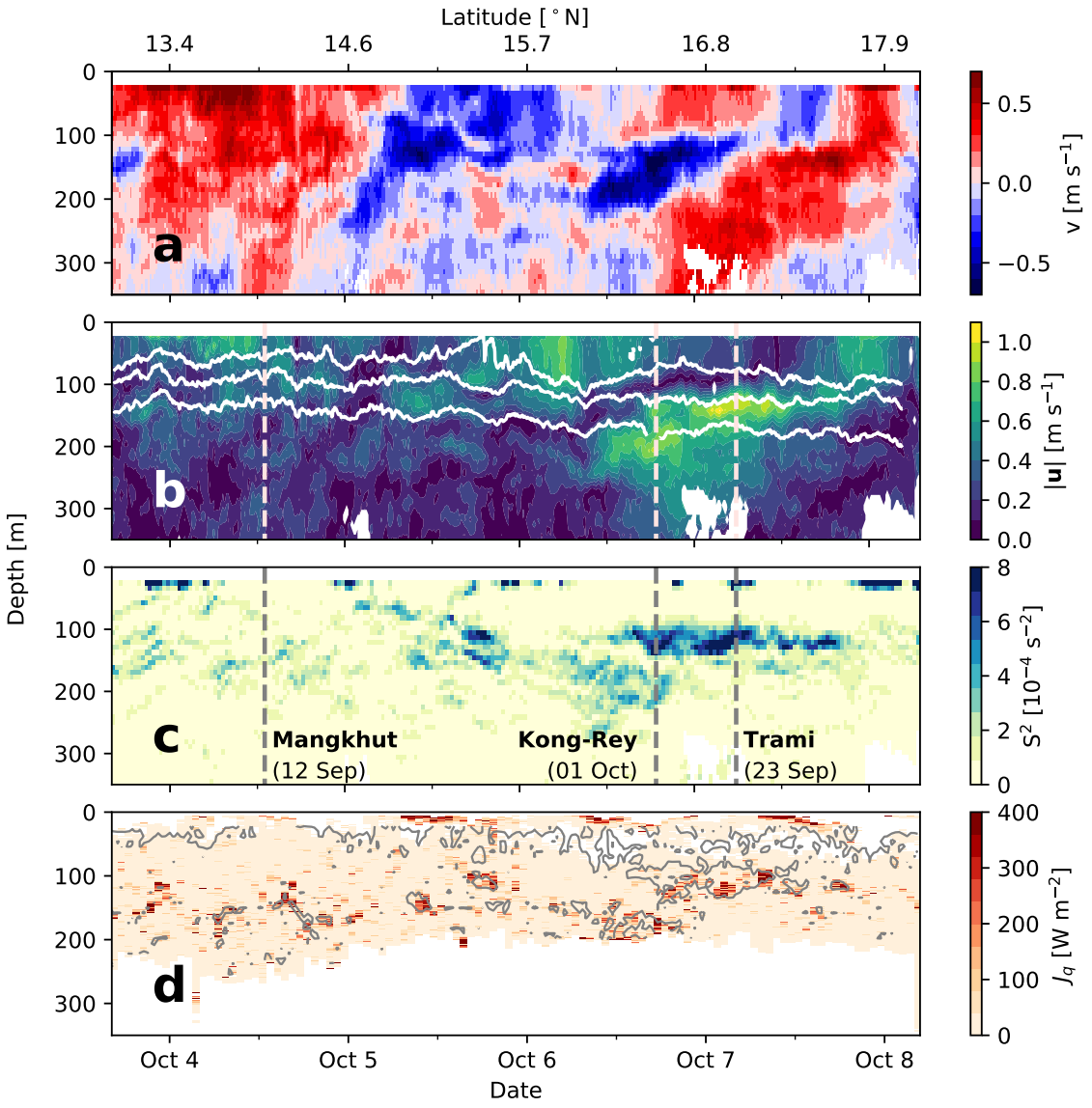

Figure 2.3. NIW activity, shear, and turbulence across TC tracks. Shipboard data show (a) v, (b) $\|\mathbf{u}\|$, (c) S^2, and (d) J_q in color. White contours in (b) track the 22, 26, and 28 °C isotherms, while gray contours in (d) show areas where $Ri = N^2/S^2 < 0.5$. Vertical dashed lines Figs. 2.3b,c indicate the approximate latitudes and dates (text in parenthesis) at which TC tracks crossed 134.7°E.

$\|\mathbf{u}_{\mathrm{NI}}\|$ is only an indirect proxy for turbulence and NIWs drive enhanced mixing through their effect on S^2 and Ri (Figs. 2.3c,d), extending the observed relation between $\|\mathbf{u}_{\mathrm{NI}}\|$ and κ helps us to broadly assess the impacts of TC-generated NIWs on the regional ocean heat budget.

Observed 4-day averages of thermocline κ and $\|\mathbf{u}_{\mathrm{NI}}\|$ covaried during our experiment (Fig. 2.4a). In fact, the linear relation

$$\kappa = a\|\mathbf{u}_{\mathrm{NI}}\| + b \tag{2.1}$$

yields a correlation coefficient $r = 0.64$ when $a = 33 \pm 5 \times 10^{-5}$ and $b = 0.9 \pm 0.9 \times 10^{-5}$ (Fig. 2.4b, 95% confidence interval). A comparison between HYCOM's representation of NIW activity ($\|\mathbf{u}_{\mathrm{NI}}^{\mathrm{HYCOM}}\|$) and two year-long moored records from our study region shows that HYCOM can roughly reproduce temporal patterns in $\|\mathbf{u}_{\mathrm{NI}}\|$ but can underestimate its value below 100 m (Figs. S2, S3). After noting this, we used $\|\mathbf{u}_{\mathrm{NI}}^{\mathrm{HYCOM}}\|$ and the linear relation in Fig. 2.4a to estimate κ and J_{q} during our experiment in the Western Pacific (Fig. 2.4c,d).

To emphasize the long timescales of NIW-driven mixing, HYCOM-based estimates of κ and J_{q} are shown in Figs. 2.4c,d as 30-day averages between 12 September and 11 October (the same period used for ΔKE in Fig. 2.1b). To facilitate interpretation of their climate significance, κ and J_{q} were interpolated onto the 22 and 26 °C isotherms. Results for the 22°C isotherm are shown in Figs. 2.4c,d, while results at the 26°C level are shown in Fig. S4a,b and a time series of the T_t^{turb} that results from differences between the two levels is shown in Fig. S4c. The 22 °C isotherm was chosen because it roughly separates between hotter water masses that take up heat from the atmosphere and colder ones that release their heat into the atmosphere (Holmes et al., 2019). Similarly, the 26 °C isotherm was chosen because it approximately marks an SST threshold at which air-sea fluxes can power TC intensification (Leipper and Volgenau, 1972; Shay et al., 2000).

Regional estimates of thermocline κ have local peaks along the right sides of TC tracks (dashed lines in Fig. 2.4d), consistent with the asymmetry of NIW generation by TCs (Chang and

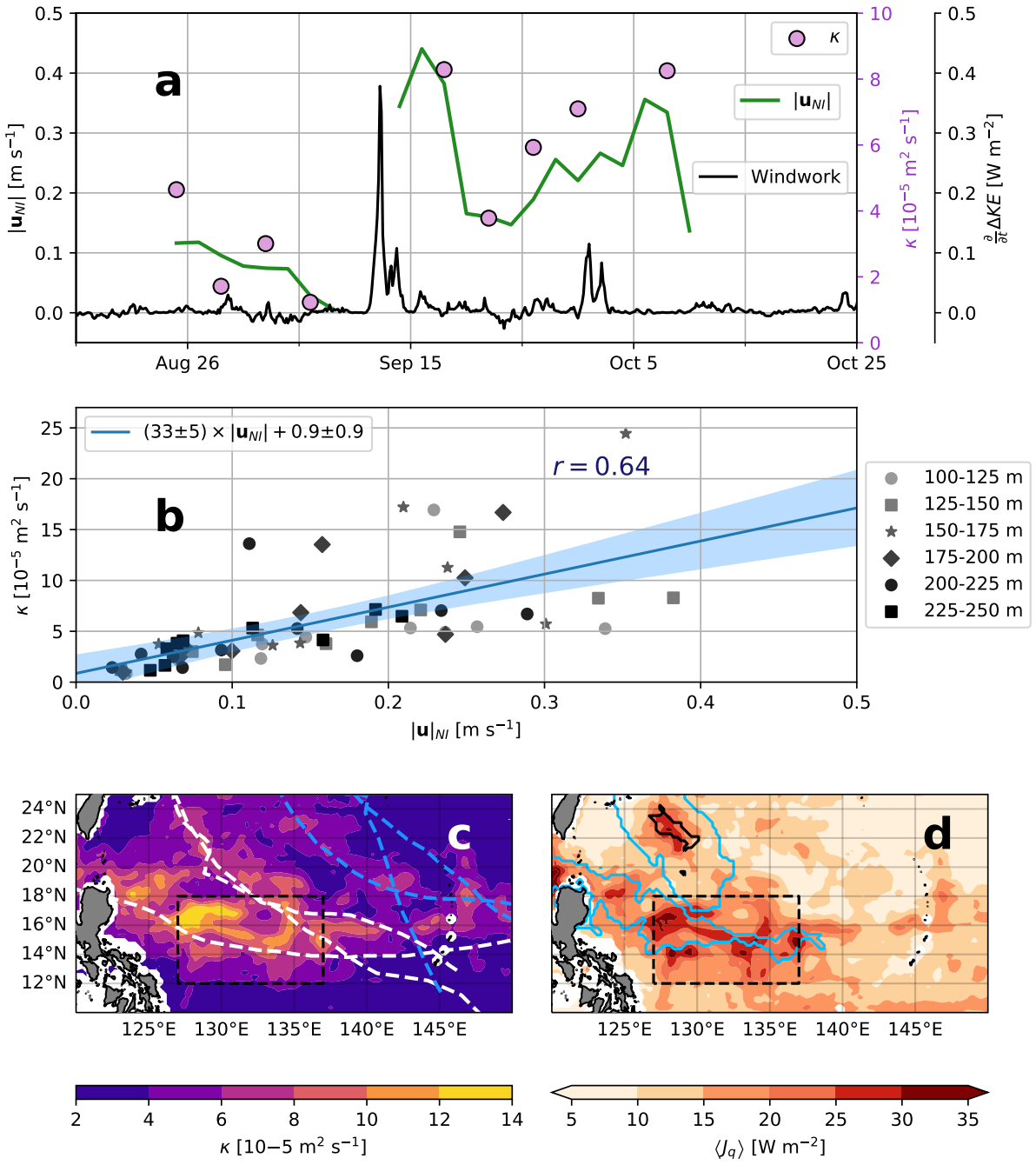

Figure 2.4. NIW activity, its relation to κ, and regional effects. (a) 4-day averages of $\|\mathbf{u}_{\mathrm{NI}}\|$ (green line) and κ (pink circles) observed between 125 and 150 m. Windwork $\frac{\partial}{\partial t}\Delta KE$ at the mooring site is shown in black. (b) Linear fit on 4-day averages of observed $\|\mathbf{u}_{\mathrm{NI}}\|$ and κ at different depths ($r = 0.64$). Mean values of (c) κ and (d) J_{q} at the 22 °C isotherm between Sep 12 and Oct 11 inferred from $\|\mathbf{u}_{\mathrm{NI}}^{\mathrm{HYCOM}}\|$. Dashed lines in blue and white show TC tracks as in Fig. 2.1a,b. The blue contour in (d) shows areas of SST cooling > 1 °C induced by TCs, while the black contour denotes an area where z_L was deeper than the 22 °C isotherm. Dashed box is area whose averages are described in the main text.

Anthes, 1978). While the influence of TCs Mangkhut, Trami, and Kong-Rey is most prominent, κ is also 2-3 times greater than the background along the track of TC Jebi (blue dashed line), which passed by this area near 1 September. Similar patterns are observed in J_q, which is as high as 35 W m^{-2}. These values are roughly consistent with observations, where mean values of J_q at the 22°C isotherm are approximately 20, 40, and 20 W m^{-2} for the *Left Side, Across TC Tracks*, and *Right Side* periods respectively (Fig. 2.1e).

To assess the climatic relevance of our results, we focus on values of J_q inside the 10° × 6° dashed box in Fig. 2.4d. There, the area-averaged NIW-driven J_q across the 22 °C isotherm was 20.5 ± 3.0 W m^{-2}, which is roughly 5% greater than across the 26 °C isotherm (Fig. S4a,b) and ∼80% of the climatological surface heat flux for September (≈ 25 W m^{-2}). The difference between J_q at 22 and 26°C, which is small compared to the magnitude of J_q, would presumably cool the water between these isotherms at a rate ≈ 0.01 °C month^{-1} (Fig. S4c, Eq. 2.4), while the remaining J_q remains available to warm the ocean below 22°C.

Integrated within the dashed box in Fig. 2.4d, NIW-driven J_q transfers ∼ 0.015 PW across the 22°C isotherm, which is between 2.5 and 10% of the global TC contribution to OHU (Sriver and Huber, 2007; Mei et al., 2013; Cheng et al., 2015). Furthermore, this downward heat flux is ∼2% of the northward Pacific heat transport out of the tropics (Talley, 2003; Forget and Ferreira, 2019) and ∼16% of the contribution by eddies (Roemmich and Gilson, 2001). Considering that these estimates only account for a small fraction of the area impacted by the three TCs in this study, our analyses highlight the importance of NIWs in shaping the TC contribution to OHC and climate.

2.2.4 SST cooling and TC-driven mixing

Previous estimates of the TC contribution to OHC have used satellite measurements of SST cooling behind TCs to infer the TC-induced κ via a characteristic mixing depth z_L. This method, exemplified in Fig. 2.5a, often defines z_L as the depth above which the average pre-TC temperature is equal to the SST after TC passage (T_{TC}). Assuming a mixing timescale $t_{mix} \sim 24$ h

to represent the duration of the forced stage, turbulence is then roughly quantified as $\kappa \approx z_L^2/t_{\mathrm{mix}}$ (Sriver and Huber, 2007; Sriver et al., 2008, 2010). While this approach is physically sound and has proven useful to parameterize TC-driven mixing, it gives the impression that TC-driven mixing only acts to impact SST via ML deepening and that it only does it during the forced stage of TCs. However, observations in Figs. 2.1e and 2.2e-h show that turbulence in TC-generated NIWs drives a prolonged downward transfer of heat across the thermocline (Fig. 2.5b). If the contribution of TCs to ocean heat transport and remote climate is in fact determined by the amount of heat they transfer to water masses colder than the local wintertime SST (Jansen et al., 2010), quantifying J_q in the thermocline weeks to months after TC passage is essential to assessing the net impact of TCs on OHC and climate (Fig. 2.5).

Spatial patterns in SST cooling and z_L are not indicative of the distribution of NIW activity and thermocline mixing. Blue contours in Fig. 2.4d outline areas where SST cooling in TC wakes exceeded 1 °C, while black contours indicate areas where z_L reached below the 22 °C isotherm (see Materials and Methods). Differences between these contours and our estimates of J_q (Fig. 2.4d) show that SST-based techniques would indicate that no heat was transferred across the 22 °C along the track of TC Mangkhut. The comparison yields similar results at the 26 °C level (Fig. S4b), highlighting how SST cooling and the prolonged NIW-driven mixing detailed by our observations are complementary but quite different facets of TC-driven mixing.

A schematic in Fig. 2.5 summarizes the different stages of mixing driven by TCs and their distinct impacts to upper ocean stratification. SST cooling results from mixing at the ML base during the forced stage of TCs (Fig. 2.5a) and tends to be collocated with ΔKE (Price, 1981). In contrast, the 3D distribution of NIWs is impacted by TC forcing, background stratification, and ocean currents with horizontal scales $\sim$ 25 km and greater (Asselin and Young, 2020; Thomas et al., 2020). Without proper representation of NIWs and their mixing, ocean models are likely to underestimate the depth of anomalous OHC induced by TCs (Fig. 2.5b) and thereby misallocate anomalous air-sea fluxes in subsequent seasons and years (Fig. 2.5c). Two year-long comparisons between modelled and observed $\|\mathbf{u}_{\mathrm{NI}}\|$ in Figs. S2, S3 show that

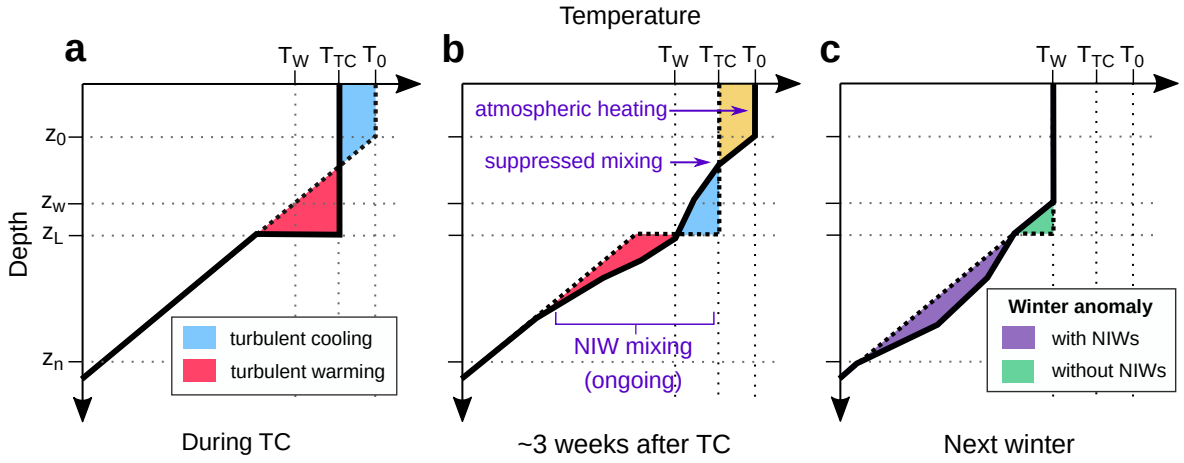

Figure 2.5. Schematic description of short-term and long-term changes in $T(z)$ induced by TC forcing. The solid lines in each panel show (a) ML deepening that happens under TC winds, (b) the partial effect of J_q enhanced by NIWs, and (c) the cumulative effect of NIWs at the end of the TC season. T_0, T_{TC}, and T_w are the pre-TC, post-TC, and wintertime values of SST. Likewise, z_0 is the pre-TC ML depth, z_W is the wintertime ML depth, z_L is the mixing depth inferred from SST, and z_n is the depth below which the NIW-induced J_q is negligible.

HYCOM (horizontal resolution $1/12 \times 1/12°$) underestimates $\|\mathbf{u}_{NI}\|$ with increasing depth, yielding annually-averaged values > 30 % lower than observations below 150 m. This is likely due to the low vertical resolution (50-100 m) of HYCOM's permanent thermocline, suggesting that high resolution model configurations and NIW-specific parameterizations alike (Jochum et al., 2013; Claret et al., 2022) are needed to accurately reproduce the TC contribution to OHC and meridional heat transport.

2.3 Conclusion

Much like mixing at the ML base cools the surface and heats up the seasonal thermocline during the forced stage of TCs (Fig. 2.5a), NIW-driven mixing in the thermocline cools waters directly beneath the ML base and warms the permanent thermocline for weeks after (Figs. 2.1g, 2.5b). Microstructure estimates of J_q demonstrate that NIW-driven mixing can help transfer > 20 W m^{-2} across the 22 °C isotherm for weeks after TC passage (Figs. 2.1e, 2.4d). This prolonged thermocline mixing does not directly impact SST or air-sea fluxes because a minimum in J_q at

the base of the post-TC ML insulates the thermocline from near-surface processes (Figs. 2.1e). Instead, NIW-driven mixing is important to understand the TC impact on ocean stratification because it helps cool the seasonal thermocline and warm the deep ocean (Fig. 2.5b) during fall, when the tropical OHC peaks. Heat transfer across the 22°C isotherm by TC-generated NIWs (Fig. 2.4d) ensures that heat anomalies will be advected towards the midlatitudes or the Equatorial Cold Tongues (Holmes et al., 2019), as opposed to being ventilated locally when the ML deepens during winter (Fig. 2.5c).

Enhanced thermocline κ and J_q weeks after TC passage result from vertical shear in TC-generated NIWs that propagate into the deep ocean (Figs. 2.2e-l, 2.3d). This mechanism is likely to unfold throughout the TC season and over vast regions of the Western Pacific Warm Pool (Fig. 2.4d). Given these scales, mixing by TC-generated NIWs may help explain TC-climate interactions noted in models and observations (Fedorov et al., 2010; Hart, 2011). Inclusion of this previously unrecognized mechanism in climate models constitutes a great technical challenge, as full representation of TC-generated NIWs and their mixing requires high spatial resolution (Walsh et al., 2007; Vincent et al., 2012a), fast air-sea coupling, and specialized parameterizations (Jochum et al., 2013; Claret et al., 2022). Likewise, further microstructure measurements of κ and J_q will be necessary to constrain the fate of warm anomalies deepened by NIW-driven mixing, as this cannot be retrieved from SST, sea surface height, or even in-situ temperature measurements that fail to distinguish turbulent warming from downwelling or horizontal advection.

2.4 Materials and Methods

2.4.1 Shipboard data

Horizontal velocities $\mathbf{u}$ (Figs. 2.2a-d, 2.3b) were measured using a hull-mounted, 75 kHz acoustic Doppler current profiler (ADCP) and were processed using a third order Butterworth filter within the frequency range $[0.7f, 1.3f]$ to extract their near-inertial component $\mathbf{u}_{\mathrm{NI}}$ (Fig. 2.2e-h), where f is the mean inertial frequency for locations sampled. The same filter was

used to compute $\mathbf{u}_{\mathrm{NI}}$ from moored records (Fig. S2) and HYCOM output. Vertical wavenumber spectra of shear (Fig. 2.1f) were computed after applying WKB-stretching and scaling procedures in (Leaman and Sanford, 1975), for which monthly stratification data from ARGO (Roemmich and Gilson, 2009) were used.

Because the ship was only static from 21 Sep to Oct 3 and from Oct 9 to Oct 12, bandpass filters used to calculate $\|\mathbf{u}_{\mathrm{NI}}\|$ when the ship moved across TC wakes are likely to underestimate $\|\mathbf{u}_{\mathrm{NI}}\|$. While ship motion induces a bias in the perceived phase propagation of NIWs (Hebert and Moum, 1994; Alford et al., 2013), small scale spatial variations in $\|\mathbf{u}_{\mathrm{NI}}\|$ can further bias the results of bandpass filtering. Cross-track variations in $\|\mathbf{u}_{\mathrm{NI}}\|$ follow the length scale ~ 100 km, or twice the maximum wind radius of TCs (Geisler, 1970; Brizuela et al., 2023b), but our ship moved at a cross-track velocity of up to 250 km for every inertial period (Fig. 2.3). Sampling at that speed, a 100 km-long peak in $\|\mathbf{u}_{\mathrm{NI}}\|$ would appear in measurements as an oscillation with frequency $> 2f$. This may be the case for some of the local peaks near 150 m in Fig. 2.3b, where $\|\mathbf{u}\|$ goes from 0.4 to 0.9 m s^{-1} and back to 0.4 m s^{-1} in ~ 150 km, or little more than half an inertial period.

More than 4000 individual vertical profiles of temperature (T), stratification (N^2), and the turbulent dissipation rate (ε) were obtained using the Chameleon microstructure profiler (Moum et al., 1995), which was deployed from the stern of *R/V Thomas G. Thompson*. Following (Osborn, 1980), we used 3-hourly (or longer) averages of ε and N^2, and set $\Gamma = 0.2$ (Moum, 1996; Smyth et al., 2001) to compute κ as

$$\kappa = \Gamma \frac{\varepsilon}{N^2}. \tag{2.2}$$

Likewise, turbulent heat fluxes J_{q} were computed as

$$J_{\mathrm{q}} = \rho_0 c_p \kappa \frac{\partial T}{\partial z}, \tag{2.3}$$

while estimates of the turbulent warming rate T_t^{turb} are given by

$$T_t^{\text{turb}} = \frac{\partial}{\partial z}\left(\kappa \frac{\partial T}{\partial z}\right) = \frac{-1}{\rho_0 c_p}\frac{\partial J_{\text{q}}}{\partial z}. \tag{2.4}$$

Here, $\rho_0 = 1024\,\text{kg m}^{-3}$ is the reference density of seawater and $c_p = 4.1 \times 10^3\,\text{J K}^{-1}$ kg^{-1} is the heat capacity. J_{q} and T'_{turb} were computed using hourly averages of the vertical temperature gradient $\frac{\partial T}{\partial z}$ and κ as shown in Fig. 2.3d, and later averaged to the temporal periods specified in Figs. 2.1, 2.2, 2.4, and Table 2.1. Confidence intervals in Fig. 2.1 and Table 2.1 were computed via bootstrapping.

2.4.2 Reanalysis data

Data from the atmospheric ERA5 (Skamarock et al., 2008) and oceanic HYCOM (Chassignet et al., 2007) reanalyses provide context for shipboard observations and help inform their large scale implications. We computed the cumulative transfer of kinetic energy into the ocean $\Delta KE = \int \tau \cdot \mathbf{u}_{surf}\, dt$ as a proxy for net forcing, assuming that a fraction of ΔKE becomes available for NIW generation (Figs. 2.1a,b). Here, τ and $\mathbf{u}_{surf}$ are given 3-hourly data of wind stress and surface velocities from ERA5 and HYCOM respectively, while the dates t_0 and t_1 used are indicated as titles on top of Figs. 2.1a,b.

$\mathbf{u}_{\text{NI}}^{\text{HYCOM}}$ was obtained by applying a third order Butterworth bandpass filter to the model's velocity output using the local frequency range $[0.7f, 1.3f]$. Values of $\|\mathbf{u}_{\text{NI}}^{\text{HYCOM}}\|$ were computed for multiple vertical levels and later validated by comparing them against corresponding measurements from two year-long moored records within our area of observations (Fig. S2, S3).

30-day averages of κ in Figs. 2.4c, S4a were calculated by interpolating 4-day averages of $\|\mathbf{u}_{\text{NI}}\|$ on to the depth of the 22°C isotherm, applying the linear fit described in Fig. 2.4b to obtain κ, and averaging the results between 12 September and 11 October. Corresponding values of J_{q} (Fig. 2.4d) were calculated as $c_p \rho_0 \kappa \frac{\partial T}{\partial z}$ and averaged within the same period, where $\frac{\partial T}{\partial z}$ is

the local vertical temperature gradient in HYCOM.

2.4.3 TC tracks and induced SST cooling

TC track and intensity data are from the US Navy's Joint Typhoon Warning Center (JTWC) and summarized in Fig. S1. TCs' potential for NIW generation was assessed using the ratio U_{storm}/c_g, where U_{storm} is the TC translation speed and c_g is the local baroclinic mode-1 gravity wave speed (roughly 3.2 m s^{-1}, (Chelton et al., 1998)), which was computed using ARGO climatology data (Roemmich and Gilson, 2009) and assuming constant stratification beneath 2000 m.

SST cooling induced by TCs was computed as the difference between SST averages 3 to 10 days before and 1 to 4 days after TC passage (Vincent et al., 2012a) with daily SST data from ERA5. SST cooling was computed for every location within 200 km of TC tracks and corresponding dates of TC passage were defined as the dates of closest proximity to the TC eye. Results were used to plot the blue contours in Fig. 2.4d), which highlight areas where SST cooling from TCs Mangkhut, Trami, or Kong-Rey was greater than 1 °C. Moreover, the characteristic mixing depth z_L was computed using HYCOM temperature stratification data, and areas where z_L went deeper than the pre-TC 22 °C isotherm are shown as black contours in Figs. 2.4d, S4c.

Acknowledgments

This work was supported by grants N00014163085 and N000141613073 from the Office of Naval Research's PISTON initiative, which is a component of the international Years of the Maritime Continent program. N.G.B. was supported by CONACYT and UC Mexus. The authors are grateful for the hard work of the Captain and crew onboard R/V Thomas G. Thompson and R/V Sally Ride during PISTON fieldwork campaigns in 2018 and 2019. Pavan Vutukur and Kerry Latham supported OSU ocean mixing operations.

2.5 Appendix

2.5.1 Tropical cyclones in our observations

Tropical cyclones leave powerful wakes of NIWs behind them when their translation speed (U_{storm}) is greater than the local baroclinic mode-1 gravity wave speed (c_g, roughly 3.2 m s^{-1} Chelton et al. 1998) (Geisler, 1970; Nilsson, 1995). Therefore, we use TC intensity and the ratio U_{storm}/c_g to verify that NIWs sampled in our experiment could have been generated by TCs Mangkhut, Trami, and Kong-Rey (Fig. 2.6). The tracks of each TC and corresponding windspeed are shown in Figs. 2.6a,b, while U_{storm}/c_g is shown in Fig. 2.6. Blue shading in Figs. 2.6b,c represents periods when the eye of each TC was inside the red rectangle outlined in Fig. 2.6, near our observation sites.

All three TCs reached maximum windspeeds > 70 m s^{-1} (Category 5 in the Saffir-Simpson scale), and crossed our study region at or near their period of maximum intensity (Fig. 2.6b). Within the blue shading of Fig. 2.6c, all estimates indicate U_{storm}/c_g, suggesting that the ocean response to all three TCs was dominated by NIWs. Shipboard measurements are represented by horizontal colored rectangles in Figs. 2.6b,c, which indicate the temporal proximity between TC forcing and in-situ observations.

2.5.2 Assessment of NIW activity in HYCOM

Parameterized estimates of κ in Figs. 4c, 2.9a a rely on HYCOM's appropriate representation of near-inertial currents $\mathbf{u}_{NI}$. To assess this, we compared 4-day averages of $\|\mathbf{u}_{NI}\|$ in HYCOM output to observational estimates from two year-long moored records (Figs. 2.7, 2.8). The moorings, located at latitudes 12.3°N (SIO1) and 15.7°N (SIO3) were deployed along the 134.7°E longitude line between October of 2018 and 2019. Moorings were equipped with a pair of upward- and downward-looking ADCPs that recorded hourly averages of $\mathbf{u}$. Frequency filtering of HYCOM and mooring data was done using a third-order Butterworth bandpass filter for the frequency range [0.7f, 1.3f] corresponding to each location. To alleviate the mismatch

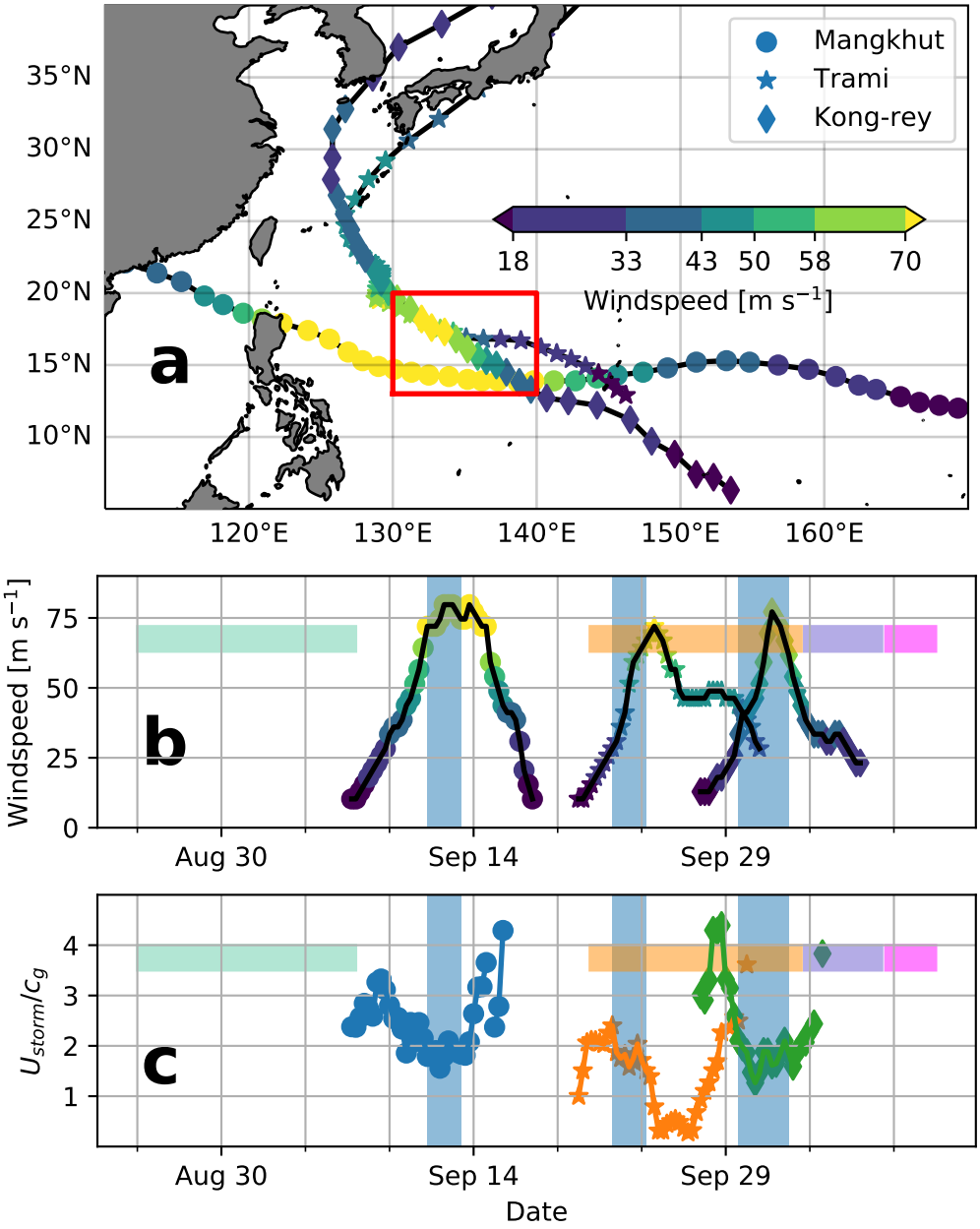

Figure 2.6. Tropical cyclones observed in this study. (**a**) 6-hourly TC tracks and intensity from JTWC data are color coded using the Saffir-Simpson windspeed thresholds. (**b**) Timeseries of maximum one-minute windspeed for the three TCs. (**c**) Ratio U_{storm}/c_g of each TC. Blue highlighting in Figs. 2.6b,c indicate periods when each TC was within the red rectangle in Fig. 2.6a. Colored rectangles in Figs. 2.6b,c mark the observation periods described in the main text.

between observed and modelled values of $\|\mathbf{u}_{NI}\|$ due to inaccuracies in background ocean conditions and surface forcing, we computed $\|u_{NI}\|$ within a region $1^\circ \times 1^\circ$ centered at the mooring locations and plot its range with pink shading in Fig. 2.7.

Statistical comparison between observed and modelled $\|\mathbf{u}_{NI}\|$ suggests that HYCOM accurately reproduces NIW activity in the 51-100 m depth range but underrepresents it at greater depths (Fig. 2.8). While the median values of $\|\mathbf{u}_{NI}\|$ between 51 and 100 m depth in HYCOM are 7 and 16% smaller than in observations at SIO1 and SIO3 respectively, the medians become roughly 60 and 40% smaller than observations between 251 and 300 m. With this in mind, it is apparent that thermocline NIWs in HYCOM are generally underrepresented. Therefore, it is likely that estimates of κ and J_q in Figs. 4c,d are underestimates.

Chapter 2, in full, is a reprint of the material as it appears in Gutiérrez Brizuela, N., Alford, M. H., Xie, S. P., Sprintall, J., Voet, G., Warner, S. J., Hughes, K., & Moum, J. N. (2023). Prolonged thermocline warming by near-inertial internal waves in the wakes of tropical cyclones. *Proceedings of the National Academy of Sciences*, 120(26), e2301664120. The dissertation author was the primary investigator and author of this paper.

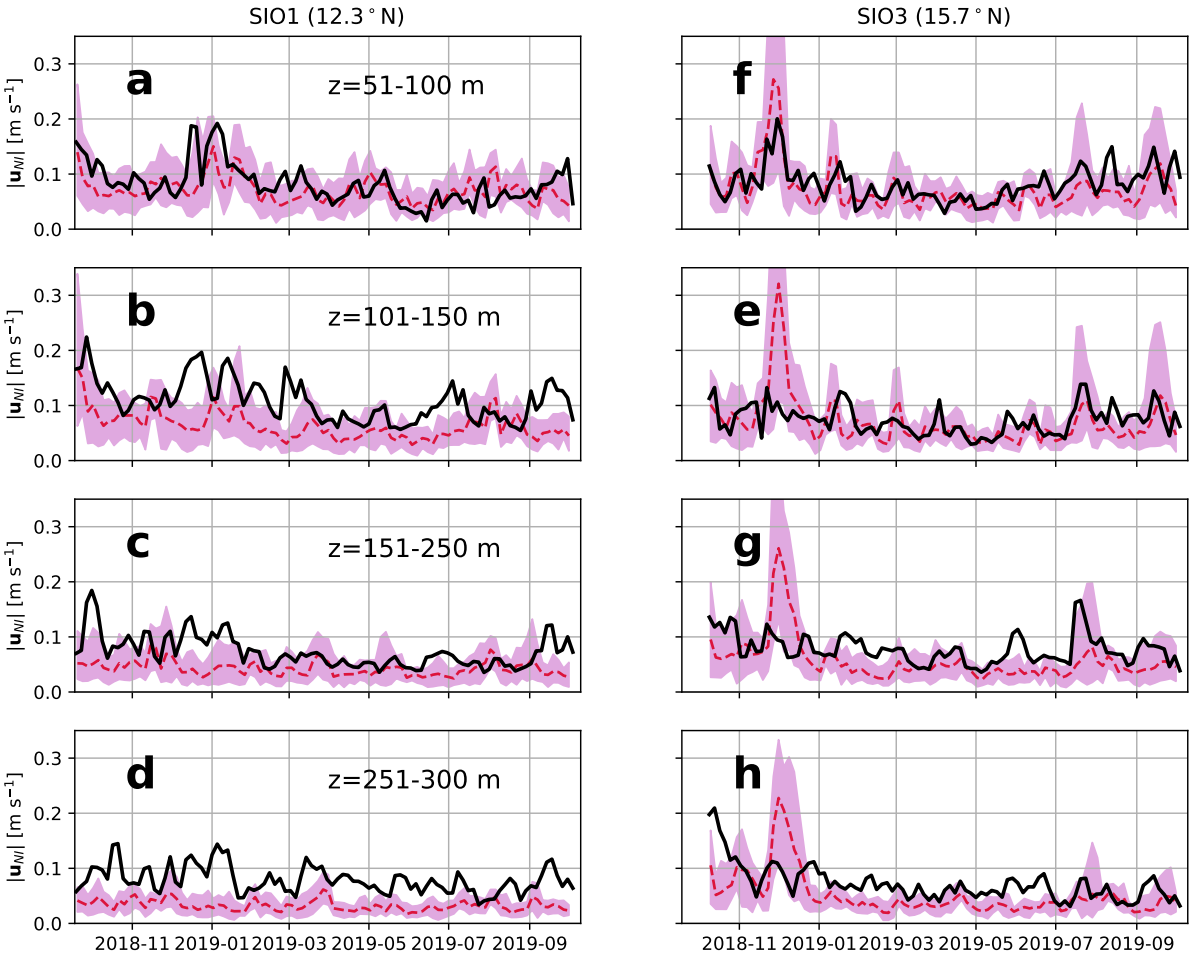

Figure 2.7. Time series of $\|\mathbf{u}_{NI}\|$ in observations and HYCOM at multiple depths. (a-d) show measurements made by mooring SIO1, while (f-h) show data from SIO3. Pink shading represents the range of $\|\mathbf{u}_{NI}\|$ within a $1^\circ \times 1^\circ$ area centered around each mooring.

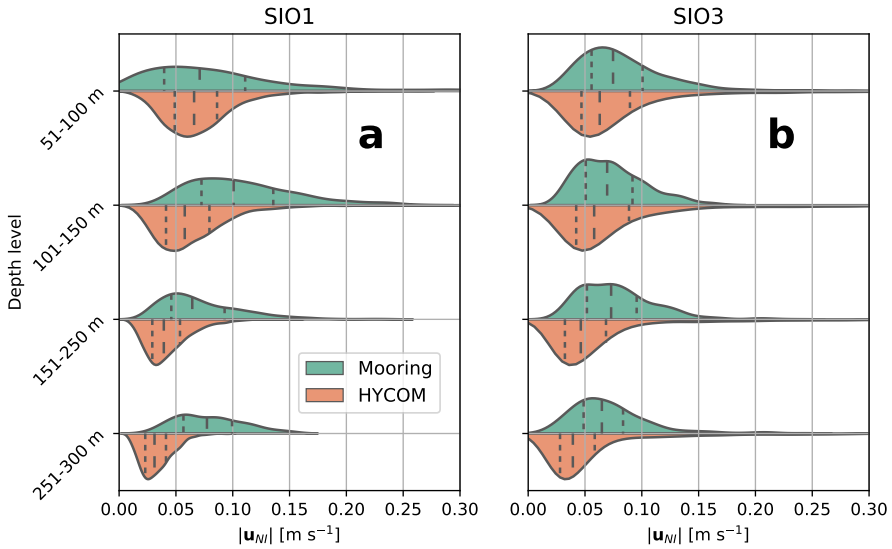

Figure 2.8. Violin plots compare the probability distributions of $\|\mathbf{u}_{NI}\|$ in mooring data (turquoise) and HYCOM (orange). The two sites considered are (**a**) SIO1 and (**b**) SIO3.

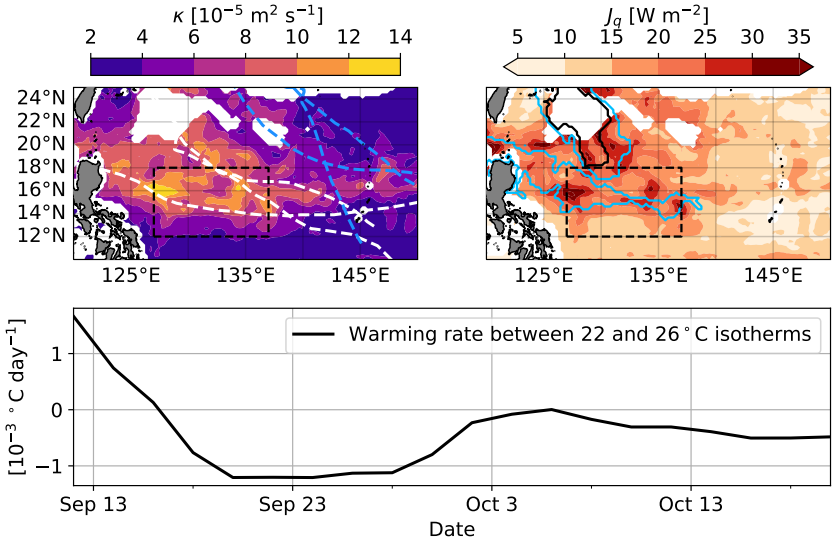

Figure 2.9. Model-based estimates of mixing. (a) κ and (b) J_q at the 26 °C isotherm were averaged between 12 September and 11 October. (c) The average warming rate between the 26 and 22 °C isotherms was computed using J_q at both levels and the vertical distance between the isotherms.

Chapter 3

Asian Monsoon impacts on Western Pacific Warm Pool mixing and heat storage

3.1 Introduction

Ocean heat stored in the Western Pacific Warm Pool (WPWP) helps drive some of the world's foremost modes of climate and weather variability including El Nino and the Hadley Circulation, the Asian Monsoon System, Intra-Seasonal Oscillations (ISOs), and tropical cyclones (TCs) (Gill, 1980; Zebiak, 1989; Fu and Wang, 2004; Vincent et al., 2014; Roxy et al., 2019). Displacements, expansions, and contractions of the WPWP are therefore key drivers of climate variability at a variety of timescales, as atmospheric deep convection that helps redistribute heat and moisture throughout the tropics and beyond typically follows the WPWP's warm sea surface temperatures (SSTs, Figs. 3.6a-c). Historical oceanographic data provide a comprehensive description of the WPWP's depth, size, and displacements (Roxy et al., 2019). However, understanding of the processes that control changes in the WPWP remains limited by a relative scarcity of observations measuring heat fluxes into and out of the WPWP, and uncertainties therein.

Time- and area-averaged estimates of the net air-sea heatflux (Q_{net}) into the WPWP vary by as much as 40 W m^{-2} between datasets (Song and Yu, 2013). Similarly, turbulent heat

fluxes (J_q) that redistribute heat in the ocean interior are unresolved by observations. Instead, oceanographers have estimated J_q using parameterizations, or as residuals that rely on the accuracy of Q_{net} and many assumptions (Godfrey and Lindstrom, 1989; McPhaden, 2002; Song and Yu, 2013). Without a clear picture of how much heat enters the WPWP through the ocean surface (Q_{net}), and how much of that heat is transferred to colder water masses (J_q), the predictive skill of general circulation models is compromised over multiple timescales and beyond the WPWP region (Wang et al., 2005; Kosaka and Xie, 2016). As the Tropical Pacific becomes increasingly recognized for its paramount role in absorbing and redistributing heat to the global ocean (Holmes et al., 2019; Forget and Ferreira, 2019), understanding the coupled ocean-atmosphere processes that regulate sea surface temperature (SST) and J_q over the WPWP is crucial to handle uncertainties in Q_{net} and improve model representations of tropical climate variability.

J_q regulates heat supply to the ocean thermocline, thereby controlling the subsurface ocean stratification and the SST response to atmospheric forcing (D'Asaro, 2003; Pujiana et al., 2018; Brizuela et al., 2023a). This way, variations in J_q can shape air-sea interactions and large scale patterns of ocean heat transport alike (Sriver and Huber, 2010; Fedorov et al., 2010; Moum et al., 2016; Holmes et al., 2019). Model simulations have repeatedly shown that weather systems and background climate are sensitive to coupling between atmospheric forcing, J_q, and its impacts on ocean stratification (Qiu et al., 2004; Luongo et al., 2023). Therefore, J_q ought to be included in our understanding of the coupled ocean-atmosphere system, but a scarcity of measurements have slowed its inclusion in dynamical frameworks and theories (MacKinnon et al., 2017).

Recent developments in sensor technology have allowed oceanographers to obtain long-term records of J_q and the turbulent diffusivity coefficient (κ) from ocean moorings (Moum and Nash, 2009). This way, multi-year deployments of microstructure turbulence sensors (χpods) have revealed how J_q regulates SST and air-sea interactions at seasonal and interannual timescales (Moum et al., 2013; Warner and Moum, 2019), as well as interactions between high-frequency

atmospheric forcing and background ocean currents that yield long-term variations in mixing (Moum et al., 2022). Furthermore, measurements made during ISO pulses suggest that variations in J_q driven by atmospheric forcing help warm the thermocline and further produce feedbacks that influence future weather (Moum et al., 2016; Pujiana et al., 2018). Cherian et al. (2020) used χpod measurements from three moorings in the Bay of Bengal to find that Monsoon wind reversals induce a biannual cycle in κ. This cycle is impactful because the near-surface stratification sharpens and SST rises when κ plunges, while enhanced κ helps redistribute freshwater supplied by river discharge that helps modulate atmospheric deep convection (Seo et al., 2009).

In this article, we synthesize the results of two year-long moored records of J_q and other parameters of ocean turbulence in the northern WPWP. The data span between September of 2018 and October of 2019, and are interpreted along with temperature data and an atmospheric reanalysis. Our analyses highlight how variations in J_q are related to local atmospheric forcing associated with the Asian Monsoon. Based on this evidence, we argue that the contributions of J_q and Q_net to seasonal displacements of the WPWP are quantitatively similar, and that J_q thus supplies WPWP heat to the large scale ocean circulation. Section 2 describes our observations and reanalysis data used in our analyses. Section 3 presents a summary of our observations and how they relate to atmospheric forcing. Section 4 presents a discussion exploring whether our analyses are representative of patterns across the WPWP region. Lastly, conclusions are laid out in Section 5.

3.2 Data and Methods

3.2.1 Moored observations

Horizontal ocean currents ($\mathbf{u} = (u, v)$), temperature (T), and the turbulent dissipation rate of temperature (χ) were observed at two mooring locations. Both moorings were deployed between October of 2018 and October of 2019 along 134.7°E, with mooring SIO1 sitting at

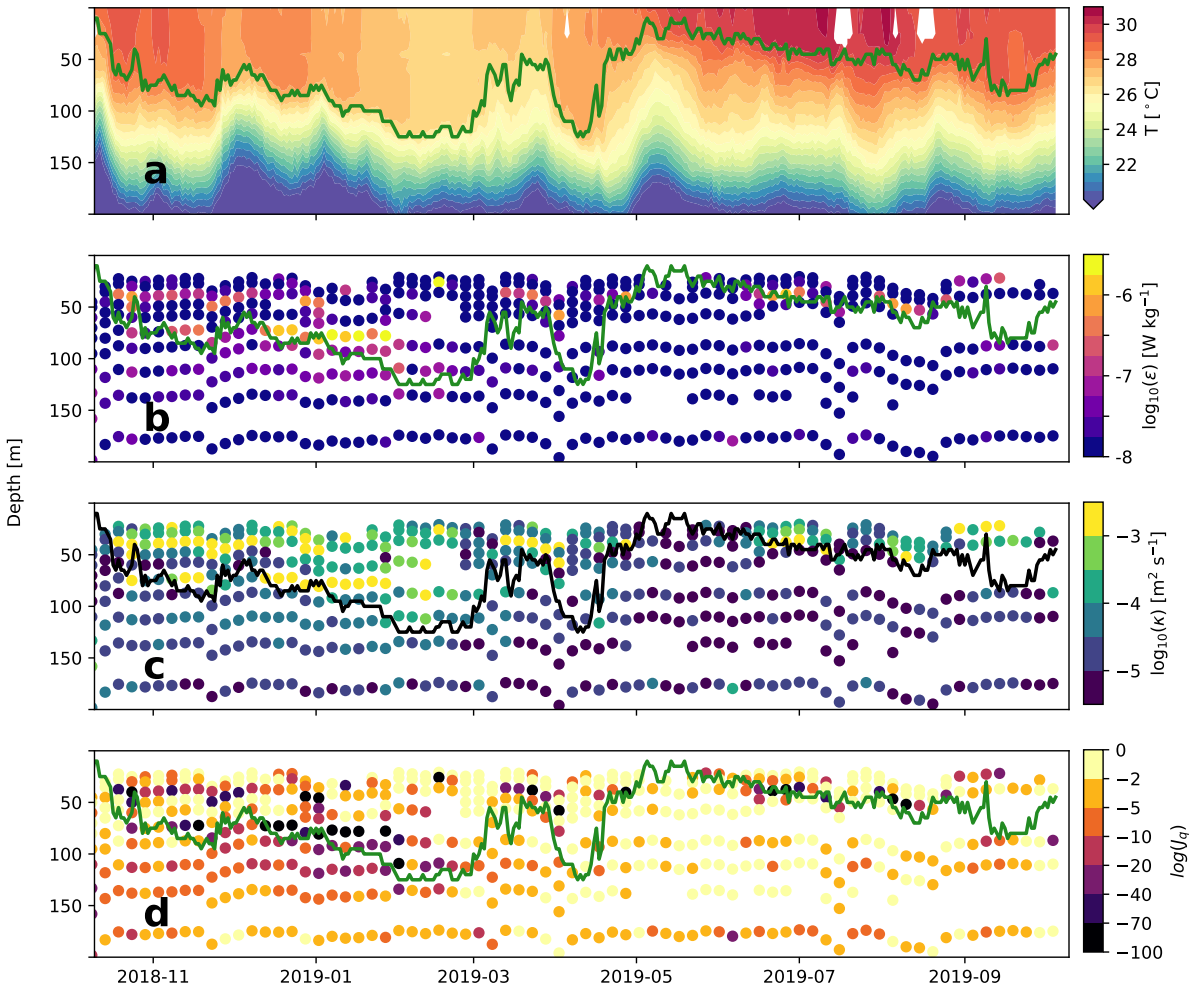

Figure 3.1. Moored observations at SIO3. (a) mean daily temperature, and five-day averages of (b) ε, (c) κ, and (d) J_q. Solid lines track the ML base as defined in the text.

12.3 and SIO3 at 15.7°N. While both moorings were equipped with 14 χpods, our analysis puts greater focus on SIO3 because its sensors were as shallow as 16 m and thus sampled the mixed layer (ML) base throughout most of the year. In our measurements, the ML base is noted by h and defined as the depth at which daily averaged T is 0.3 °C colder than the corresponding sea surface temperature (SST) in the ERA5 reanalysis. When relevant, data from SIO1 is used to verify or enrich our interpretations.

Measurements of T and of the vertical temperature gradient ($\frac{\partial T}{\partial z}$) used here were made using 70 thermistors that were distributed along the top 500 m of each mooring, including three

CTD sensors that also measured salinity and pressure. In turn, **u** comes an upward-looking 300 kHz Acoustic Doppler Current Profiler (ADCP) and a downward-looking 75 kHz ADCP, both situated roughly 80 m below the top of each mooring.

Chipods measure the time rate of change $\frac{\partial T}{\partial t}$ at a high frequency (100 Hz) and combine them with estimates of flow speed past the sensor U_{chipod} to compute empirical spectra of $\frac{\partial T}{\partial \hat{x}} = \frac{1}{U_{\text{chipod}}} \frac{\partial T}{\partial t}$. Theoretical Batchelor spectra are then fitted to empirical ones, yielding a best estimate of the temperature dissipation rate (χ), from which other turbulent quantities are derived (Moum and Nash, 2009). In particular, the turbulent kinetic energy dissipation rate (ε) is given by

$$\varepsilon = \frac{N^2 \chi}{2\Gamma \langle \frac{\partial T}{\partial z} \rangle^2}. \tag{3.1}$$

Here, $\Gamma = 0.2$ is the mixing coefficient (Osborn, 1980; Moum, 1996), N^2 is the buoyancy frequency squared, and $\langle \frac{\partial T}{\partial z} \rangle$ is the mean vertical temperature gradient calculated over a 10-minute segment. Likewise, κ is computed as

$$\kappa = \Gamma \frac{\varepsilon}{N^2}, \tag{3.2}$$

while the subsurface turbulent heatflux is estimated directly from χ as

$$J_q = \rho_0 c_p \frac{\chi}{2\langle \frac{\partial T}{\partial z} \rangle}. \tag{3.3}$$

Likewise, $\rho_0 = 1024$ kg m^{-3} is a reference density and $c_p = 3900$ J kg^{-1} K^{-1} is the heat capacity of seawater.

Because Eqs. (3.1)-(3.3) require $\langle \frac{\partial T}{\partial z} \rangle \neq 0$ to be determinate, we discard all estimates for which $\langle \frac{\partial T}{\partial z} \rangle < 0.01\,^{\circ}$C m^{-1}. This ensures that enhanced turbulence in our observations results from rapid, vigorous fluctuations in measured temperature, and not from meager fluctuations in a negligible temperature gradient. Despite this constraint, our observations include thousands of

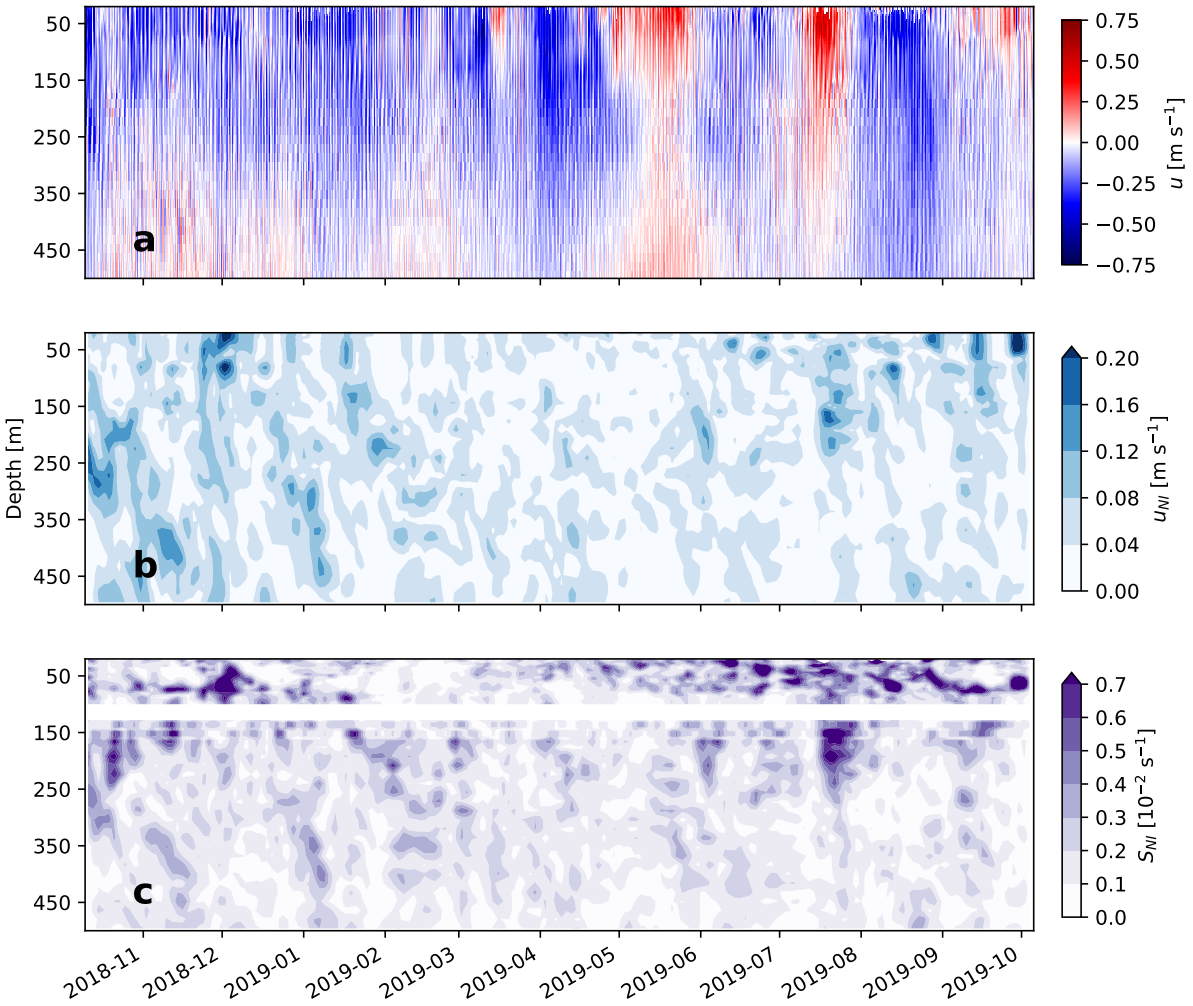

Figure 3.2. Ocean currents and NIW activity at SIO3. Zonal component of (a) **u**, and 2-day averaged magnitudes of (b) $\mathbf{u}_{NI}$ and (c) $\mathbf{S}_{NI}$ are shown.

turbulence estimates that are situated well above h (Figs. 3.1b-d). This is possible because h is defined daily, while chipods take in data on timescales at which the strictly-defined ML (where T is exactly constant) can vary greatly (Brainerd and Gregg, 1993).

Observed **u** and derived quantities in Fig. 3.2 help diagnose the drivers of thermocline mixing. In particular, we assess the level of NIW activity by extracting the near-inertial component ($\mathbf{u}_{NI}$) from **u** with a third-order Butterworth bandpass filter in the local frequency range $[0.7f, 1.3f]$. Given time-depth values of $\mathbf{u}_{NI}$ (Fig. 3.2b), we then estimate the vertical shear associated with NIWs as $\mathbf{S}_{NI} = \frac{\partial \mathbf{u}_{NI}}{\partial z}$ (Fig. 3.2c).

3.2.2 Reanalysis data

We use atmospheric and oceanic data from the ERA5 (Hersbach et al., 2018b,a) and ECCO (Wunsch et al., 2009) reanalyses. Atmospheric data from ERA5 are saved hourly and with spatial resolution $0.25^\circ \times 0.25^\circ$, including the net heat flux across the air-sea interface (Q_{net}), horizontal winds at levels 850 hPa and 10 m (noted $\mathbf{U}_{850}$ and $\mathbf{U}_{10}$ respectively), and the mean total precipitation rate P. Q_{net} is computed as

$$Q_{\text{net}} = Q_{\text{sw}} + Q_{\text{lw}} + Q_{\text{lat}} + Q_{\text{sen}}, \tag{3.4}$$

where Q_{sw}, Q_{lw}, Q_{lat}, Q_{sen} are the shortwave, longwave, latent, and sensible heat fluxes, all defined positive into the ocean. Q_{net} and Q_{lat} are used to compute the buoyancy flux (J_{b}) across the air-sea interface as

$$J_b = -\frac{g}{\rho_0}\left(\alpha Q_{\text{net}}/c_p + \beta S_0/\lambda_e\right) \tag{3.5}$$

Here, g is the gravity acceleration and ρ_0 is a reference density. Likewise, α and β are the seawater coefficients of thermal expansion and saline contraction, while c_p is the heat capacity and λ_e is the latent heat of vaporization (Carniel et al., 2012).

Lastly, we calculate the wind stress on the ocean surface (τ) as

$$\tau = C_D \rho_{\text{air}} \|\mathbf{U}_{10}\| \mathbf{U}_{10}, \tag{3.6}$$

where ρ_{air} is the density of air and C_D is a drag coefficient.

Oceanic reanalysis data, which include SST and h from ERA5 and ECCO respectively. The latter have a $1^\circ \times 1^\circ$ spatial resolution and are available between 1992 and 2018.

We describe the local climatology of air-sea interactions at SIO3 through the seasonal cycles of SST, Q_{net}, $\|\tau\|$, and P (black lines) in Fig. 3.3, where colored lines show values corresponding to our observation period. Seasonal cycles are obtained by fitting sine waves with

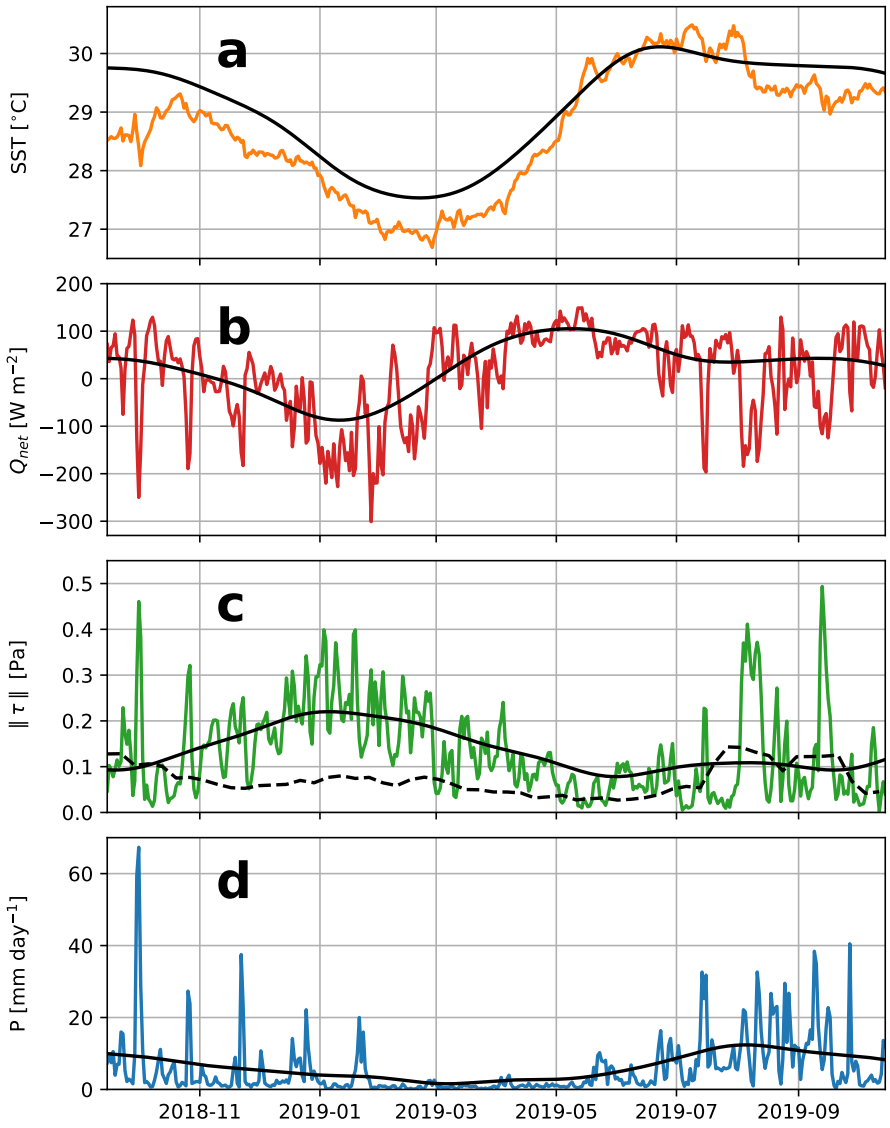

Figure 3.3. Daily reanalysis data of (a) SST, (b) Q_{net}, (c) $\|\tau\|$, and (d) precipitation averaged within a $5^\circ \times 5^\circ$ area centered over the SIO3 mooring. Climatology values area shown in black, while 2019 values are shown in color. A dashed line in (c) shows the climatological standard deviation of τ calculated with a 30-day rolling window.

periods 12, 6, 4, 3, and 2 months to ERA5 data between 1990 and 2020 using least squares. All data shown in Fig. 3.3 are area averaged within a $5^\circ \times 5^\circ$ box centered at SIO3. Large scale climatologies presented in Section 3 are derived from the ERA5 monthly average dataset.

3.2.3 Similarity scalings of ML turbulence

We use the similarity scaling

$$\varepsilon_{\text{sim}} = A\frac{u_*^3}{\|z\|} - \begin{cases} BJ_\text{b}(1 - C\frac{\|z\|}{h}) & \text{if} \quad J_\text{b} < 0 \\ 0 \quad \text{if} \quad J_\text{b} > 0 \end{cases}, \tag{3.7}$$

to assess the effects of surface forcing by $\|\tau\|$ and Q_{net} on mixing across the ML base (Fig. 3.4). The first term in the right hand side of Eq. (3.7) uses the friction velocity ($u_\star = \sqrt{\|\tau\|/\rho_0}$) to account for wind-driven turbulence. Meanwhile, the term including J_b accounts for convective turbulence driven by $Q_{\text{net}} < 0$ and evaporation ($Q_{\text{lat}} < 0$), both of which increase the density of seawater at the ocean surface (Anis and Moum, 1992).

Microstructure measurements of ε in the ocean ML under a variety of weather conditions (Shay and Gregg, 1986; Lombardo and Gregg, 1989; Anis and Moum, 1994; Carniel et al., 2012) have validated Eq. (3.7) provided that A, B, and C are adjusted empirically. We follow the results in Lombardo and Gregg (1989) and set $A = 1.76/0.4$, $B = 0.58$, and $C = 0$ to evaluate ε_{sim} under the atmospheric forcing at SIO3 (Fig. 3.3).

Chipods require a background temperature gradient to sample turbulence (Moum and Nash, 2009), and thus unable to estimate ε turbulence within a strictly-defined ML for which T is exactly constant (Anis and Moum, 1994). Therefore, a fair comparison between our observations (Fig. 3.1b) and Eq. (3.7) requires that we estimate ε at the ML base (henceforth noted ε^{ML}) and account for the suppression of turbulence therein. In particular, measurements made under a variety of forcing conditions (Lombardo and Gregg, 1989; Anis and Moum, 1994) lead us to expect that ε^{ML} will be between 25% and 70% the magnitude of ε_{sim} that corresponds to $z = h$ in

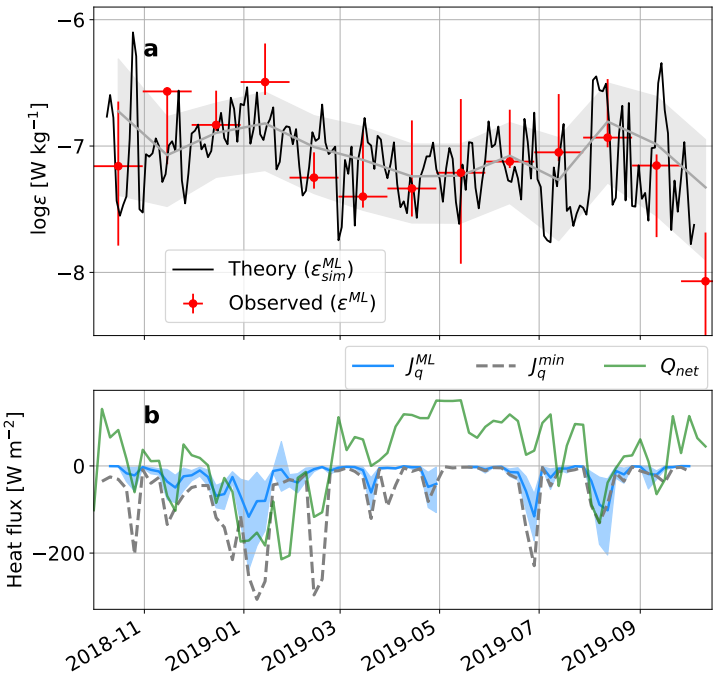

Figure 3.4. (a) Turbulent dissipation ε^{ML} in observations (30-day averages shown as red circles) and theory (black line, gray shading). (b) Q_{net} (green line), and five-day averages of J_q^{ML} (blue line). The dashed gray line in (b) shows the minimum 5-day average of J_q across all chipods. All data correspond to SIO3 (Fig. 3.1).

Eq. (3.7). Therefore, our theoretical estimates of ε at the ML base are adjusted accordingly and noted as $\varepsilon^{\text{ML}}_{\text{sim}}$. For comparison purposes, time-depth averages of χpod data within the vertical range $z \in [h-15, h+15]$ are noted by the superscript ML (e.g. ε^{ML}, J^{ML}_{q}, shown in Fig. 3.4).

3.3 Monsoon impacts on atmospheric forcing and its relations to mixing

A year-long summary of ε near the ML base (Fig. 3.4a) shows that variations in turbulence followed changes in atmospheric forcing imposed by the Asian Monsoon. Corresponding variations in J^{ML}_{q} (Fig. 3.4b) suggest that heat transfer between the ML and thermocline peak between late Summer and Winter, but is suppressed between March and June. This implies that the seasonalities of Q_{net} and J_{q} may be out of phase, allowing SST to increase rapidly when Q_{net} is large, and accelerating SST cooling throughout the Winter (Figs. 3.3a,b). In fact, J_{q} and

Q_{net} have the same order of magnitude during many of the periods when $Q_{\text{net}} < 0$ (Figs. 3.1d, 3.4b). Altogether, this suggests that heat accumulates near the ocean surface between March and June until SST peaks, and up to half of that heat is later transferred deeper into the thermocline between July and February.

A similar seasonality is observed in the thermocline, where κ is elevated for the first half of the record and later decreases (Figs. 3.5). Rather than being tied to instantaneous atmospheric forcing, thermocline κ follows similar temporal patterns as the vertical shear associated with NIWs (S_{NI}), with is normalized by the vertical temperature gradient T_z in Fig. 3.5. This implies that NIWs generated by synoptic variations in τ allow for heat transfer to continue well below the ML base, thus connecting WPWP weather and cold water masses that influence climate at higher latitudes.

To further investigate this apparent seasonality in which heat accumulates near the ocean surface during Spring and is transferred to greater depths for the rest of the year, we now explore the relations between local atmospheric forcing and large scale air-sea interactions during three stages of the Asian Monsoon. Ordered as they appear in observations, the three stages are henceforth referred to as the Winter Monsoon (NDJF, Figs. 3.6a,d), the Inter-Monsoon period (MAMJ, Figs. 3.6b,e), and the Summer Monsoon (JASO, Figs. 3.6c,f).

2-day averages of $\varepsilon_{\text{sim}}^{\text{ML}}$ (black line in Fig. 3.4a) reveal the main key difference in the nature of enhanced upper ocean mixing during the Winter and Summer Monsoons. While the monthly averages of $\varepsilon_{\text{sim}}^{\text{ML}}$ (gray shading) are quite similar for both periods, the variability in 2-day averages is drastically different. Typical low-end values $\varepsilon_{\text{sim}}^{\text{ML}} \approx 1 \times 10^{-7}$ and 2×10^{-8} W kg^{-1} during the Winter and Summer Monsoons respectively imply that enhanced upper ocean mixing at the seasonal scale results from intense background forcing during Winter, and from episodic spikes during Summer when background wind vectors are negligible (Figs. 3.3c, 3.6f). This difference is consistent with the uninterrupted appearance of enhanced J_{q} during NDJF (Fig. 3.1d) and, as we argue below, it results from the relative orientations between seasonal Monsoon winds and the easterly trade winds (ETWs).

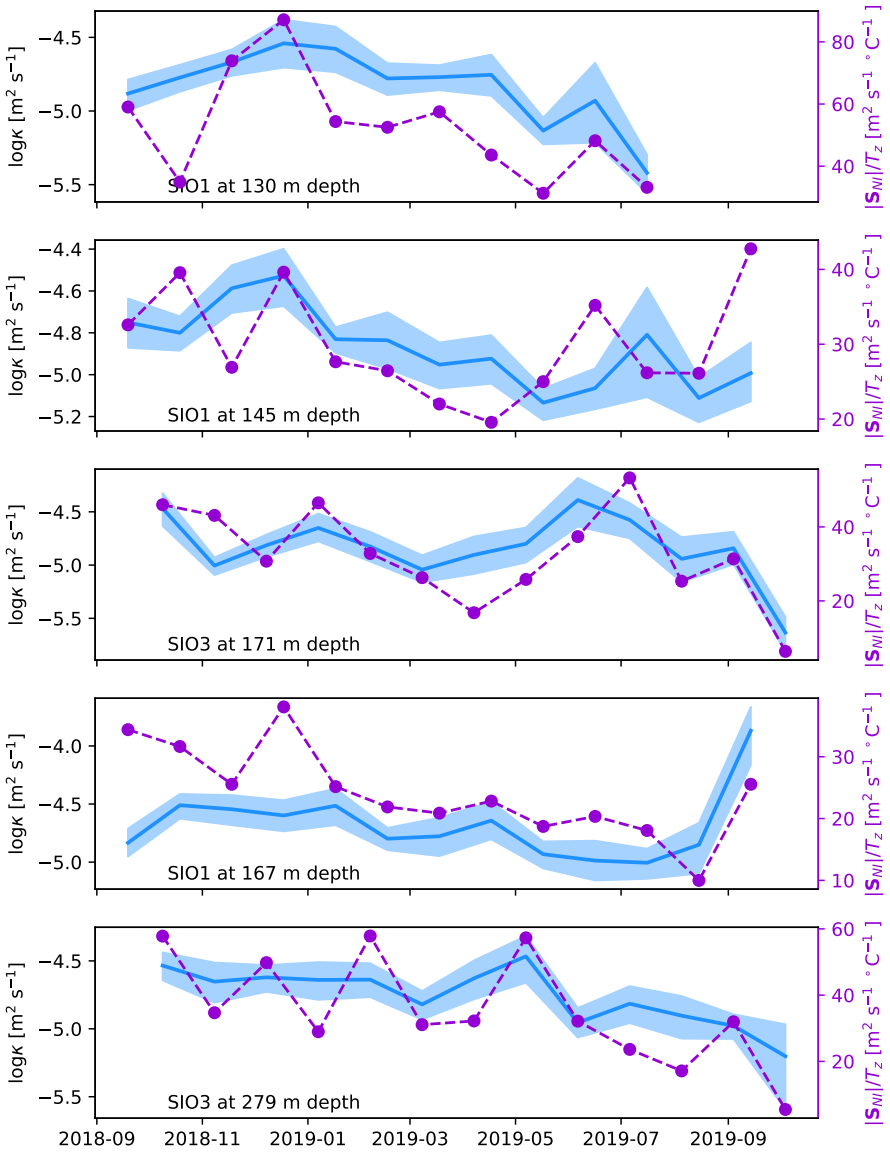

Figure 3.5. 30-day averages of κ (blue lines, left axes) are compared to corresponding values of S_{NI} (purple dashed lines, right axes) for two chipods deployed on SIO3. Blue shading corresponds to the 95% confidence intervals obtained via bootstrapping.

Because our turbulence records only span little over a year, our principal aim is not to provide a quantitative average of the seasonal cycles of turbulence. In fact, considerable gaps in our data, as well as differences in the calibrations and working conditions of individual chipods, and the patchy nature of ocean turbulence make such quantities somewhat uncertain (see for example 95% CIs in Fig. 3.4) and difficult to interpret. Instead, we seek to synthesize general patterns in our observations, explain how those relate to local atmospheric forcing, and put that forcing in the context of large scale regimes of ocean-atmosphere interaction (Fig. 3.6). Altogether, we hope that this will advance understanding of the coupling between the Asian Monsoon and the seasonality of the WPWP, while highlighting the importance of representing J_{q} in models and theories of coupled tropical climate.

The following subsections offer an overview of background and high-frequency processes of ocean-atmosphere interaction during the Winter Monsoon (NDJF), the Inter-Monsoon Period (MAMJ), and the Summer Monsoon (JASO). Climatologies of SST, Q_{net}, $\mathbf{U}_{10}$, and P over much of the Indo-Pacific Warm Pool region (Fig. 3.6) provide valuable context. Furthermore, they help inform how the patterns and principles that explain our observations (Fig. 3.4) may apply to other parts of the tropical ocean.

3.3.1 Large scale controls on J_{q}

The Asian Monsoon System (AMS) is the set of seasonal processes that rule the formation, migration, and dissipation of a large scale atmospheric convective center in the Indo-Pacific (Lau and Chan, 1983; Meehl, 1987). The Monsoon convective center forms in the Bay of Bengal during May and then migrates southeastward until February, when it arrives east of New Guinea and dissipates (Lau and Chan, 1983; Chang et al., 2006). Local precipitation rates increase drastically as the convective center moves through the Indo-Pacific. Monsoon convection enters the WPWP between July and August (Ueda et al., 1995, 2009), causing the seasonal maximum in precipitation maximum over our mooring sites (Figs. 3.3d, 3.6b).

Throughout the Indo-Pacific, seasonal anomalies in $\mathbf{U}_{10}$ are oriented towards the Monsoon

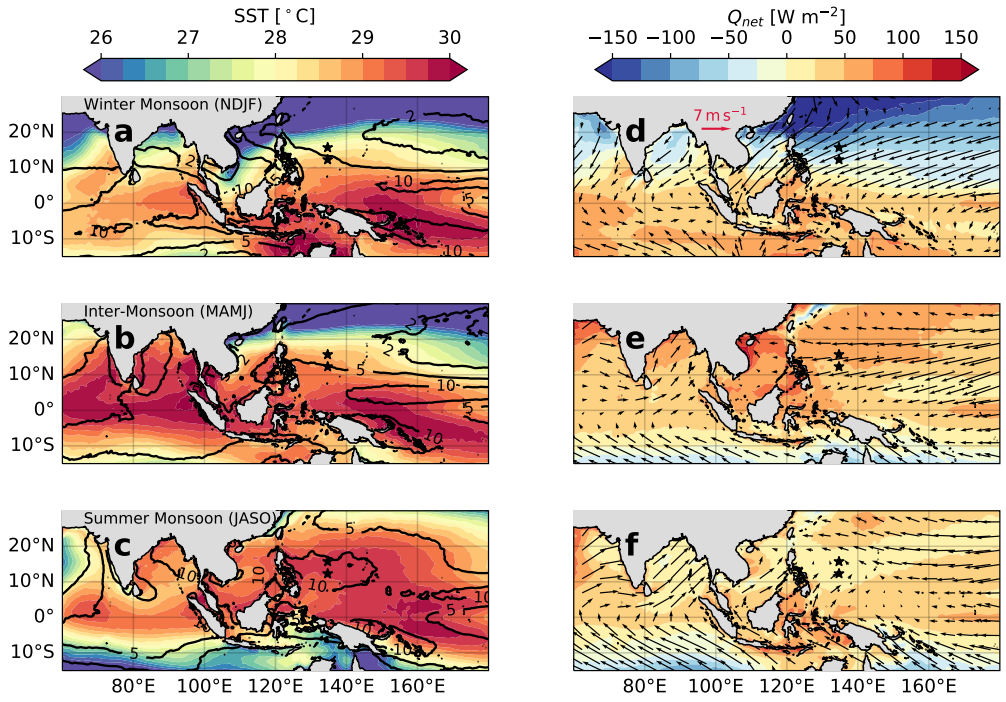

Figure 3.6. Climatological values of (a,b,c) SST and P (black contours, mm day^{-1}, (d,e,f) Q_{net} and U_{10} for March-May (top row), July-September (middle row), and November-January (bottom row).

convective center and help supply warm, moist air that sustains deep cloud formation (Fig. 3.6). Therefore, one can understand the AMS effects on atmospheric forcing over a given region as the compound effect of background, steady winds, and that of seasonal wind anomalies directed towards the Monsoon center. At our mooring site, steady forcing is done by the Easterly Trade Winds (ETWs), while seasonal anomalies are northerly during the Winter Monsoon (Fig. 3.6d), negligible during the Inter-Monsoon Period (Fig. 3.6e), and westerly during the Summer Monsoon (Fig. 3.6f).

The relative orientations between steady and seasonal winds have far-reaching consequences for Eq. (3.7) and for the development of weather systems. Because the ETWs and seasonal anomalies are orthogonal during the Winter Monsoon, they interact constructively and give rise to seasonal maxima in $\|\tau\|$ and $\|Q_{\text{lat}}\|$ (Figs. 3.3b,c). In contrast, seasonal wind anomalies are exactly opposite to the ETWs during the Summer Monsoon. This makes the climatological wind vector vanish over our moorings (Fig. 3.6f) such that the background $\|\tau\|$ is negligible. Nonetheless, large scale confluence between these two opposing air flows powers vigorous convective storms (Lau and Lau, 1992; Wu et al., 2015) that propagate through the mooring site and cause episodic peaks in $\|\tau\|$, $\|Q_{\text{lat}}\|$, and $\varepsilon_{\text{sim}}^{\text{ML}}$ (Figs. 3.3b-d, 3.4a).

Air-sea interactions during the Inter-Monsoon Period help slowly prepare the WPWP to sustain vigorous deep convection during the Summer Monsoon. Without a large scale center of deep convection over the Indo-Pacific, Monsoon wind anomalies vanish and $\|\tau\|$ weakens over the WPWP (Fig. 3.3c). Q_{net} grows to its seasonal maximum, partly because $\|Q_{\text{lat}}\|$ is reduced, and partly because Q_{sw} penetrates unabated through clear skies that are evidenced by the lack of precipitation (Figs. 3.3b,d). This causes seasonal minima in $\varepsilon_{\text{sim}}^{\text{ML}}$ and $\|J_{\text{q}}^{\text{ML}}\|$ (Fig. 3.4). With Q_{net} at its peak, and the winds leaving the upper ocean relatively undisturbed, heat supplied by Q_{net} accumulates near the ocean surface and SST rises quickly to its seasonal maximum (Figs. 3.1a,d).

3.3.2 Weather impacts on J_q and thermocline mixing

Having explained how large-scale dynamics result in the observed seasonality of J_q^{ML}, we now highlight the role of intra-seasonal and synoptic weather systems as drivers of variations in upper ocean mixing. First, we contrast the ocean response to shallow- and deep-convective storms that take place before and after the Summer Monsoon convective onset respectively (Ueda et al., 1995, 2009). Second, we contrast the NIW patterns that result from cold outbreaks and TD-like storms during the Winter and Summer Monsoons respectively, and later discuss the implications for observed variations in thermocline J_q.

Air-sea interactions before and after the Summer Monsoon convective onset

A sudden change in the patterns of SST variability during the first and second half of the period shown in Fig. 3.7 exemplifies how the arrival of the Monsoon convective center causes a qualitative shift in air-sea interactions over the WPWP. Throughout July and early August, SST oscillated between 30 and 30.5 °C, as multiple storms with peak $\|\tau\|$ between 0.2 and 0.3 Pa cooled SST but were followed by periods of large Q_{net} and weak $\|\tau\|$. However, synoptic variations in SST were suppressed after a Westerly Wind Burst sustained $\|\tau\| \approx 0.4$ Pa between August 3 and 12 and cooled SST by roughly 1 °C. Once SST fell below 29.5°C, subsequent storms and break periods failed to induce significant SST cooling and warming respectively. In what follows, we argue that this qualitative shift from seesaw-like oscillations to near-constant SST marks the arrival of the Summer Monsoon convective center, thus making this transition a hallmark of WPWP air-sea interactions during the Summer Monsoon.

Both atmospheric and oceanic factors contributed to keep SST near constant between mid August and the end of our record. First, we show that gradual changes in the upper ocean stratification partly induced by J_q helped increase the ocean's thermal inertia, therefore making SST less susceptible to atmospheric forcing and helping sustain storm intensification after the convective onset (Fig. 3.7d). Second, we propose that atmospheric shifts (Figs. 3.7b,c) associated with the local onset of convection resulted in increased ε_{sim}^{ML} and thus helped inhibit

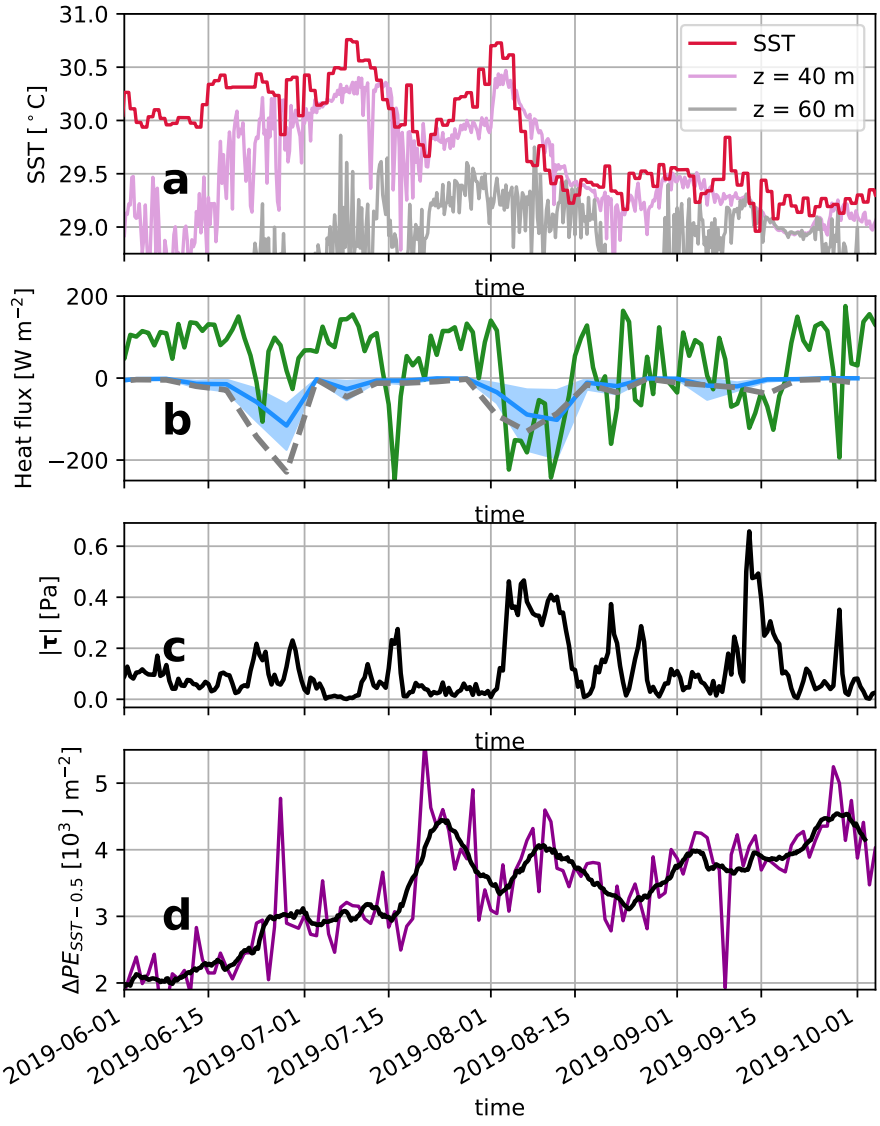

Figure 3.7. Transition between two regimes of air-sea interaction during JASO. (a) shows time series of SST from ERA5, and T at 40 and 60 m depth from SIO3, (b) lines show Q_{net} and J_{q}^{ML}. (c) shows $\|\tau\|$, and (d) shows daily values (green) and a 15-day rolling mean (black) of $\Delta PE_{\text{SST-0.25}}$.

restratification of the upper ocean and stabilized SST (Figs. 3.4a). Our observations and evidence from reanalyses suggest that this sudden, qualitative transition in air-sea interactions mediated by J_q is in fact a repetitive feature of JASO dynamics and may therefore be generalized to broader regions of the northern WPWP.

The potential energy change necessary to cool SST by 0.25 °C via near-surface mixing ($\Delta PE_{\text{SST - 0.25}}$, Fig. 3.7c) increased throughout June and July (Vincent et al., 2012b). $\Delta PE_{\text{SST-0.25}}$ increased from roughly 2 to $5 \times 10\,\text{J m}^{-2}$ between early June and early October, implying that SST became increasingly resilient to atmospheric forcing. Changes in $\Delta PE_{\text{SST-0.25}}$ result from the accumulation of heat below the ML base, which is partly induced by the cumulative effects of sporadic peaks in J_q (Fig. 3.7b). Therefore, evidence in Fig. 3.7 suggests that the history of J_q helped weaken the near-surface stratification (Figs. 3.1a,d), thereby priming the upper ocean at SIO3 to sustain stable values of Q_{lat} despite intense atmospheric forcing and ultimately help sustain storm intensification in the later part of JASO (Vincent et al., 2012b).

Qualitative shifts in the variability of $\|\tau\|$, Q_{net}, and precipitation (Figs. 3.7b,c, 3.3b-d) are also noticeable before and after SST dropped below 29.5 °C in early August. Peaks in $\|\tau\|$ grew in magnitude and increased in frequency after the SST drop; likewise, the magnitude of Q_{net} inbetween those peaks decreased (Fig. 3.7b). Changes in the contribution by Q_{sw} suggests that reduced heating of the ocean surface during break periods corresponds to increased cloud cover after the SST drop. While increases in $\Delta PE_{\text{SST-0.25}}$ help explain why storm intensity grew in mid August without causing further SST cooling, the lack of long-term SST warming is consistent with both the suppression of Q_{net} by clouds, and enhanced downward mixing of solar heat by greater $\|\tau\|$ (Fig. 3.4).

It is well established that the Summer Monsoon convective onset produces an abrupt increase in northern WPWP precipitation and atmospheric deep convection between July and August of most years (Ueda et al., 1995, 2009). However, it remains unclear whether or not the SST response and oceanic factors described above (Fig. 3.7) are representative of air-sea interactions during the convective onset in most years. In order to begin constraining the ocean's

involvement in this convective *Ueda jump* (Ueda et al., 1995), we seek evidence of concurrent *SST drops* in reanalysis data. More precisely, we process reanalysis data at SIO3 to find all events between May and October that match the following sequence of events:

1. the SST anomaly relative to climatology (SSTA) was greater than 0.3°C for 10 consecutive days or longer

2. after that, the net SST value dropped by at least 0.3°C over 6 days while the zonal wind $U_{10} > 0\,\mathrm{m\ s^{-1}}$

Conditions above were applied to corresponding variables averaged within a $5^\circ \times 5^\circ$ area centered at SIO3. 38 matching events were found between 1990 and 2020 inclusive. Data from these events were referenced in time relative to the second day of the SST cooling period, and daily values of air-sea parameters were averaged across all events to create composite event time series (Fig. 3.8). We set the condition that $\mathbf{U}_{10} > 0$ m s^{-1} to ensure that Monsoon westerly winds dominate over the ETWs at the time of SST cooling; this is a mechanistic condition that is largely necessary for the Summer Monsoon convective onset (Ueda et al., 2009) and thus helps us rule out some weak convective events that happen before the onset.

Composite timeseries in Figs. 3.8a-d show that SST cooling is concurrent with decreased OLR, increased $\|\tau\|$, and a sudden deepening of h. More importantly, they show that SST remains remains relatively stable below 29.5 °C for at least 40 days after the drop. Similar long-lasting transitions also appear in composite time series of OLR and $\|\tau\|$, which stabilize at lower and greater values respectively after the SST drop (Figs. 3.8b,c). As we argued using our observations (Fig. 3.7), these transitions imply a greater $\underset{\sim}{\varepsilon}^{\mathrm{ML}}$ after the SST drop, which would then help sustain the greater h that appears in the composite (Fig. 3.8d). The change (ΔP) in 30-day averages of precipitation before and after the *SST drop* is positive for all events (Fig. 3.8e), thus suggesting that these transitions in oceanic and atmospheric conditions are indeed characteristic of the Summer Monsoon convective onset.

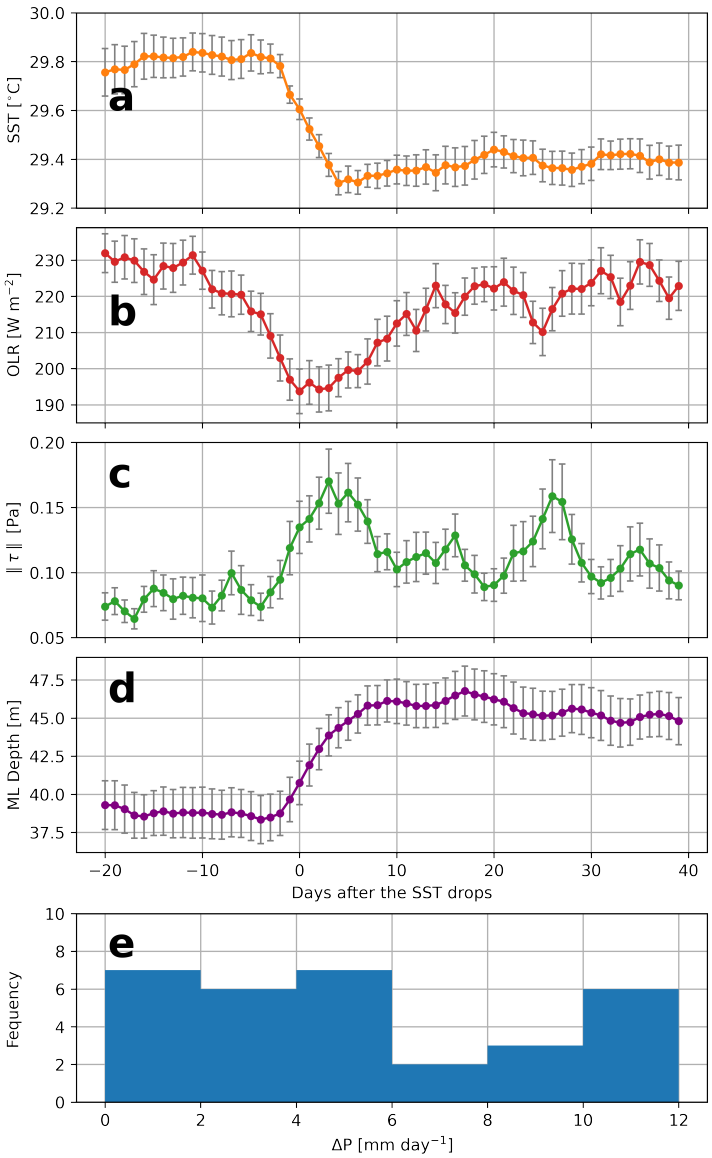

Figure 3.8. Composite view of air-sea interactions during the SST drop, constructed from 39 total events.

The joint evolution of composite timeseries in Figs. 3.8a-d is consistent with the effects of a forcing event that cools and stabilizes SST: Even though a second peak in $\|\tau\|$ tends to occur approximately 25 days after the SST drop (Fig. 3.8c), the SST impacts of that recurrent second event are barely noticeable (Fig. 3.8a). Therefore, it appears like the increase in the upper ocean's thermal inertia detailed in Figs. 3.7d and 3.8d is a recurring characteristic of oceanic conditions before and after the Summer Monsoon convective onset. Furthermore, time series of $J_{\mathrm{q}}^{\mathrm{ML}}$ in Fig. 3.7b and peaks in $\varepsilon_{\mathrm{sim}}^{\mathrm{ML}}$ suggest that the effects of weak storms between May and July might help accumulate thermocline heat, decrease the near-surface stratification, and thereby increase $\Delta PE_{\mathrm{SST\text{-}0.25}}$.

A broader view at large scale conditions concurrent with the events summarized in Fig. 3.8 shows that the sudden *SST drop* happens during active phases of the Boreal Summer Intra-Seasonal Oscillation (BSISO, Fig. 3.9). Histograms in Fig. 3.9a show that 32 out of 38 SST drop events happened during phases 4-8 of the BSISO1 index, corresponding to the only phases that capture intraseasonal convection in the WPWP region (Lee et al., 2013). Out of the 32 events that happened during active phases, 18 happened during weak pulses and 14 did so during strong ones. However, this difference is insufficient to assess whether weak rather than strong pulses are more likely to set off the convective onset and associated shifts in air-sea interactions (Figs. 3.7, 3.8).

Composite maps of SSTA and anomalous $\mathbf{U}_{10}$, and SLP (Figs. 3.9b,c) further show that *SST drops* are associated with TD-like disturbances that are embedded within BSISO active phases (Straub and Kiladis, 2003). Patterns in SSTA before the SST drop (Fig. 3.9b) show that the anomalous build up of near-surface heat in fact covers a large fraction of the northern WPWP region, and that westerly wind anomalies south of our mooring sites precede the cooling. Anomalies in $\mathbf{U}_{10}$ and SLP after the SST drop (Fig. 3.9c) clearly outline TD-like disturbances that have moved northwest of SIO3. Furthermore, the composite show that SST cooling is widespread throughout the northern WPWP and even reaches the South China Sea (Fig. 3.9d), where the positive wind curl in westerly winds induce large scale upwelling (Xie et al., 2003,

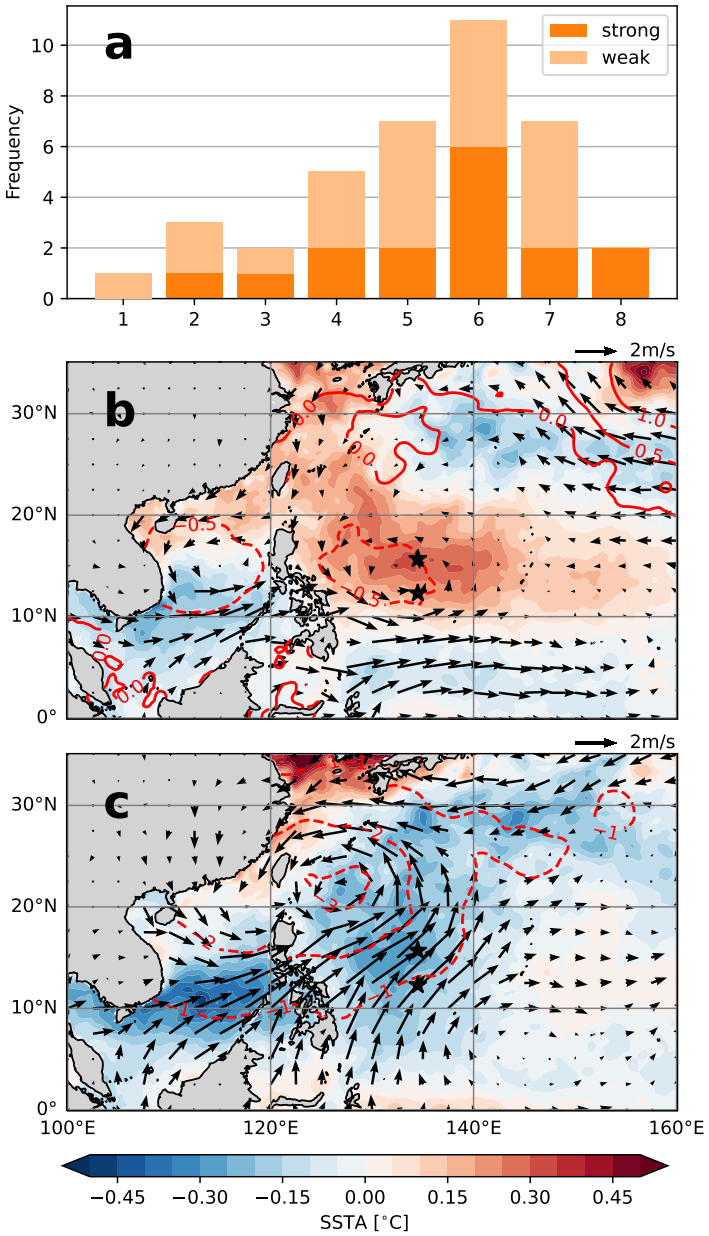

Figure 3.9. Large scale aspects of synoptic conditions associated SST cooling during the Summer Monsoon convective onset. (a) Phase of the BSISO during SST drop events used for the composite in Fig. 3.8. Average fields of SSTA and anomalies in $\mathbf{U}_{10}$ and SLP are calculated (b) 6 to 3 days before, and (c) 3 to 6 days after the SST drop, using the time convention of Fig. 3.8.

2007).

The effect of TD-like storms in cooling and stabilizing SST has a noticeable impact on the interannual variability of air-sea interactions (Fig. 3.10). We classified summertime reanalysis data into warm or cold years by calculating the mean SSTA for JJA within a $5 \times 5^{\circ}$ centered at SIO3, and setting a threshold $\pm 0.25\,^{\circ}$C for a year to be considered warm or cold, respectively (Fig. 3.10a). Composite maps of the JJA eddy kinetic energy (EKE, calculated as in Lau and Lau 1992) and corresponding anomalies in $\mathbf{U}_{850}$ for warm and cold years (Figs. 3.10b,c) reveal relationships between SSTA, storm activity, and Monsoon winds. Warm years are associated with low EKE and easterly wind anomalies over the Philippines (Fig. 3.10b), suggesting that a weakened or delayed Summer Monsoon has failed to bring vigorous convection well into the WPWP (Ueda et al., 2009), thus lowering EKE, allowing atmospheric heat to accumulate near the ocean surface, and raising SST. In contrast, cold years have Monsoon westerlies blowing well past the Philippines, thus creating a stronger convergence with the ETWs and promoting convection that raises EKE and leads to mixing of near-surface temperature gradients (Fig. 3.10c).

NIW generation and thermocline mixing

Having described how weather-induced peaks in J_{q} help modulate the value and variability of SST during the Summer Monsoon, we now focus on how weather indirectly promotes heat transfer between the seasonal and permanent thermoclines. In particular, we describe how high-frequency forcing helps generate NIWs, which transfer the energy of wind-driven currents down from the ML and thus increase the thermocline J_{q} (Brizuela et al., 2023a).

NIW activity at SIO3 was greatest during the Winter Monsoon and later decreased gradually throughout the Inter-Monsoon Period (Figs. 3.2b,c). After reaching their seasonal minima, sporadic periods of increased $\|\mathbf{u}_{NI}\|$ and $\|\mathbf{S}_{NI}\|$ began to occur in May and continued throughout JASO. Despite the influence of summertime storms, NIW activity during JASO was more sporadic and unevenly distributed throughout the water column than it was during NDJF

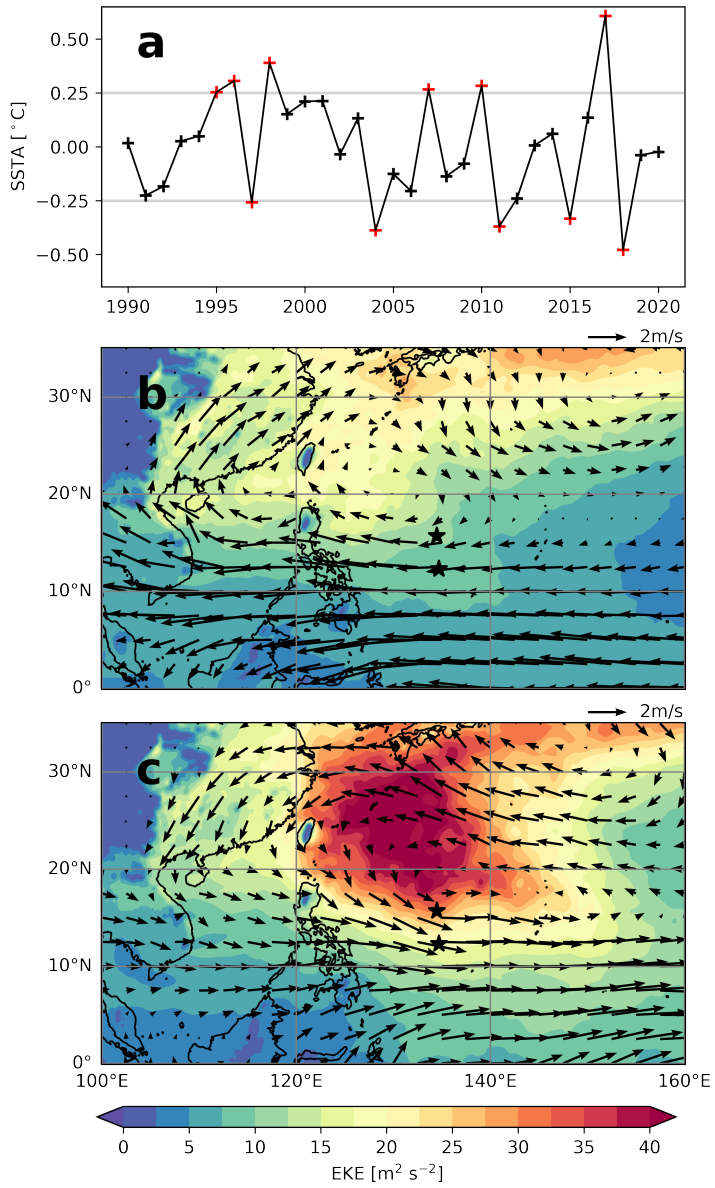

Figure 3.10. Interannual variations in JJA SSTA calculated z, EKE, and corresponding anomalies in $\mathbf{U}_{850}$ Mean values of SSTA Relation between JJA SSTA, atmospheric EKE, and large scale anomalous winds.

(Fig. 3.2b). Overall, this pattern in which MAMJ features the annual minimum of NIW activity, JASO is an intermediate period of buildup, and NDJF is the annual peak, is mirrored by observed patterns in thermocline mixing (Fig. 3.1).

The association between NIW activity and thermocline mixing is best summarized by Fig. 3.5, which compares 30-day averages of κ and the normalized shear $\|\mathbf{S}_{NI}\|/T_z$ for individual χpods from both SIO1 and SIO3. Because the time-depth distribution of NIW activity was more homogeneous during NDJF than it was during JASO, all χpods experienced increase $\|\mathbf{S}_{NI}\|/T_z$ during NDJF, but peaks in NIW activity later in our record occurred at different times for different instruments (Fig. 3.5). Patterns in synoptic atmospheric forcing that generate NIWs help explain these differences in NIW activity between NDJF and JASO.

The seasonality in the intensity of synoptic forcing at SIO3 (dashed line in Fig. 3.3c) acts as a proxy for the potential for NIW generation, and suggests that NIW activity would peak during JASO, and then be slightly weaker in NDJF. This contrasts with time-depth sections of $\|\mathbf{u}_{NI}\|$ and $\|\mathbf{S}_{NI}\|$ that show important differences between the two seasons at the thermocline (Figs. 3.2b,c). It is only when we consider morphological differences between the dominant modes of synoptic variability of each season that we can understand why thermocline NIW activity would be more homogeneous and pervasive during the Winter Monsoon, and patchy during the Summer Monsoon.

Cold outbreaks and TD-like disturbances are dominant modes of synoptic atmospheric variability during NDJF and JASO respectively (Chang et al., 2006; Lau and Lau, 1990). Cold outbreaks propagate as atmospheric fronts that move southeastward from the marginal seas of East Asia. They have along-front lengthscales $L \sim 2000\,\mathrm{km}$, and moved by our mooring site every 7 days or so, causing seesaw-like variations in $\|\tau\|$ with amplitude of approximately 0.15 Pa. In contrast, TD-like disturbances propagate as horizontally-compact pressure minima with with lengthscales $L \sim 100\,\mathrm{km}$. As such, they appear sporadically in records of $\|\tau\|$ and manifest as isolated peaks with magnitudes closer to 0.5 Pa. Therefore, cold outbreaks act as a line source of NIWs and distribute their energy more evently across the WPWP than TD-like disturbances,

which act as point sources (Kundu and Thomson, 1985).

Horizontal propagation of NIWs after storm passage then implies that local NIW activity after a synoptic disturbance will decrease more rapidly in the wake of a TD-like storm than in the wake of cold outbreak (Kundu and Thomson, 1985). This difference that arises from the morphology of storms allows NIW activity to accumulate from multiple sources and events during JASO, while JASO NIWs are as sporadic and patchy as the storms that generate them. Futhermore, the lifespan of NIWs lasts for many weeks, so NIW activity during NDJF builds on the remainings of NIWs generated in late September and October (Fig. 3.2b). In contrast, early TD-like storms put NIWs into an ocean state that has little NIW activity to begin with, given that synoptic forcing reaches a minimum during the Inter-Monsoon Period (Figs. 3.2b, 3.3c).

3.4 Discussion

Moored measurements of turbulence in the WPWP show that during periods of atmospheric cooling, heat fluxes out of the ocean and into the thermocline often contribute in similar amounts to cool SST ($J_q^{ML} \sim Q_{net} < 0$, Fig. 3.4b). This implies that, when the WPWP retreats into the deep tropics during Winter, our study region supplies a large fraction of its heat to colder water masses that may be later transported to remote areas. This result can help constrain heat budget analyses in this region, and guide similar analyses in others, as heat budget studies often infer J_q as a residual (Godfrey and Lindstrom, 1989; McPhaden, 2002; Cronin et al., 2015), even though uncertainties in Q_{net} are often as large as the mean value of Q_{net} (Song and Yu, 2013).

While the large scale conditions set by the Asian Monsoon give rise to the seasonality with which the WPWP takes up, loses, and stores heat, synoptic and intra-seasonal weather is found to have important roles in shaping the downward transfer of WPWP heat. First, synoptic weather helps increase J_q during the Summer Monsoon, thus impacting SST and the ocean's thermal inertia (Fig. 3.7). This contribution is crucial produce observed seasonal patterns in ε^{ML}, since the background forcing by $\|\tau\|$ is weak during JASO (Figs. 3.3c, 3.4). Secondly, we

highlight the role of synoptic weather in generating NIWs that allow downward heat transfer by J_q to continue well below the ML base (Figs. 3.1d, 3.5).

The important role of synoptic weather suggests that studies of large scale air-sea interaction can benefit from improving their representation of synoptic weather systems. This is in line with previous analyses suggesting that synoptic atmospheric variability is necessary to maintain SST and h at realistic values (Qiu et al., 2004; Luongo et al., 2023). Some challenges remain, however, since direct observations that can help validate parameterizations of Q_{net}, τ, and upper ocean mixing are relatively scarce under extreme atmospheric forcing (Powell et al., 2003; D'Asaro, 2003).

Numerical weather prediction in the northern WPWP is particularly challenging, since SST is negatively correlated with rainfall here, but not in most other tropical areas (Chang et al., 2006). Most people's instinct is to think that SST and tropical rainfall are related because high SSTs promote atmospheric deep convection (Gadgil et al., 1984). While this is still true in the northern WPWP, our analyses suggest that the relation between SST and rainfall is dominated by the cooling effect of storms with high $\|\tau\|$ and the enhanced J_q that is associated with that (Figs. 3.7, 3.10). Moored measurements (Fig. 3.7d) further suggest that this relationship holds because, when SST cooling is partly produced by J_q, anomalously cold SST also implies an anomalously warm thermocline, which increases the ocean's thermal inertia and its ability to sustain high-intensity storms. Further research is needed, however, to test this relation and whether it can be implemented to improve methods of weather and climate prediction.

3.5 Conclusions

Year-long measurements of turbulence in the WPWP (Fig. 3.1) detail variations in ocean turbulence associated with three stages of the Asian Monsoon (Fig. 3.4a). In the seasonal cycle that results, the WPWP expands northward during the Inter-Monsoon Period when the decreasing $\|\tau\|$ and enhanced Q_{net} lead to suppressed ML turbulence the allows heat to build up near the

ocean surface (Figs. 3.4b). Later on, westerly winds associated with the Summer Monsoon allow for the development of convective storms that increase J_q and supply heat to the thermocline (Fig. 3.7) while the northern WPWP continues to take up heat. Lastly, as the WPWP retreats back into the deep tropics during the Winter Monsoon; similar fractions of observed SST cooling during this can be attributed to Q_{net} and J_q (Figs. 3.1d, 3.6a,b, 3.4b).

Our analyses highlight how three stages of the Asian Monsoon (Fig. 3.6) each induce a different regime of air-sea interactions and turbulent ocean mixing over the WPWP. In particular, seasonal Monsoon winds help drive enhanced mixing of the upper ocean during the Summer and Winter Monsoons (Fig. 3.4). While background winds associated with the Winter Monsoon help increase ε^{ML} directly via their effect on the background wind vector and resulting $\|\tau\|$ (Figs. 3.3c, 3.6d), background winds associated with the Summer Monsoon increase ε^{ML} by flowing against the ETWs and creating a low-level convergence that promotes the development of TD-like storms (Figs. 3.10).

Chapter 3, is currently being prepared for submission for publication of the material. G. Brizuela, Noel; Xie, Shang-Ping; Alford, Matthew H.; Xia, Yi; Voet, Gunnar; Moum, James N. have contributed to the investigation. The dissertation author was the primary investigator and author of this material.

Bibliography

Alford, M. H. (2001). Internal swell generation: The spatial distribution of energy flux from the wind to mixed layer near-inertial motions. *Journal of Physical Oceanography*, 31(8):2359–2368.

Alford, M. H. (2020). Revisiting near-inertial wind work: Slab models, relative stress, and mixed layer deepening. *Journal of Physical Oceanography*, 50(11):3141–3156.

Alford, M. H. and Gregg, M. C. (2001). Near-inertial mixing: Modulation of shear, strain and microstructure at low latitude. *Journal of Geophysical Research: Oceans*, 106(C8):16947–16968.

Alford, M. H., Gregg, M. C., and Ilyas, M. (1999). Diapycnal mixing in the Banda Sea: Results of the first microstructure measurements in the Indonesian Throughflow. *Geophysical Research Letters*, 26(17):2741–2744.

Alford, M. H., MacKinnon, J. A., Pinkel, R., and Klymak, J. M. (2017). Space–time scales of shear in the north pacific. *Journal of Physical Oceanography*, 47(10):2455–2478.

Alford, M. H., Shcherbina, A. Y., and Gregg, M. C. (2013). Observations of near-inertial internal gravity waves radiating from a frontal jet. *Journal of physical oceanography*, 43(6):1225–1239.

Anis, A. and Moum, J. (1994). Prescriptions for heat flux and entrainment rates in the upper ocean during convection. *Journal of Physical Oceanography*, 24(10):2142–2155.

Anis, A. and Moum, J. N. (1992). The superadiabatic surface layer of the ocean during convection. *Journal of Physical Oceanography*, 22:1221–1221.

Asselin, O. and Young, W. R. (2020). Penetration of Wind-Generated Near-Inertial Waves into a Turbulent Ocean. *Journal of Physical Oceanography*, 50(6):1699–1716.

Balaguru, K., Chang, P., Saravanan, R., Leung, L. R., Xu, Z., Li, M., and Hsieh, J.-S. (2012). Ocean barrier layers' effect on tropical cyclone intensification. *Proceedings of the National Academy of Sciences*, 109(36):14343–14347.

Balmforth, N., Llewellyn Smith, S. G., and Young, W. (1998). Enhanced dispersion of near-inertial waves in an idealized geostrophic flow. *Journal of marine research*, 56(1):1–40.

Brainerd, K. and Gregg, M. (1993). Diurnal restratification and turbulence in the oceanic surface mixed layer: 1. Observations. *Journal of Geophysical Research: Oceans*, 98(C12):22645–22656.

Brizuela, N. G., Alford, M. H., Xie, S.-P., Sprintall, J., Voet, G., Warner, S., Hughes, K., and Moum, J. (2023a). Prolonged thermocline warming by near-inertial internal waves in the wakes of tropical cyclones.

Brizuela, N. G., Johnston, T. S., Alford, M. H., Asselin, O., Rudnick, D. L., Moum, J., Thompson, E. J., Wang, S., and Lee, C.-Y. (2023b). A vorticity-divergence view of internal wave generation by tropical cyclones: insights from Super Typhoon Mangkhut. *Journal of Geophysical Research: Oceans*, page e2022JC019400.

Bueti, M. R., Ginis, I., Rothstein, L. M., and Griffies, S. M. (2014). Tropical cyclone–induced thermocline warming and its regional and global impacts. *Journal of Climate*, 27(18):6978–6999.

Carniel, S., Kantha, L. H., Book, J. W., Sclavo, M., and Prandke, H. (2012). Turbulence variability in the upper layers of the southern adriatic sea under a variety of atmospheric forcing conditions. *Continental shelf research*, 44:39–56.

Chang, C.-P., Wang, Z., and Hendon, H. (2006). The asian winter monsoon. In Wang, B., editor, *The Asian Monsoon*, chapter 3, pages 89–127. Springer.

Chang, S. W. and Anthes, R. A. (1978). Numerical simulations of the ocean's nonlinear, baroclinic response to translating hurricanes. *Journal of Physical Oceanography*, 8(3):468–480.

Chassignet, E. P., Hurlburt, H. E., Smedstad, O. M., Halliwell, G. R., Hogan, P. J., Wallcraft, A. J., Baraille, R., and Bleck, R. (2007). The HYCOM (hybrid coordinate ocean model) data assimilative system. *Journal of Marine Systems*, 65(1-4):60–83.

Chelton, D. B., DeSzoeke, R. A., Schlax, M. G., El Naggar, K., and Siwertz, N. (1998). Geographical variability of the first baroclinic Rossby radius of deformation. *Journal of Physical Oceanography*, 28(3):433–460.

Chen, S. S. and Curcic, M. (2016). Ocean surface waves in Hurricane Ike (2008) and Superstorm Sandy (2012): Coupled model predictions and observations. *Ocean Modelling*, 103:161–176.

Cheng, L., Zhu, J., and Sriver, R. L. (2015). Global representation of tropical cyclone-induced short-term ocean thermal changes using argo data. *Ocean Science*, 11(5):719–741.

Cherian, D., Shroyer, E., Wijesekera, H., and Moum, J. (2020). The seasonal cycle of upper-ocean mixing at 8° n in the bay of bengal. *Journal of Physical Oceanography*, 50(2):323–342.

Claret, M., Lelong, M.-P., Winters, K. B., and Ourmières, Y. (2022). Wave-eddy interactions in the gulf of lion: Bridging ocean general circulation models and process ocean simulations. Technical report, Copernicus Meetings.

Crawford, G. and Large, W. (1996). A numerical investigation of resonant inertial response of the ocean to wind forcing. *Journal of physical oceanography*, 26(6):873–891.

Cronin, M. F., Pelland, N. A., Emerson, S. R., and Crawford, W. R. (2015). Estimating diffusivity from the mixed layer heat and salt balances in the n orth p acific. *Journal of Geophysical Research: Oceans*, 120(11):7346–7362.

Cuypers, Y., Le Vaillant, X., Bouruet-Aubertot, P., Vialard, J., and Mcphaden, M. J. (2013). Tropical storm-induced near-inertial internal waves during the Cirene experiment: Energy fluxes and impact on vertical mixing. *Journal of Geophysical Research: Oceans*, 118(1):358–380.

D'Asaro, E. A. (1985). The energy flux from the wind to near-inertial motions in the surface mixed layer. *Journal of Physical Oceanography*, 15(8):1043–1059.

D'Asaro, E. A. (1989). The decay of wind-forced mixed layer inertial oscillations due to the β effect. *Journal of Geophysical Research: Oceans*, 94(C2):2045–2056.

D'Asaro, E. A. (2003). The ocean boundary layer below Hurricane Dennis. *Journal of Physical Oceanography*, 33(3):561–579.

D'Asaro, E. A., Eriksen, C. C., Levine, M. D., Paulson, C. A., Niiler, P., and Van Meurs, P. (1995). Upper-ocean inertial currents forced by a strong storm. Part I: Data and comparisons with linear theory. *Journal of Physical Oceanography*, 25(11):2909–2936.

Davis, R., Sherman, J., and Dufour, J. (2001). Profiling ALACEs and other advances in autonomous subsurface floats. *Journal of atmospheric and oceanic technology*, 18(6):982–993.

Davis, R. E. (1985). Objective mapping by least squares fitting. *Journal of Geophysical Research: Oceans*, 90(C3):4773–4777.

Dillon, T. M. (1982). Vertical overturns: A comparison of thorpe and ozmidov length scales. *Journal of Geophysical Research: Oceans*, 87(C12):9601–9613.

Dunckley, J., Koseff, J., Steinbuck, J., Monismith, S., and Genin, A. (2012). Comparison of mixing efficiency and vertical diffusivity models from temperature microstructure. *Journal of*

Geophysical Research: Oceans, 117(C10).

Ekman, V. W. (1905). On the influence of the earth's rotation on ocean-currents.

Emanuel, K. (2001). Contribution of tropical cyclones to meridional heat transport by the oceans. *Journal of Geophysical Research: Atmospheres*, 106(D14):14771–14781.

Emanuel, K. (2005). Increasing destructiveness of tropical cyclones over the past 30 years. *Nature*, 436(7051):686–688.

Emanuel, K. A. (1999). Thermodynamic control of hurricane intensity. *Nature*, 401(6754):665–669.

Fairall, C. W., Bradley, E. F., Rogers, D. P., Edson, J. B., and Young, G. S. (1996). Bulk parameterization of air-sea fluxes for tropical ocean-global atmosphere coupled-ocean atmosphere response experiment. *Journal of Geophysical Research: Oceans*, 101(C2):3747–3764.

Fedorov, A. V., Brierley, C. M., and Emanuel, K. (2010). Tropical cyclones and permanent El Niño in the early Pliocene epoch. *Nature*, 463(7284):1066–1070.

Ferron, B., Mercier, H., Speer, K., Gargett, A., and Polzin, K. (1998). Mixing in the romanche fracture zone. *Journal of Physical Oceanography*, 28(10):1929–1945.

Forget, G. and Ferreira, D. (2019). Global ocean heat transport dominated by heat export from the tropical pacific. *Nature Geoscience*, 12(5):351–354.

Frankignoul, C. and Hasselmann, K. (1977). Stochastic climate models, part ii application to sea-surface temperature anomalies and thermocline variability. *Tellus*, 29(4):289–305.

Fu, X. and Wang, B. (2004). Differences of boreal summer intraseasonal oscillations simulated in an atmosphere–ocean coupled model and an atmosphere-only model. *Journal of Climate*, 17(6):1263–1271.

Gadgil, S., Joseph, P., and Joshi, N. (1984). Ocean–atmosphere coupling over monsoon regions. *Nature*, 312(5990):141–143.

Galbraith, P. S. and Kelley, D. E. (1996). Identifying overturns in ctd profiles. *Journal of Atmospheric and Oceanic Technology*, 13(3):688–702.

Ganachaud, A. and Wunsch, C. (2000). Improved estimates of global ocean circulation, heat transport and mixing from hydrographic data. *Nature*, 408(6811):453–457.

Gargett, A. and Garner, T. (2008). Determining thorpe scales from ship-lowered ctd density profiles. *Journal of Atmospheric and Oceanic Technology*, 25(9):1657–1670.

Gargett, A. E. and Moum, J. (1995). Mixing efficiencies in turbulent tidal fronts: Results from direct and indirect measurements of density flux. *Journal of Physical Oceanography*, 25(11):2583–2608.

Geisler, J. E. (1970). Linear theory of the response of a two layer ocean to a moving hurricane. *Geophysical and Astrophysical Fluid Dynamics*, 1(1-2):249–272.

Gill, A. (1984). On the behavior of internal waves in the wakes of storms. *Journal of Physical Oceanography*, 14(7):1129–1151.

Gill, A. E. (1980). Some simple solutions for heat-induced tropical circulation. *Quarterly Journal of the Royal Meteorological Society*, 106(449):447–462.

Glenn, S., Miles, T., Seroka, G., Xu, Y., Forney, R., Yu, F., Roarty, H., Schofield, O., and Kohut, J. (2016). Stratified coastal ocean interactions with tropical cyclones. *Nature Communications*, 7(1):1–10.

Godfrey, J. and Lindstrom, E. (1989). The heat budget of the equatorial western Pacific surface mixed layer. *Journal of Geophysical Research: Oceans*, 94(C6):8007–8017.

Gregg, M., d'Asaro, E., Shay, T., and Larson, N. (1986). Observations of persistent mixing and near-inertial internal waves. *Journal of Physical Oceanography*, 16(5):856–885.

Gregg, M. C. (1989). Scaling turbulent dissipation in the thermocline. *Journal of Geophysical Research: Oceans*, 94(C7):9686–9698.

Guan, S., Zhao, W., Huthnance, J., Tian, J., and Wang, J. (2014). Observed upper ocean response to typhoon Megi (2010) in the Northern South China Sea. *Journal of Geophysical Research: Oceans*, 119(5):3134–3157.

Hamann, M. M., Alford, M. H., Lucas, A. J., Waterhouse, A. F., and Voet, G. (2021). Turbulence driven by reflected internal tides in a supercritical submarine canyon. *Journal of Physical Oceanography*, 51(2):591–609.

Haney, S., Bachman, S., Cooper, B., Kupper, S., McCaffrey, K., Van Roekel, L., Stevenson, S., Fox-Kemper, B., and Ferrari, R. (2012). Hurricane wake restratification rates of one-, two-and three-dimensional processes. *Journal of Marine Research*, 70(6):824–850.

Hart, R. E. (2011). An inverse relationship between aggregate northern hemisphere tropical cyclone activity and subsequent winter climate. *Geophysical Research Letters*, 38(1).

Hautala, S. L., Reid, J. L., and Bray, N. (1996). The distribution and mixing of Pacific water masses in the Indonesian Seas. *Journal of Geophysical Research: Oceans*, 101(C5):12375–12389.

Hebert, D. and Moum, J. (1994). Decay of a near-inertial wave. *Journal of Physical Oceanography*, 24(11):2334–2351.

Hersbach, H., Bell, B., Berrisford, P., Biavati, G., Horányi, A., Muñoz Sabater, J., Nicolas, J., Peubey, C., Radu, R., and Rozum, I. (2018a). Era5 hourly data on single levels from 1959 to present. copernicus climate change service (c3s) climate data store (cds).

Hersbach, H., Bell, B., Berrisford, P., Biavati, G., Horányi, A., Muñoz Sabater, J., Nicolas, J., Peubey, C., Radu, R., Rozum, I., et al. (2018b). Era5 hourly data on pressure levels from 1979 to present, copernicus climate change service (c3s) climate data store (cds). 2018.

Hlywiak, J. and Nolan, D. S. (2019). The influence of oceanic barrier layers on tropical cyclone intensity as determined through idealized, coupled numerical simulations. *Journal of Physical Oceanography*, 49(7):1723–1745.

Holmes, R. M., Zika, J. D., and England, M. H. (2019). Diathermal heat transport in a global ocean model. *Journal of Physical Oceanography*, 49(1):141–161.

Huang, P., Sanford, T. B., and Imberger, J. (2009). Heat and turbulent kinetic energy budgets for surface layer cooling induced by the passage of Hurricane Frances (2004). *Journal of Geophysical Research: Oceans*, 114(C12).

Huffman, G. J., Bolvin, D. T., Braithwaite, D., Hsu, K., Joyce, R., Xie, P., and Yoo, S.-H. (2015). NASA global precipitation measurement (GPM) integrated multi-satellite retrievals for GPM (IMERG). *Algorithm Theoretical Basis Document (ATBD) Version*, 4:26.

Hughes, K. G., Moum, J. N., and Shroyer, E. L. (2020a). Evolution of the velocity structure in the diurnal warm layer. *Journal of Physical Oceanography*, 50(3):615–631.

Hughes, K. G., Moum, J. N., and Shroyer, E. L. (2020b). Heat transport through diurnal warm layers. *Journal of Physical Oceanography*, 50(10):2885–2905.

Hummels, R., Dengler, M., Rath, W., Foltz, G. R., Schütte, F., Fischer, T., and Brandt, P. (2020). Surface cooling caused by rare but intense near-inertial wave induced mixing in the tropical atlantic. *Nature communications*, 11(1):1–13.

Jacob, S. D., Shay, L. K., Mariano, A. J., and Black, P. G. (2000). The 3D oceanic mixed layer response to Hurricane Gilbert. *Journal of Physical Oceanography*, 30(6):1407–1429.

Jaimes, B. and Shay, L. K. (2010). Near-inertial wave wake of Hurricanes Katrina and Rita over mesoscale oceanic eddies. *Journal of Physical Oceanography*, 40(6):1320–1337.

Jansen, M. and Ferrari, R. (2009). Impact of the latitudinal distribution of tropical cyclones on ocean heat transport. *Geophysical Research Letters*, 36(6).

Jansen, M. F., Ferrari, R., and Mooring, T. A. (2010). Seasonal versus permanent thermocline warming by tropical cyclones. *Geophysical Research Letters*, 37(3).

Jochum, M., Briegleb, B. P., Danabasoglu, G., Large, W. G., Norton, N. J., Jayne, S. R., Alford, M. H., and Bryan, F. O. (2013). The impact of oceanic near-inertial waves on climate. *Journal of Climate*, 26(9):2833–2844.

Johnson, H. L. and Garrett, C. (2004). Effects of noise on thorpe scales and run lengths. *Journal of physical oceanography*, 34(11):2359–2372.

Johnston, T. M. S., Chaudhuri, D., Mathur, M., Rudnick, D. L., Sengupta, D., Simmons, H. L., Tandon, A., and Venkatesan, R. (2016). Decay mechanisms of near-inertial mixed layer oscillations in the Bay of Bengal. *Oceanography*, 29(2):180–191.

Johnston, T. M. S. and Rudnick, D. (2021). Float trajectory and CTD data [Dataset]. *NASA*.

Johnston, T. M. S. and Rudnick, D. L. (2009). Observations of the transition layer. *Journal of physical oceanography*, 39(3):780–797.

Johnston, T. M. S., Rudnick, D. L., Brizuela, N., and Moum, J. N. (2020). Advection by the North Equatorial Current of a cold wake due to multiple typhoons in the western Pacific: Measurements from a profiling float array. *Journal of Geophysical Research: Oceans*, 125(4):e2019JC015534.

Johnston, T. M. S., Wang, S., Lee, C.-Y., Moum, J. N., Rudnick, D. L., and Sobel, A. (2021). Near-inertial wave propagation in the wake of Super Typhoon Mangkhut: Measurements from a profiling float array. *Journal of Geophysical Research: Oceans*, page e2020JC016749.

Joint Typhoon Warning Center (2022). Western North Pacific Ocean Best Track Data [Dataset]. *U.S. Navy*.

Jourdain, N. C., Lengaigne, M., Vialard, J., Madec, G., Menkès, C. E., Vincent, E. M., Jullien, S., and Barnier, B. (2013). Observation-based estimates of surface cooling inhibition by heavy rainfall under tropical cyclones. *Journal of Physical Oceanography*, 43(1):205–221.

Korty, R. L., Emanuel, K. A., and Scott, J. R. (2008). Tropical cyclone–induced upper-ocean mixing and climate: Application to equable climates. *Journal of Climate*, 21(4):638–654.

Kosaka, Y. and Xie, S.-P. (2016). The tropical pacific as a key pacemaker of the variable rates of global warming. *Nature Geoscience*, 9(9):669–673.

Kraus, E. and Turner, J. (1967). A one-dimensional model of the seasonal thermocline ii. the general theory and its consequences. *Tellus*, 19(1):98–106.

Kundu, P. K. and Thomson, R. E. (1985). Inertial oscillations due to a moving front. *Journal of physical oceanography*, 15(8):1076–1084.

Kunze, E. (1985). Near-inertial wave propagation in geostrophic shear. *Journal of Physical Oceanography*, 15(5):544–565.

Kunze, E. and Sanford, T. B. (1984). Observations of near-inertial waves in a front. *Journal of Physical Oceanography*, 14(3):566–581.

Large, W. and Pond, S. (1981). Open ocean momentum flux measurements in moderate to strong winds. *Journal of Physical Oceanography*, 11(3):324–336.

Lau, K.-H. and Lau, N.-C. (1990). Observed structure and propagation characteristics of tropical summertime synoptic scale disturbances. *Monthly Weather Review*, 118(9):1888–1913.

Lau, K.-H. and Lau, N.-C. (1992). The energetics and propagation dynamics of tropical summertime synoptic-scale disturbances. *Monthly weather review*, 120(11):2523–2539.

Lau, K.-M. and Chan, P. H. (1983). Short-term climate variability and atmospheric teleconnections from satellite-observed outgoing longwave radiation. part i: Simultaneous relationships. *Journal of the Atmospheric Sciences*, 40(12):2735–2750.

Le Traon, P., Nadal, F., and Ducet, N. (1998). An improved mapping method of multisatellite altimeter data. *Journal of atmospheric and oceanic technology*, 15(2):522–534.

Leaman, K. D. and Sanford, T. B. (1975). Vertical energy propagation of inertial waves: A vector spectral analysis of velocity profiles. *Journal of Geophysical Research*, 80(15):1975–1978.

Lee, J.-Y., Wang, B., Wheeler, M. C., Fu, X., Waliser, D. E., and Kang, I.-S. (2013). Real-time multivariate indices for the boreal summer intraseasonal oscillation over the asian summer monsoon region. *Climate Dynamics*, 40:493–509.

Leipper, D. F. and Volgenau, D. (1972). Hurricane heat potential of the gulf of mexico. *Journal of Physical Oceanography*, 2(3):218–224.

Liu, J., Curry, J. A., Clayson, C. A., and Bourassa, M. A. (2011). High-resolution satellite surface latent heat fluxes in north atlantic hurricanes. *Monthly Weather Review*, 139(9):2735–2747.

Lombardo, C. and Gregg, M. (1989). Similarity scaling of viscous and thermal dissipation in a convecting surface boundary layer. *Journal of Geophysical Research: Oceans*, 94(C5):6273–6284.

Luongo, M. T., Brizuela, N., Eisenman, I., and Xie, S.-P. (2023). Retaining short-term variability reduces biases in wind stress overriding simulations. *Authorea Preprints*.

MacKinnon, J. and Gregg, M. (2005). Near-inertial waves on the New England shelf: The role of evolving stratification, turbulent dissipation, and bottom drag. *Journal of Physical Oceanography*, 35(12):2408–2424.

MacKinnon, J. A., Zhao, Z., Whalen, C. B., Waterhouse, A. F., Trossman, D. S., Sun, O. M., Laurent, L. C. S., Simmons, H. L., Polzin, K., Pinkel, R., et al. (2017). Climate process team on internal wave–driven ocean mixing. *Bulletin of the American Meteorological Society*, 98(11):2429–2454.

Manucharyan, G., Brierley, C., and Fedorov, A. (2011). Climate impacts of intermittent upper ocean mixing induced by tropical cyclones. *Journal of Geophysical Research: Oceans*, 116(C11).

Mater, B. D., Venayagamoorthy, S. K., St. Laurent, L., and Moum, J. N. (2015). Biases in thorpe-scale estimates of turbulence dissipation. part i: Assessments from large-scale overturns in oceanographic data. *Journal of Physical Oceanography*, 45(10):2497–2521.

McPhaden, M. J. (2002). Mixed layer temperature balance on intraseasonal timescales in the equatorial pacific ocean. *Journal of climate*, 15(18):2632–2647.

Meehl, G. A. (1987). The annual cycle and interannual variability in the tropical Pacific and Indian Ocean regions. *Monthly Weather Review*, 115(1):27–50.

Mei, W., Primeau, F., McWilliams, J. C., and Pasquero, C. (2013). Sea surface height evidence for long-term warming effects of tropical cyclones on the ocean. *Proceedings of the National Academy of Sciences*, 110(38):15207–15210.

Menkes, C. E., Lengaigne, M., Lévy, M., Ethé, C., Bopp, L., Aumont, O., Vincent, E., Vialard, J., and Jullien, S. (2016). Global impact of tropical cyclones on primary production. *Global Biogeochemical Cycles*, 30(5):767–786.

Moum, J. (1996). Efficiency of mixing in the main thermocline. *Journal of Geophysical Research: Oceans*, 101(C5):12057–12069.

Moum, J., Farmer, D., Smyth, W., Armi, L., and Vagle, S. (2003). Structure and generation of turbulence at interfaces strained by internal solitary waves propagating shoreward over the continental shelf. *Journal of Physical Oceanography*, 33(10):2093–2112.

Moum, J., Gregg, M., Lien, R., and Carr, M. (1995). Comparison of turbulence kinetic energy dissipation rate estimates from two ocean microstructure profilers. *Journal of Atmospheric and Oceanic Technology*, 12(2):346–366.

Moum, J. and Nash, J. (2009). Mixing measurements on an equatorial ocean mooring. *Journal of Atmospheric and Oceanic Technology*, 26(2):317–336.

Moum, J. N., Hughes, K. G., Shroyer, E. L., Smyth, W. D., Cherian, D., Warner, S. J., Bourlès, B., Brandt, P., and Dengler, M. (2022). Deep cycle turbulence in Atlantic and Pacific cold tongues. *Geophysical Research Letters*, 49(8):e2021GL097345.

Moum, J. N., Perlin, A., Nash, J. D., and McPhaden, M. J. (2013). Seasonal sea surface cooling in the equatorial pacific cold tongue controlled by ocean mixing. *Nature*, 500(7460):64–67.

Moum, J. N., Pujiana, K., Lien, R.-C., and Smyth, W. D. (2016). Ocean feedback to pulses of the madden–julian oscillation in the equatorial indian ocean. *Nature communications*, 7(1):13203.

Mrvaljevic, R. K., Black, P. G., Centurioni, L. R., Chang, Y.-T., D'Asaro, E. A., Jayne, S. R., Lee, C. M., Lien, R.-C., Lin, I.-I., Morzel, J., et al. (2013). Observations of the cold wake of typhoon fanapi (2010). *Geophysical Research Letters*, 40(2):316–321.

Nagai, T., Tandon, A., Kunze, E., and Mahadevan, A. (2015). Spontaneous generation of near-inertial waves by the kuroshio front. *Journal of Physical Oceanography*, 45(9):2381–2406.

Névir, P. and Sommer, M. (2009). Energy–vorticity theory of ideal fluid mechanics. *Journal of the Atmospheric Sciences*, 66(7):2073–2084.

Nilsson, J. (1995). Energy flux from traveling hurricanes to the oceanic internal wave field. *Journal of Physical Oceanography*, 25(4):558–573.

Osborn, T. (1980). Estimates of the local rate of vertical diffusion from dissipation measurements. *Journal of physical oceanography*, 10(1):83–89.

Park, J. J., Kwon, Y.-O., and Price, J. F. (2011). Argo array observation of ocean heat content changes induced by tropical cyclones in the north pacific. *Journal of Geophysical Research: Oceans*, 116(C12).

Pasquero, C., Desbiolles, F., and Meroni, A. N. (2021). Air-sea interactions in the cold wakes of tropical cyclones. *Geophysical Research Letters*, 48(2):e2020GL091185.

Pollard, R. T. and Millard, R. (1970). Comparison between observed and simulated wind-generated inertial oscillations. In *Deep Sea Research and Oceanographic Abstracts*, volume 17, pages 813–821. Elsevier.

Pollard, R. T., Rhines, P. B., and Thompson, R. O. (1973). The deepening of the wind-mixed layer. *Geophysical Fluid Dynamics*, 4(4):381–404.

Powell, M. D., Vickery, P. J., and Reinhold, T. A. (2003). Reduced drag coefficient for high wind speeds in tropical cyclones. *Nature*, 422(6929):279–283.

Price, J. F. (1981). Upper ocean response to a hurricane. *Journal of Physical Oceanography*,

11(2):153–175.

Price, J. F. (1983). Internal wave wake of a moving storm. Part I. Scales, energy budget and observations. *Journal of Physical Oceanography*, 13(6):949–965.

Price, J. F., Morzel, J., and Niiler, P. P. (2008). Warming of sst in the cool wake of a moving hurricane. *Journal of Geophysical Research: Oceans*, 113(C7).

Price, J. F., Sanford, T. B., and Forristall, G. Z. (1994). Forced stage response to a moving hurricane. *Journal of Physical Oceanography*, 24(2):233–260.

Price, J. F., Weller, R. A., and Pinkel, R. (1986). Diurnal cycling: Observations and models of the upper ocean response to diurnal heating, cooling, and wind mixing. *Journal of Geophysical Research: Oceans*, 91(C7):8411–8427.

Pujiana, K., Moum, J. N., and Smyth, W. D. (2018). The role of turbulence in redistributing upper-ocean heat, freshwater, and momentum in response to the MJO in the equatorial Indian Ocean. *Journal of Physical Oceanography*, 48(1):197–220.

Qiu, B., Chen, S., and Hacker, P. (2004). Synoptic-scale air–sea flux forcing in the western north pacific: Observations and their impact on sst and the mixed layer. *Journal of Physical Oceanography*, 34(10):2148–2159.

Reul, N., Chapron, B., Grodsky, S. A., Guimbard, S., Kudryavtsev, V., Foltz, G. R., and Balaguru, K. (2021). Satellite observations of the sea surface salinity response to tropical cyclones. *Geophysical research letters*, 48(1):e2020GL091478.

Roemmich, D. and Gilson, J. (2001). Eddy transport of heat and thermocline waters in the north pacific: A key to interannual/decadal climate variability? *Journal of Physical Oceanography*, 31(3):675–687.

Roemmich, D. and Gilson, J. (2009). The 2004–2008 mean and annual cycle of temperature, salinity, and steric height in the global ocean from the argo program. *Progress in oceanography*, 82(2):81–100.

Roxy, M., Dasgupta, P., McPhaden, M. J., Suematsu, T., Zhang, C., and Kim, D. (2019). Twofold expansion of the Indo-Pacific warm pool warps the MJO life cycle. *Nature*, 575(7784):647–651.

Rudzin, J. E., Shay, L. K., and Jaimes de la Cruz, B. (2019). The impact of the Amazon–Orinoco River plume on enthalpy flux and air–sea interaction within Caribbean Sea tropical cyclones. *Monthly Weather Review*, 147(3):931–950.

Salmon, R. (2007). A general method for conserving energy and potential enstrophy in shallow-

water models. *Journal of the Atmospheric Sciences*, 64(2):515–531.

Sanabia, E. R. and Jayne, S. R. (2020). Ocean observations under two major hurricanes: Evolution of the response across the storm wakes. *AGU Advances*, 1(3):e2019AV000161.

Sanford, T. B., Ma, B. B., and Alford, M. H. (2021). Stalling and dissipation of a near-inertial wave (niw) in an anticyclonic ocean eddy: Direct determination of group velocity and comparison with theory. *Journal of Geophysical Research: Oceans*, 126(5):e2020JC016742.

Schade, L. R. and Emanuel, K. A. (1999). The ocean's effect on the intensity of tropical cyclones: Results from a simple coupled atmosphere–ocean model. *Journal of the Atmospheric Sciences*, 56(4):642–651.

Scoccimarro, E., Gualdi, S., Bellucci, A., Sanna, A., Giuseppe Fogli, P., Manzini, E., Vichi, M., Oddo, P., and Navarra, A. (2011). Effects of tropical cyclones on ocean heat transport in a high-resolution coupled general circulation model. *Journal of Climate*, 24(16):4368–4384.

Scotti, A. (2015). Biases in thorpe-scale estimates of turbulence dissipation. part ii: Energetics arguments and turbulence simulations. *Journal of Physical Oceanography*, 45(10):2522–2543.

Seo, H., Xie, S.-P., Murtugudde, R., Jochum, M., and Miller, A. J. (2009). Seasonal effects of indian ocean freshwater forcing in a regional coupled model. *Journal of Climate*, 22(24):6577–6596.

Shay, L. K. and Chang, S. W. (1997). Free surface effects on the near-inertial ocean current response to a hurricane: A revisit. *Journal of Physical Oceanography*, 27(1):23–39.

Shay, L. K., Elsberry, R. L., and Black, P. G. (1989). Vertical structure of the ocean current response to a hurricane. *Journal of Physical Oceanography*, 19(5):649–669.

Shay, L. K., Goni, G. J., and Black, P. G. (2000). Effects of a warm oceanic feature on hurricane opal. *Monthly Weather Review*, 128(5):1366–1383.

Shay, L. K., Mariano, A. J., Jacob, S. D., and Ryan, E. H. (1998). Mean and near-inertial ocean current response to Hurricane Gilbert. *Journal of Physical Oceanography*, 28(5):858–889.

Shay, T. J. and Gregg, M. (1986). Convectively driven turbulent mixing in the upper ocean. *Journal of Physical Oceanography*, 16(11):1777–1798.

Skamarock, W. C., Klemp, J. B., Dudhia, J., Gill, D. O., Barker, D. M., Wang, W., and Powers, J. G. (2008). A description of the Advanced Research WRF version 3. NCAR Technical note-475+ STR.

Smyth, W., Moum, J., and Caldwell, D. (2001). The efficiency of mixing in turbulent patches:

Inferences from direct simulations and microstructure observations. *Journal of Physical Oceanography*, 31(8):1969–1992.

Smyth, W., Zavialov, P., and Moum, J. (1997). Decay of turbulence in the upper ocean following sudden isolation from surface forcing. *Journal of Physical Oceanography*, 27(5):810–822.

Sobel, A. H., Sprintall, J., Maloney, E. D., Martin, Z. K., Wang, S., de Szoeke, S. P., Trabing, B. C., and Rutledge, S. A. (2021). Large-scale state and evolution of the atmosphere and ocean during piston 2018. *Journal of Climate*, 34(12):5017–5035.

Song, X. and Yu, L. (2013). How much net surface heat flux should go into the western pacific warm pool? *Journal of Geophysical Research: Oceans*, 118(7):3569–3585.

Sriver, R. L., Goes, M., Mann, M. E., and Keller, K. (2010). Climate response to tropical cyclone-induced ocean mixing in an Earth system model of intermediate complexity. *Journal of Geophysical Research: Oceans*, 115(C10).

Sriver, R. L. and Huber, M. (2007). Observational evidence for an ocean heat pump induced by tropical cyclones. *Nature*, 447(7144):577–580.

Sriver, R. L. and Huber, M. (2010). Modeled sensitivity of upper thermocline properties to tropical cyclone winds and possible feedbacks on the Hadley circulation. *Geophysical Research Letters*, 37(8).

Sriver, R. L., Huber, M., and Nusbaumer, J. (2008). Investigating tropical cyclone-climate feedbacks using the trmm microwave imager and the quick scatterometer. *Geochemistry, Geophysics, Geosystems*, 9(9).

Straub, K. H. and Kiladis, G. N. (2003). Interactions between the boreal summer intraseasonal oscillation and higher-frequency tropical wave activity. *Monthly Weather Review*, 131(5):945–960.

Talley, L. D. (2003). Shallow, intermediate, and deep overturning components of the global heat budget. *Journal of Physical oceanography*, 33(3):530–560.

Thomas, L. N., Rainville, L., Asselin, O., Young, W. R., Girton, J., Whalen, C. B., Centurioni, L., and Hormann, V. (2020). Direct observations of near-inertial wave ζ-refraction in a dipole vortex. *Geophysical Research Letters*, 47(21):e2020GL090375.

Thompson, A., Gille, S. T., MacKinnon, J. A., and Sprintall, J. (2007). Spatial and temporal patterns of small-scale mixing in Drake Passage. *Journal of Physical Oceanography*, 37(3):572–592.

Thompson, E. J., Moum, J. N., Fairall, C. W., and Rutledge, S. A. (2019). Wind limits on rain

layers and diurnal warm layers. *Journal of Geophysical Research: Oceans*, 124(2):897–924.

Thorpe, S. (1977). Turbulence and mixing in a Scottish loch. *Philosophical Transactions of the Royal Society of London. Series A, Mathematical and Physical Sciences*, 286(1334):125–181.

Turner, J. and Kraus, E. (1967). A one-dimensional model of the seasonal thermocline i. a laboratory experiment and its interpretation. *Tellus*, 19(1):88–97.

Ueda, H., Ohba, M., and Xie, S.-P. (2009). Important factors for the development of the asian–northwest pacific summer monsoon. *Journal of climate*, 22(3):649–669.

Ueda, H., Yasunari, T., and Kawamura, R. (1995). Abrupt seasonal change of large-scale convective activity over the western pacific in the northern summer. *Journal of the Meteorological Society of Japan. Ser. II*, 73(4):795–809.

Vincent, E. M., Emanuel, K. A., Lengaigne, M., Vialard, J., and Madec, G. (2014). Influence of upper ocean stratification interannual variability on tropical cyclones. *Journal of Advances in Modeling Earth Systems*, 6(3):680–699.

Vincent, E. M., Lengaigne, M., Madec, G., Vialard, J., Samson, G., Jourdain, N. C., Menkes, C. E., and Jullien, S. (2012a). Processes setting the characteristics of sea surface cooling induced by tropical cyclones. *Journal of Geophysical Research: Oceans*, 117(C2).

Vincent, E. M., Lengaigne, M., Vialard, J., Madec, G., Jourdain, N. C., and Masson, S. (2012b). Assessing the oceanic control on the amplitude of sea surface cooling induced by tropical cyclones. *Journal of Geophysical Research: Oceans*, 117(C5).

Wallcraft, A., Metzger, E., and Carroll, S. (2009). Software design description for the hybrid coordinate ocean model (HYCOM), Version 2.2. Technical report, Naval Research Lan Stennis Space Center MS Oceanography Div.

Walsh, K., Fiorino, M., Landsea, C., and McInnes, K. (2007). Objectively determined resolution-dependent threshold criteria for the detection of tropical cyclones in climate models and reanalyses. *Journal of climate*, 20(10):2307–2314.

Wamsley, L. (2018). Dozens more feared dead in the philippines after typhoon triggers mudslide. *National Public Radio*.

Wang, B., Ding, Q., Fu, X., Kang, I.-S., Jin, K., Shukla, J., and Doblas-Reyes, F. (2005). Fundamental challenge in simulation and prediction of summer monsoon rainfall. *Geophysical Research Letters*, 32(15).

Wang, S. (2020). Mixed layer velocity and surface wind stress from numerical simulation of Super Typhoon Mangkhut [Dataset]. *Zenodo*.

Warner, S. J., Becherer, J., Pujiana, K., Shroyer, E. L., Ravichandran, M., Thangaprakash, V., and Moum, J. N. (2016). Monsoon mixing cycles in the bay of bengal: A year-long subsurface mixing record. *Oceanography*, 29(2):158–169.

Warner, S. J. and Moum, J. N. (2019). Feedback of mixing to enso phase change. *Geophysical research letters*, 46(23):13920–13927.

Whitt, D. B. and Thomas, L. N. (2015). Resonant generation and energetics of wind-forced near-inertial motions in a geostrophic flow. *Journal of Physical Oceanography*, 45(1):181–208.

Wu, L., Wen, Z., and Wu, R. (2015). Influence of the monsoon trough on westward-propagating tropical waves over the western north pacific. part ii: Energetics and numerical experiments. *Journal of Climate*, 28(23):9332–9349.

Wunsch, C., Heimbach, P., Ponte, R. M., Fukumori, I., and MEMBERS, E.-G. C. (2009). The global general circulation of the ocean estimated by the ecco-consortium. *Oceanography*, 22(2):88–103.

Xie, S.-P., Chang, C.-H., Xie, Q., and Wang, D. (2007). Intraseasonal variability in the summer south china sea: Wind jet, cold filament, and recirculations. *Journal of Geophysical Research: Oceans*, 112(C10).

Xie, S.-P., Xie, Q., Wang, D., and Liu, W. T. (2003). Summer upwelling in the south china sea and its role in regional climate variations. *Journal of Geophysical Research: Oceans*, 108(C8).

Yablonsky, R. M. and Ginis, I. (2009). Limitation of one-dimensional ocean models for coupled hurricane–ocean model forecasts. *Monthly Weather Review*, 137(12):4410–4419.

Zebiak, S. E. (1989). Oceanic heat content variability and el niño cycles. *Journal of Physical Oceanography*, 19(4):475–486.

Zhang, H., Wu, R., Chen, D., Liu, X., He, H., Tang, Y., Ke, D., Shen, Z., Li, J., Xie, J., et al. (2018). Net modulation of upper ocean thermal structure by Typhoon Kalmaegi (2014). *Journal of Geophysical Research: Oceans*, 123(10):7154–7171.

Zhang, S., Xie, L., Hou, Y., Zhao, H., Qi, Y., and Yi, X. (2014). Tropical storm-induced turbulent mixing and chlorophyll-a enhancement in the continental shelf southeast of Hainan Island. *Journal of Marine Systems*, 129:405–414.

Zhang, S., Zhao, M., Lin, S.-J., Yang, X., Anderson, W., Zhang, W., Rosati, A., Underwood, S., and Zeng, F. (2015). Impact of having realistic tropical cyclone frequency on ocean heat content and transport forecasts in a high-resolution coupled model. *Geophysical research letters*, 42(14):5966–5973.

Zweers, N., Makin, V., De Vries, J., and Burgers, G. (2010). A sea drag relation for hurricane wind speeds. *Geophysical Research Letters*, 37(21).